

Dynamic Energy Planning for Autonomous Aerial Robots

University of Southern Denmark

Dynamic Energy Planning for Autonomous Aerial Robots

A Dissertation submitted in partial satisfaction of the
requirements for the degree of Doctor of Philosophy
in Robotics

by

Adam Seewald

Approved by:

Dr. Ulrik Pagh Schultz, Advisor
Unmanned Aerial Systems Center
University of Southern Denmark

Approved on:

<https://doi.org/10>.

The typesetting is done using L^AT_EX. Figures are generated with PGF/TikZ. Fonts are EB Garamond, Helvetica, and Iwona for body, headers, and equations respectively.

Copyright © 2021 by Adam Seewald. Some rights reserved.

This work is subject to CC BY-NC-SA license, which means that you can copy, redistribute, remix, transform, and build upon the content for any non commercial purpose, as long as you give appropriate credit, provide a link to the license, and indicate if changes were made. If you remix, transform, or build upon the material, you must distribute your contributions under the same license as the original. License details: <https://creativecommons.org/licenses/by-nc-sa/4.0/>



First edition, 2021

Published by University of Southern Denmark, in Odense, Denmark

To ...

Acknowledgements

Contents

1	<i>Introduction</i>	1
1.1	<i>From UAVs to Modern Aerial Robots</i>	3
1.2	<i>Common Classes of Aerial Robots</i>	5
1.3	<i>Motivation</i>	7
1.3.1	<i>Path planning and computations scheduling</i>	8
1.3.2	<i>Objective</i>	9
1.4	<i>Outline of the Approach</i>	10
1.5	<i>Applications</i>	11
1.6	<i>Contribution</i>	12
1.7	<i>Structure</i>	12
2	<i>Problem Formulation</i>	15
2.1	<i>Definitions of computations and motion</i>	16
2.2	<i>Definitions of path functions</i>	17
2.3	<i>Definitions of stages and triggering points</i>	18
2.4	<i>Definition of the plan</i>	20
2.5	<i>Planning problem</i>	22
2.6	<i>Precision agriculture example</i>	23
2.6.1	<i>paths sub-plan</i>	23
2.6.2	<i>Computations sub-plan</i>	28
2.6.3	<i>Planning problem with paths and computations sub-plans</i>	29
2.7	<i>Summary</i>	30
3	<i>State of the Art</i>	31
3.1	<i>Energy Modeling</i>	31
3.2	<i>Motion Planning</i>	33
3.3	<i>Planning with Dynamics</i>	34
3.4	<i>Planning for Autonomous Aerial Robots</i>	34

3.4.1	<i>Flight controllers</i>	34
3.4.2	<i>Energy models in aerial robotics</i>	34
3.4.3	<i>State estimation in aerial robotics</i>	34
3.4.4	<i>Optimal control in aerial robotics</i>	34
3.5	<i>Planning Computations with Motion</i>	34
3.6	<i>Summary</i>	34
4	<i>Energy Models</i>	35
4.1	<i>Energy Model of the Computations</i>	35
4.1.1	<i>Computational energy of the aerial robot</i>	36
4.1.2	<i>Energy modeling for heterogeneous hardware</i>	38
4.1.3	<i>Measurement layer</i>	39
4.1.4	<i>Application specification</i>	40
4.1.5	<i>Predictive layer</i>	40
4.1.6	<i>Hardware platforms and benchmarks</i>	42
4.1.7	<i>Power measurements</i>	44
4.1.8	<i>The powprofiler tool</i>	46
4.1.9	<i>Energy-aware design of algorithms</i>	47
4.1.10	<i>ROS integration</i>	47
4.1.11	<i>Experimental evaluation</i>	47
4.2	<i>Battery Model</i>	48
4.2.1	<i>Batteries for aerial robots</i>	48
4.2.2	<i>Derivation of differential battery model</i>	48
4.3	<i>Energy Model of the Motion</i>	49
4.3.1	<i>Mechanical energy of the aerial robot</i>	49
4.3.2	<i>Fourier series of empirical data</i>	51
4.4	<i>Periodic Energy Model</i>	52
4.4.1	<i>Derivation of the differential periodic model</i>	52
4.4.2	<i>Nominal control</i>	57
4.4.3	<i>Parameters scale transformation</i>	60
4.4.4	<i>Aperiodic energy evolution</i>	61
4.5	<i>Contribution</i>	61
4.6	<i>Results</i>	62
4.6.1	<i>Validation</i>	64
4.6.2	<i>Assessment</i>	65
4.7	<i>Summary</i>	65
5	<i>State Estimation</i>	67
5.1	<i>A Brief History of State Estimation</i>	67
5.2	<i>A Necessary Background on Probability Theory</i>	67

5.3	<i>The Curve Fitting Problem</i>	67
5.3.1	<i>Least square fitting</i>	67
5.3.2	<i>Levenberg-Marquardt algorithm</i>	67
5.4	<i>Periodic Model Estimation</i>	67
5.4.1	<i>Period estimation</i>	67
5.4.2	<i>Minimization of the estimate error</i>	67
5.4.3	<i>Period and horizon in continuous estimation</i>	67
5.5	<i>Filtering</i>	67
5.5.1	<i>Discrete time Kalman filter</i>	67
5.5.2	<i>Continuous time Kalman filter</i>	68
5.5.3	<i>Nonlinear filtering</i>	68
5.6	<i>Results</i>	68
5.7	<i>Summary</i>	69
6	<i>Guidance</i>	71
6.1	<i>Vector Fields for Guidance</i>	71
6.2	<i>Derivation of the Guidance Action</i>	72
6.2.1	<i>Motion simulations</i>	72
6.2.2	<i>Energy simulations</i>	72
6.3	<i>Alteration of the Path</i>	72
6.4	<i>Results</i>	73
6.5	<i>Summary</i>	73
7	<i>Optimal Control Generation</i>	75
7.1	<i>A Brief History of Optimal Control</i>	76
7.2	<i>Optimization Problems with Dynamics</i>	78
7.2.1	<i>Continuous systems: unconstrained case</i>	78
7.2.2	<i>Continuous systems: constrained case</i>	79
7.2.3	<i>Perturbed systems</i>	79
7.2.4	<i>Multistage systems</i>	79
7.3	<i>Numerical Simulation and Differentiation</i>	79
7.3.1	<i>Euler method</i>	79
7.3.2	<i>Runge-Kutta methods</i>	79
7.3.3	<i>Algorithmic differentiation</i>	79
7.4	<i>Direct Optimal Control Methods</i>	79
7.4.1	<i>Direct single shooting</i>	79
7.4.2	<i>Direct multiple shooting</i>	79
7.4.3	<i>Direct collocation</i>	80
7.5	<i>Numerical Optimization</i>	80
7.5.1	<i>Convexity</i>	80

7.5.2	<i>Optimality conditions</i>	80
7.5.3	<i>First order optimality conditions</i>	80
7.5.4	<i>Second order optimality conditions</i>	80
7.5.5	<i>Sequential quadratic programming</i>	80
7.5.6	<i>Nonlinear interior point methods</i>	80
7.6	<i>Model Predictive Control</i>	80
7.6.1	<i>Output model predictive control</i>	80
7.6.2	<i>Optimal control generation with model predictive control</i>	82
7.6.3	<i>Dynamic planning algorithm</i>	84
7.7	<i>Results</i>	84
7.8	<i>Summary</i>	84
8	<i>Summary and Future Directions</i>	85
8.1	<i>Summary</i>	85
8.2	<i>Contribution</i>	85
8.3	<i>Future Directions</i>	85
8.4	<i>Conclusion</i>	85
<i>Appendices</i>		87
A	<i>Implementation</i>	87
A.1	<i>Energy Models</i>	87
A.2	<i>State Estimation</i>	91
A.2.1	<i>Estimation of the period</i>	91
A.2.2	<i>Estimation of the state</i>	92
A.3	<i>Guidance</i>	92
A.4	<i>Optimal Control Generation</i>	93
<i>References</i>		97
<i>Index</i>		105

Figures

<i>Opterra fixed-wing aerial robot</i>	2
<i>Hewitt-Sperry Automatic Airplane, first unmanned flying machine</i>	4
<i>NASA's Ingenuity Mars Helicopter</i>	5
<i>Skye, an omnidirectional spherical blimp</i>	6
<i>Different aerial robots in relation to the M&CE and flight time</i>	8
<i>The covering problem in a precision agriculture scenario</i>	9
<i>Diagram of the structure</i>	12
<i>Concept of the path and generic point in space</i>	18
<i>Definition of a plan</i>	21
<i>Detail of a stage in the FSM</i>	21
<i>Definition of a plan with a loop</i>	22
<i>Intuitive plan to cover a regular polygon with four sides</i>	24
<i>Fixed-wing aerial robot's plan to cover a regular polygon with four sides</i>	25
<i>Alteration of a path parameter of the fixed-wing aerial robot's plan</i>	27
<i>Overview of energy modeling for heterogeneous hardware</i>	39
<i>Average power</i>	41
<i>Overall energy</i>	41
<i>Remaining battery capacity</i>	42
<i>Average power</i>	42
<i>Overall energy</i>	43
<i>Remaining battery capacity</i>	43
<i>ODROID XU3</i>	44
<i>NVIDIA Jetson TK1</i>	44
<i>NVIDIA Jetson TX2</i>	45
<i>NVIDIA Jetson Nano</i>	45
<i>Energy data of a fixed-wing aerial robot</i>	52

<i>Trajectory of the aerial robot flying the highest path configuration</i>	59
<i>Trajectory of the aerial robot flying the lowest path configuration</i>	59
<i>Concept of a path and computation parameter scale transformation</i>	61
<i>Layer 2 model of darknet-gpu component</i>	63
<i>Path parameter in the flight of an aerial robot</i>	71
<i>External interference on the path</i>	72
<i>Summary of the optimal control approach</i>	76
· · · · ·	83

Notation

\exists	there exists
\in	is an element of the set
$:=$	is defined
$f(\cdot)$	is function f
$f : \mathbb{C} \rightarrow \mathbb{D}$	f maps set \mathbb{C} to set \mathbb{D}
\mathbb{Z}	set of integers
$\mathbb{Z}_{\geq 0}$	set of positive integers
$\mathbb{Z}_{> 0}$	set of strictly positive integers
\mathbb{R}	set of reals
$\mathbb{R}_{\geq 0}$	set of positive reals
$[x]$	set of positive integers up to a : $\{0, 1, \dots, a\}$, with $a \in \mathbb{Z}_{\geq 0}$
$[x]_{> 0}$	set of strictly positive integers up to a : $\{1, 2, \dots, x\}$, with $x \in \mathbb{Z}_{> 0}$
\mathbf{x}	vector
X	matrix
\mathbf{x}', X'	transpose of a vector \mathbf{x} or of a matrix X
\mathbf{x}^{-1}, X^{-1}	inverse of a vector \mathbf{x} or of a matrix X
x_i	i th set of parameters
$x_{i,j}$	j th parameter of the i th set of parameters
$\underline{x}_{i,j}$	lower bound of the parameter $x_{i,j}$
$\overline{x}_{i,j}$	upper bound of the parameter $x_{i,j}$
x^*	optimal with respect to a given cost

Abbreviations

LP	linear program
QP	quadratic program
MPC	model predictive control
NLP	non linear program
UAV	unmanned aerial vehicle
UAS	unmanned aerial system
OCP	optimal control problem
BVP	boundary-value problem
RSTA	reconnaissance, surveillance, and target acquisition
GNSS	global navigation satellite system
IMU	inertial measurement unit
RPV	remotely piloted vehicle
GPS	global positioning system
SoC	state of charge
M&CE	difference of motion and computations energy
CNN	convolutional neural network
FPS	frames per second
FSM	finite state machine

Chapter 1

Introduction

MOBILE ROBOTS are a class of robots with the ability to move through the environment (Corke, 2017). Most of these robots are power-demanding devices constrained by battery limitations. Although such limitations are a common challenge in many areas, they are critical in mobile robots' design and development. They influence the level of autonomy (Seewald, Garcia de Marina, et al., 2020), which in turn is expected to increase in the foreseeable future (Fisher et al., 2013).

To move, mobile robots combine different components which sense and interact with the surrounding environment (Mei et al., 2006). The analysis and interpretation of the data originating from these components often rely on high-level decisions. These are usually implemented on energy-demanding heterogeneous computing hardware. Planning an energy-aware path with a power-saving scheduling policy on such hardware is an underrepresented topic in the literature. Many past approaches focus almost exclusively on one of these topics. Some generate an energy-optimized path, despite the computations energy almost equaling the motion energy of some instances of low-energy mobile robots (Sudhakar et al., 2020). Moreover, due to the recent advancements in the computational capabilities of heterogeneous computing hardware, such as the introduction of powerful portable GPUs (Rizvi et al., 2017), the use of computations is on the rise (Abramov et al., 2012; Jaramillo-Avila et al., 2019; Satria et al., 2016). Others provide a power-saving scheduling policy. Yet, moving a mobile robot requires considerable energy expenditure over mere computations (Mei et al., 2004, 2005).

In this work, we focus on dynamic energy planning. We generate both an energy-aware plan of the path and a power-saving schedule of the computations. We plan these two aspects simultaneously, exploring their tradeoffs. We demonstrate the approach both in simulation and empirically, and we focus on aerial mobile robots. Al-



Fig. 1.1. Opterra fixed-wing aerial robot employed for precision agriculture (photo credit: Amit Ferencz Appel).

though these systems share with the broader class of mobile robots stringent battery limitations, handling the battery in flight introduces additional complications. It is generally required landing to replace or recharge the battery (Zamanakos et al., 2020). Aerial robots are thus an ideal instance of energy-constrained systems that would benefit from a dynamic energy planning technique. In the remainder of this work, we thus focus our analysis on aerial robots.

There are many autonomous use cases involving aerial robots, such as precision agriculture, search and rescue, payload delivery, transportation, and many others. To formulate a mobile robot planning problem later in [Chapter 2](#), we focus on precision agriculture and progressively build dynamic planning of a fixed-wing aerial robot flying over an agricultural field with little human input.

We investigate different physical aerial robotics platforms in this work but we focus most on the Opterra fixed-wing aerial robot ([Hobby, 2020](#)) adapted for precision agriculture. Precision agriculture is often put into practice ([Hajjaj and Sahari, 2014](#)) with ground mobile robots used for harvesting ([Aljanobi et al., 2010; De-An et al., 2011; F. Dong et al., 2011; Edan et al., 2000; Z. Li et al., 2008; Qingchun et al., 2012](#)), and unmanned aerial vehicles (UAVs) for preventing damage and ensuring better crop quality ([Daponte et al., 2019; Puri et al., 2017](#)). The aerial robot is shown in [Figure 1.1](#).

In the remainder of the chapter and before we introduce the problem in [Chapter 2](#), we briefly investigate the evolution of the field of aerial robotics in the next section. We then analyze the main aerial robots available today, and how they apply to dynamic energy planning in [Section 1.2](#). We then provide some further motivation for our planning in [Section 1.3](#) and the outline of the approach in [Section 1.4](#). Finally, we provide the structure of the remaining chapters in [Section 1.7](#).

This chapter connects to the remainder of this work as follows. Here we introduce and motivate the dynamic energy planning for autonomous aerial robots. We formalize the planning problem in [Chapter 2](#). We describe the derivation of a proper energy model to predict the future energy consumption of the planning problem in [Chapter 4](#). We estimate some coefficients of the model using robust estimation techniques in [Chapter 5](#). We implement an optimal configuration of the path and computations using data-driven control and other modern optimal control techniques in [Chapter 7](#). We use such configuration for guidance and scheduling of the aerial robot in [Chapter 6](#). The guidance moves physically the robot; the scheduling defines the granularity of the tasks being executed in flight. Moreover, we discuss previous approaches to solve the dynamic planning problem in [Chapter 3](#).

1.1 From UAVs to Modern Aerial Robots

Modern aerial robots are a valuable tool in robotic research and aerospace. They are found with different names in the literature. These include unmanned aerial vehicles (UAVs)¹, unmanned aerial systems (UASs), flying robots, or drones. Usually, we refer to drones, UAVs, and UASs when these systems are semi-autonomous, operated from the ground. UAS often denotes the entire infrastructure of unmanned flight in the aerospace jargon. Aerial or flying robots, on the other hand, have advanced levels of autonomy ([Siciliano and Khatib, 2016](#)). Nevertheless, all these systems have basic autonomous features such as position and altitude holding and leveling. The position holding is usually implemented using global navigation satellite system (GNSS), altitude holding using a barometer, and leveling using inertial measurement unit (IMU).

The origin of the field of aerial robotics, which deals with the design and development of aerial robots, dates back to the first guided missiles: unmanned (or uninhabited) flight has more than a century of developments ([Siciliano and Khatib, 2016](#)). Hewitt-Sperry Automatic Airplane, also denominated “flying bomb”, developed in 1917 during World War I (WWI) ([Keane and Carr, 2013](#); [Valavanis and Vachtsevanos, 2015](#)) is often referred to as the first unmanned flying machine. It is shown in [Figure 1.2](#). It has been developed 14 years after the first heavier-than-air flight in history, demonstrated on December 17, 1903, with the Wright Flyer I by Wilbur and Orville Wright (or the Wright brothers). The Hewitt-Sperry Automatic Airplane used a gyroscope similarly to modern aerial robots. The device, invented by Elmer Sperry ([Keane and Carr, 2013](#)), was mechanically connected to the control surfaces and successfully implemented a control feedback loop ([Siciliano and Khatib, 2016](#)).

In the early days, the first flying machines were referred to as remotely piloted vehicles (RPVs) ([Anderson, 2005](#)). Many instances from WWI on of these vehicles were designed for military purposes. In the 1950s, United States used a remotely controlled

¹The term unmanned is sometimes replaced by uninhabited



Fig. 1.2. The Hewitt-Sperry Automatic Airplane, also denominated “flying bomb”, was developed in WWI and represents the first instance of a UAV (photo credit: United States Naval Institute).

vehicle, the Ryan Firebee, for reconnaissance in Vietnam, and Israel was the first to use a RPV in a combat situation ([Anderson, 2005](#)). Other instances of these vehicles include the V-1 flying bomb from 1944 (deployed by the unified armed forces of nazi Germany) and the Lockheed D-21 from 1962 (deployed by the United States Air Force). Global positioning system (GPS) at the end of 1970 allowed some more recent remotely piloted vehicles to be used in surveillance. These systems were later integrated with cameras and other sensors ([Siciliano and Khatib, 2016](#)), in what are the modern aerial robots.

In recent years, the unmanned flight has been applied in many civilian applications ([González-Jorge et al., 2017](#)). Modern aerial robots are increasingly used in remote sensing ([Milas et al., 2018; Noor et al., 2018; Tang and Shao, 2015](#)), surveillance ([Bürkle, 2009; Paucar et al., 2018](#)), meteorology ([Schuyler et al., 2019](#)), search and rescue ([Cui et al., 2015; Karaca et al., 2018; Pensieri et al., 2020; Seguin et al., 2018](#)), precision agriculture ([Daponte et al., 2019; Puri et al., 2017](#)), transportation, and payload delivery ([Kellermann et al., 2020](#)). The former four categories fall into the area of reconnaissance, surveillance, and target acquisition (RSTA) and do not require advanced autonomy. Precision agriculture, transportation, and payload delivery are often realized using to a greater or lesser extent some advanced levels of computational intelligence ([Siciliano and Khatib, 2016](#)). Modern aerial robots are designed to handle unexplored terrain with little interaction as opposed to the past UAVs operated mainly by a human operator ([Siciliano and Khatib, 2016](#)). Instances of modern aerial robots are expected to autonomously adapt and possibly interact in a broad variety of environmental conditions.



Fig. 1.3. NASA’s Ingenuity Mars Helicopter. A rotary-wing coax aerial robot that achieved the first powered, controlled flight on another planet on April 19, 2021. The project is solely a demonstration of technology (photo credit: NASA Jet Propulsion Laboratory).

In summary, aerial robots have a relatively recent past. Some initial experiments of unmanned flights were performed shortly after the first heavier-than-air manned, powered flight. These initial experiments were mostly developed for military purposes, whereas modern aerial robots are used in a broad range of civil applications. Aerial robots are expected to grow significantly in numerous areas of robotics research ranging from agriculture to planetary exploration. For the latter, Figure 1.3 shows NASA’s Ingenuity Mars Helicopter. A small coaxial aerial robot that performed the first powered, controlled flight on another planet on April 19, 2021. Aerial robots for planetary exploration are to be further deployed in future explorations endeavors, for instance, to study Saturn’s moon Titan (Voosen, 2019).

Finally, we conclude this section with a quote from (Anderson, 2005): “the Wright brothers worked so hard to put humans in the air in flying machines, a hundred years later some [...] are working hard to take them out of flying machines”.

1.2 Common Classes of Aerial Robots

Numerous different types of aerial robots have emerged ever since their first introduction. We briefly investigate the most studied classes in the robotics literature and relate them to the dynamic energy planning that we focus on in this work. The two most generic classes are heavier-than-air and lighter-than-air aerial robots. Heavier-than-air aerial robots are divided into fixed- and rotary-wings (Siciliano and Khatib, 2016), and some recent developments in bio-inspired robotics study flapping-wings (Floreano and Wood, 2015).



Fig. 1.4. Skye, an omnidirectional spherical blimp developed by ETH Zürich for entertainment purposes. It has a camera system and combines the energy-efficient flight of a blimp with the characteristics of a quadrotor (photo credit: ETH Zürich).

Rotary-wing aerial robots are highly maneuverable and can perform stationary vertical flight (commonly referred to as hovering) (Siciliano and Khatib, 2016). These systems can be classified into further categories, which include multirotors (such as quadrotors or quadcopters, hexacopters, and octocopters), conventional helicopters (these have one main and one tail rotor), and a coax (these have counter-rotating coaxial rotors) (Corke, 2017). Some examples of quadrotors are DJI Mavic Mini in (h), and DJI Phantom 4 in (j) in Figure 1.5. In the same figure, DJI Agras T16 in (g), and DJI Matrice 600 in (f) are hexacopters.

Fixed-wing aerial robots have wings to provide the lift, some control surfaces for maneuvering, and a propeller for forward thrust; a shared principle with a common passenger aircraft (Corke, 2017). An example constitutes the Opterra adapted for precision agriculture in Figure 1.1, Cumulus in (b), Ebee in (d), and Penguin BE in (c) (Haugen and Imsland, 2016) in Figure 1.5. Examples of flapping-wings are Delfly II in (k) (Percin et al., 2012), and Nano-Hummingbird in (l) in Figure 1.5. We discuss in detail heavier-than-air aerial robots in this work, as they are a common platform for robotics research. We focus on the dynamic forces which govern the flight of rotary- and fixed-wings aerial robots in Chapter 6.

Common instances of lighter-than-air aerial robots are blimps (or non-rigid airships). They usually rely on a gas—such as helium enclosed in a protected envelope (Burri et al., 2013)—to generate the lifting force (Fui Liew et al., 2017). An omnidirectional spherical blimp is shown in Figure 1.4. Blimps are similar to balloons but provide basic maneuverability, whereas, in a balloon, only the altitude can be controlled (Colombatti et al., 2011).

Some other classifications found in aerial robotics literature trade size and maneuverability and include classes as micro aerial vehicles (MAVs) or vertical take-off and landing (VTOLs) aerial robots. The former are aerial robots with all dimensions lower than 15 cm. The latter are aerial robots flying in a fixed-wing configuration except if taking-off and landing where they use thrust from rotors rather than lift from wings.

Among the classes in this section, rotary-wings are the most maneuverable and lighter-than-air aerial robots are the least. These, however, have the highest flight time followed by fixed-wing aerial robots. Mixed configurations, such as VTOLs, fall into the intersection of rotary and fixed-wings for what concerns maneuverability and flight time ([Siciliano and Khatib, 2016](#)). The energy requirements are critical for all aerial robots, but the difference of motion and computations energy (M&CE) varies greatly. The energy—*inversely proportional to flight time*—is highest in rotary-wings and lowest in lighter-than-air aerial robots as shown later in [Figure 1.5](#). The dynamic energy planning approach thus relies on both power-saving task scheduling and energy-efficient path planning for the fixed-wings robots while relying almost exclusively on energy-efficient path planning for rotary-wing aerial robots. In the former M&CE is close to zero, in the latter is usually high except in energy optimized designs such as some rotary-wing MAVs. Hypothetically, in lighter-than-air aerial robots, M&CE might be negative; the energy planning approach would rely heavily on power-saving task scheduling.

1.3 Motivation

In this section, we provide a brief motivation for dynamic energy planning of these systems. Many applications that involve aerial robots have strict battery constraints. Although this is a common problem to most mobile robots, aerial robots are of particular concern. The autonomy of these systems is affected by the availability of the power source. A typical example of an aerial robotics scenario is a robot following a path and performing some onboard computations. For instance, the robot might detect ground patterns and notify other ground-based actors with little human interaction in precision agriculture or another application. Aerial robots in this situation often carry some heterogeneous computing hardware and a microcontroller. Energy requirements of such computing hardware are a further complication. Computing hardware is involved in autonomous capabilities and planning itself—both often require computer vision or other complex algorithms—whereas microcontroller runs motion primitives by directly interfacing actuators (such as servos for the control surfaces) and motors. Energy-wise, it is advantageous to schedule the computations on the computing hardware and simultaneously to plan the path.

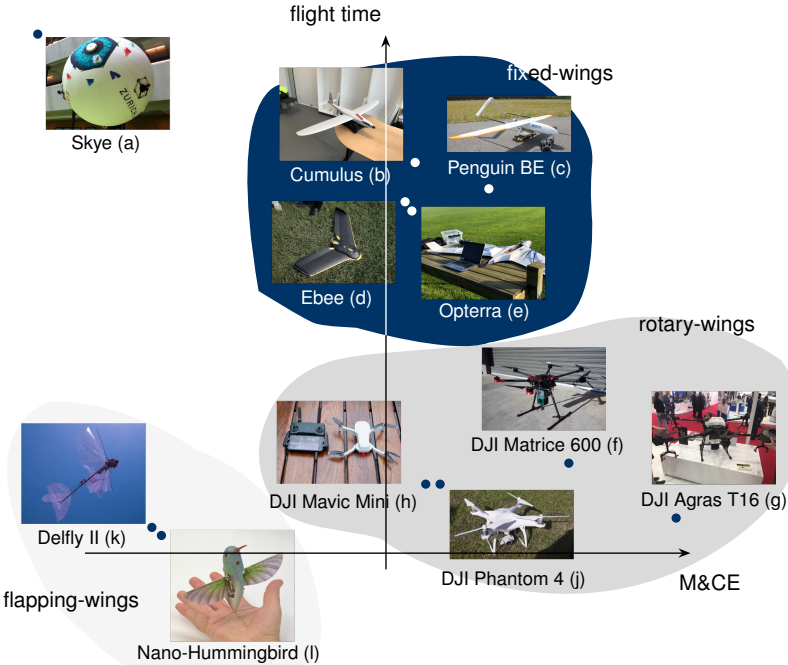


Fig. 1.5. Different aerial robots in relation to the M&CE and flight time, with a hypothetical fixed costs for computations energy. Heavier-than-air aerial robots (b)–(l) include flapping-wings (k), (l) and have a negative M&CE (computations scheduling is to be accounted for most in planning), whereas rotary-wings have a positive M&CE (f), (g) (path planning is to be accounted for most in dynamic planning). Some smaller rotary-wings have a M&CE closer to zero (h), (j). In general, rotary-wings have a short flight time. Fixed-wings (b)–(e) have a considerably longer flight time and M&CE close to zero (computations scheduling and path planning have both to be accounted for in dynamic planning). Lighter-than-air aerial robots (a) have hypothetically a relatively long flight time and lower than zero M&CE (photos credit: (b) to Sky-Watch, (f) to Rise Above, (g) to Aeromotus, (h) to Digital Photography Review, (j) to ePHOTOZine, and (l) to DARPA).

1.3.1 Path planning and computations scheduling

It is uncommon to find a ready-to-use solution for both planning the path and scheduling the computations of these systems in an energy-aware fashion (we discuss in detail the state-of-the-art in this regard in Chapter 3). Planning the two aspects simultaneously would pose an advantage in terms of autonomy by, e.g., optimizing the path and computations in the function of the battery state of charge (SoC).

For certain classes of aerial robots with M&CE close or lower than zero, the autonomy can directly influence the battery state. For these classes, it is desirable to reschedule the computations energy-wise in-flight during a motion energy-demanding phase.



Fig. 1.6. The covering problem in a precision agriculture scenario. The aerial robot has to cover an agricultural field that forms a polygon (blue/transparent area in the frame) and run some autonomous tasks (photo credit: Amit Ferencz Appel).

For instance, a fixed-wing aerial robot might be flying headwinds (with the wind vector parallel and opposite to the direction of motion) and utilizing more energy than planned. It would be of advantage to reschedule the tasks accordingly to save energy needed for motion. During the same flight, the wind direction might suddenly change. The fixed-wing craft, now flying tailwinds, requires less motion energy. It could then potentially increase the level of computations by rescheduling the tasks. Later in the flight, the battery might be subject to sudden drops (due to e.g., temperature changes) requiring replanning again by, e.g., shortening the path. It is clear that planning the path and scheduling the computations simultaneously in all these cases is the most desirable course of action.

In Figure 1.5 we show the M&CE against the flight time of different aerial robots. We observe that fixed-wings are the aerial robots that would advantage most from simultaneous path planning and computations scheduling. They have a M&CE close to zero and a relatively long flight time. Although some rotary-wings have M&CE also close to zero, their flight time is generally relatively short. Flapping-wing and lighter-than-air aerial robots require considerably less energy for the motion, and have a negative M&CE.

1.3.2 Objective

In the remainder of this work, we refer to computational tasks that can be scheduled in an energy-aware fashion as computations, opposed to the other tasks with no significant effect on energy consumption. We assume the aerial robot runs the computations

on the heterogeneous computing hardware. As an example, we refer to an aerial robot in a precision agriculture scenario in [Figure 1.1](#), which covers an agricultural field. In abstract terms, the field is represented by a polygon in [Figure 1.6](#) and the aerial robot detects some patterns on such polygon using a convolutional neural network (CNN). The aerial robot further communicates the position of a detected pattern to other, ground-based actors. Detecting the patterns usually involves heterogeneous computing elements (GPU and/or multiple CPU cores) and consumes a significant amount of energy as opposed to communication. Detection is a computation, while communication is an (energy-inexpensive) task.

We are interested in the energy optimization of the path and computations under uncertainty (atmospheric interferences) in-flight and refer to it as dynamic energy planning. Unlike most of the past mobile robotics planning literature, the approach that we propose plans these two aspects simultaneously. Such planning would find optimal tradeoffs between the path, computations, and energy requirements. Current generic planning solutions for aerial robots do not plan the path and computations dynamically, nor are they energy-aware. They are often semi-autonomous: the path and computations are static and usually defined using planning software ([Daponte et al., 2019](#)). Instances of the planning software include famous flight controllers ([Parrotarazzi, 2016](#); [PX4, 2016](#)). Such a state of practice has prompted us to investigate the topics presented in this work. We will gradually propose a dynamic energy planning approach for aerial robots. It plans both the path and computations while the aerial robot is flying and its batteries draining.

We formally define the robot planning problem after outlining the approach in the next section.

1.4 Outline of the Approach

In this work, we address the increasing demands for autonomy of modern aerial robots with a dynamic planning approach. The approach provides a simultaneous energy-aware plan of the path and a power-saving schedule of the computations. To this end, we first need a user-defined initial plan that is then replanned energy-wise using an energy model for future prediction. Later, an algorithm inputs the initial plan, estimates the state of the energy model, evaluates future energy consumption and re-plans parameters relative to the path and computations. The plan consists of different stages. At each stage, the aerial robot flies a path and executes some computations. Furthermore, it contains some additional parameters to alter the path and computations along with an energy budget. The alterations are bounded. There are path constraint sets that bound the path alterations and computations constraint sets, one per each computation, that bound computations alterations.

We use the concept of different stages to model complex paths. For instance, the path might contain multiple circles and lines. We will see such plan later in [Section 2.6](#). The approach guides the aerial robot on different paths (the plan is composed of) using vector field ([De Marina et al., 2017](#)). The robot switches between the paths as soon as it reaches specific triggering points.

The approach further relies on `powprofiler`, a profiling and modeling tool that we introduce in [Section 4.1](#). The tool models the energy consumption of the computations and is later employed to estimate the future energy of the aerial robot in flight. To this end, we empirically derive and formally prove a periodic energy model that accounts for the uncertainty. We use Fourier analysis to derive the model and state estimation to address the uncertainty. Periodicity is often present due to repetitive patterns in the plan ([Seewald, Garcia de Marina, et al., 2020](#)). Indeed, mobile robots often iterate over a set of tasks and paths ([seewald2021energy](#)). Given that the plan is periodic, we expect the energy consumption to evolve (approximately) periodically. We describe in detail such model in [Section 4.4](#).

The replanning of the path and computations is achieved with modern optimal control techniques, such as optimal state estimation in [Chapter 5](#), and model predictive control (MPC) ([Rawlings et al., 2017](#)) in [Chapter 7](#). The control is data-driven. Energy sensor data estimates some coefficients of the model used to predict the future energy consumption with uncertainty. The replanning is done under an energy budget—the battery capacity and other battery parameters. Our goal is to complete the plan with the highest possible parameters configuration.

1.5 Applications

The dynamic energy planning in this work applies to modern aerial robots with a certain degree of autonomy. By the latter, we mean that the robot performs at least a predefined set of tasks over a given space. Although most of the guidance in [Chapter 6](#) is designed for aerial robots specifically, the approach can be easily adapted to other mobile robots with energy constraints. We discuss applications out of aerial robotics domain further in [Chapter 8](#). For instance, we have applied the approach to the space robotics context ([Seewald, 2020](#)).

In the remainder of this work, we focus on the precision agriculture scenario in [Figure 1.6](#). In summary, the aerial robot covers a given agricultural field (a polygon) and searches for ground hazards. With the scenario, we validated the work experimentally. Path-wise, the aerial robot flies in circles and lines covering the polygon. Computation-wise, it detects hazards using the CNN and notifies grounded mobile robots employed for, e.g., harvesting. The approach alters the plan; it controls the processing rate and the radius of the circles affecting the distance between the lines. We

will see this concrete scenario described formally in [Section 2.6](#) and solved progressively in the remaining chapters.

1.6 Contribution

1.7 Structure

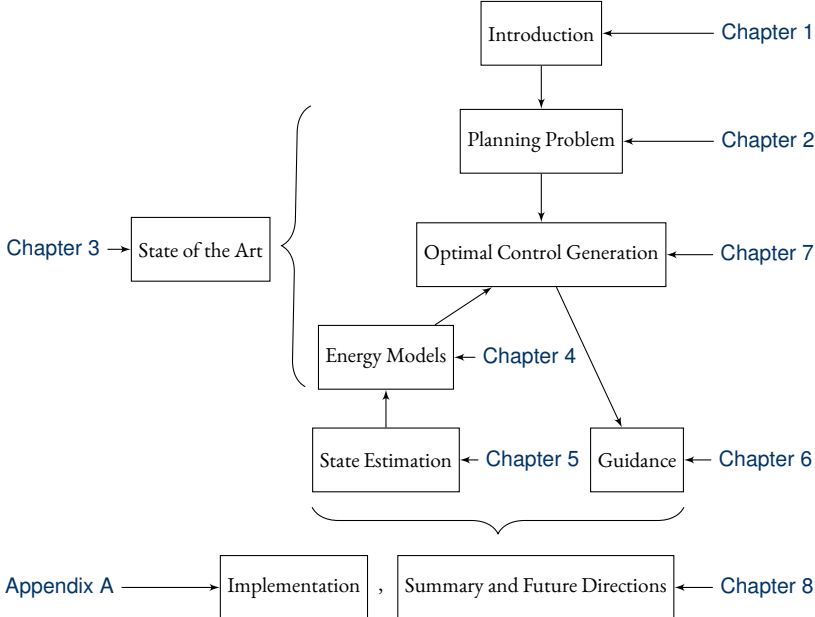


Fig. 1.7. Diagram of the structure of this work. Chapter 1 serves as an introduction while Chapter 3 presents the state of the art. Chapter 2 presents the planning problem, which is solved in Chapter 7 using notions from Chapters 4–5. Chapter 5 presents the guidance action to move over a replanned path and Appendix A the implementation. Chapter 8 concludes the work and proposes future directions.

The remainder of this work is illustrated in [Figure 1.7](#) structured as follows. In this chapter, we introduced the dynamic energy planning for aerial robots. We define the planning problem in [Chapter 2](#), and propose the solution to the problem in [Chapter 7](#), which builds upon the topics presented in the remaining chapters. In particular, in [Chapter 3](#) we present the state-of-the-art in energy modeling and planning for mobile robots. We include some energy models for heterogeneous computing hardware.

Dynamic planning requires accurate future energy predictions. We present the derivation of some energy models to address future energy predictions in [Chapter 4](#). Specifically, we propose energy models for computations, motion, and the battery. We

derive and formally prove a periodic energy model that we use in the remainder of this work to predict future energy consumption. The periodic energy model's accuracy depends on the availability of measurements of energy data. We detail the process in [Chapter 5](#). We describe how to estimate the coefficients of the periodic energy model and refine the future predictions with the available data.

Flying on a dynamic plan requires the derivation of a guidance action to guide the aerial robot in space. This process is elaborated in [Chapter 6](#). We discuss an approach to guide the aerial robot in space on the planned path.

An optimal solution for the dynamic mobile robot planning problem relies on optimal control techniques. We describe such techniques in [Chapter 7](#). Specifically, after summarizing some of these techniques, we propose an optimization algorithm to select the optimal parameters configuration for the path and computations simultaneously. Finally, we conclude our work in [Chapter 8](#) along some recommendations for future research direction.

We then present some additional information in appendices. In [Appendix A](#) we propose the implementation in MATLAB(R) of the planning problem, the model, the estimation technique, the guidance action, and the derivation of the optimal control.

Chapter 2

Problem Formulation

IN THIS CHAPTER, we discuss the planning problem that we are interested in solving. Such planning problem relies on the initial user-defined plan that we formally define later in [Section 2.4](#). We have briefly discussed the plan in [Section 1.4](#). It is replanned energy-wise in the eventuality of energy constraints dissatisfaction, and whenever the uncertainty affects the flight unexpectedly. The initial user-defined plan includes both the computations and motion. Hence, we define both these constructs. In particular, we provide formal definitions of some basic concepts in [Sections 2.1–2.3](#). These include the computations, motion, their energy, difference between computation and motion energy (M&CE) that we encountered in [Section 1.2](#), path, and some other plan-specific constructs. We then use all these to formulate the planning problem in [Section 2.5](#). We illustrate the problem on an example of the precision agriculture scenario in [Section 2.6](#).

The algorithm that we present in [Section 7.6.3](#) inputs the user-defined plan from this chapter for future energy modeling, estimation of the energy model, and guidance. It optimizes the plan with some parameters (which we also briefly outlined in [Section 1.4](#)) to plan the best configuration of computations and paths. The replanned plan is optimal energy-wise: the algorithm investigates the tradeoffs between paths and computations with varying battery and atmospheric conditions.

The chapter connects to the remainder of this work as follows. Here we formalize the plan, the planning problem, and some other basic constructs. We use the characteristics of the plan to derive an energy model in [Chapter 4](#), which we estimate from measured data in [Chapter 5](#). We solve the planning problem using modern optimal control techniques in [Chapter 7](#). With the solution, we refine the original problem in terms of both the path and computations. We guide the aerial robot using a vector field that we describe in [Chapter 6](#), where we utilize the plan's building blocks for

paths from this chapter. We discuss past approaches to solve the planning problem in [Chapter 3](#), and the concrete implementation in [Appendix A](#).

2.1 Definitions of computations and motion

Firstly, we define computations, motion, their energy, and M&CE. These are some basic concepts that our dynamic planning relies upon.

Definition 2.1.1: Computations/motion

Computations are energy-demanding computational tasks. The aerial robot runs the computations on heterogeneous computing hardware. The computing hardware interface microcontrollers.

Motion is the act of the aerial robot moving in the surrounding environment. The aerial robot runs some primitives on microcontrollers for this purpose. The microcontrollers interface actuators, motors, and other components.

Autonomous capabilities are often achieved by interconnecting heterogeneous computing hardware and microcontrollers. We assume that for the computations, the heterogeneous computing hardware runs a schedule. The schedule is then characterized by some parameters. For instance, for the CNN detection from the precision agriculture scenario in [Section 1.3.2](#), a parameter is the frames per second (FPS) rate. Alike for the computations, we assume that for the motion, the robot travels some paths characterized by some other parameters. For instance, for the covering problem, a parameter changes the distance between the survey lines.

Definition 2.1.2: Computations/motion and overall energy

Given a path characterized by ρ parameters $c_i^\rho := \{c_{i,1}, c_{i,2}, \dots, c_{i,\rho}\}$, the *motion energy* is the energy spent by the aerial robot while moving on the path.

Given a schedule characterized by parameters $c_i^\sigma := \{c_{i,\rho+1}, \dots, c_{i,\rho+\sigma}\}$, the *computations energy* is the energy spent by heterogeneous computing hardware executing the schedule.

The *overall energy* is the sum of motion energy and computations energy.

Physically, motion energy is the energy spent by all the systems powering the aerial robot, excluding the heterogeneous computing hardware. Computations, motion, and overall energies are measured in watts for instantaneous or average measures. They are measured in joules for measures over a given time interval. We show in [Section 2.3](#) what we mean by characterization of path and computations with some parameters and illustrate the concept on the agricultural scenario example in [Section 2.6](#).

M&CE that we introduced in [Section 1.2](#) is the difference of average motion and computations energy. It is measured in watts, and it gives a measure of which of the

two energy components is predominant. For M&CE greater than zero, the motion energy dominates over the computations. The dynamic planning approach plans first an energy-efficient path. If we return briefly to [Figure 1.5](#), it is the case for rotary-wing aerial robots (f), and (g) in [Figure 1.5](#). On the contrary, for M&CE lower than zero, the computations energy dominates. The dynamic planning approach plans first a power-saving schedule. In the figure, it is the case for lighter-than-air aerial robot (a) in [Figure 1.5](#). For M&CE close to zero, both energy components are important energy-wise. The dynamic planning approach plans both an energy-efficient path and power-saving schedule to a similar extent. This M&CE is characteristic for fixed-wing aerial robots, such as (b)–(e) in [Figure 1.5](#).

2.2 Definitions of path functions

To model the path, we use multiple mathematical functions $\varphi_1, \varphi_2, \dots$ that we call path functions. These functions express the path in 2D space at an altitude $h \in \mathbb{R}$ with respect to an inertial navigation frame \mathcal{O}_W . We discuss a generalization of the path functions in 3D space and how it affects the guidance in [Chapter 8](#).

Definition 2.2.1: Path functions

$\varphi_i : \mathbb{R}^2 \rightarrow \mathbb{R}, \forall i \in \{1, 2, \dots\}$ are *path functions* used to model the path. They quantify the distance of a generic time-dependent point $\mathbf{p}(t) := (x_{\mathbf{p}(t)}, y_{\mathbf{p}(t)})$ of the aerial robot flying in the 2D space on the z-axis from $\varphi_i = 0$ and are continuous and twice differentiable.

We use this notion to guide the aerial robot using vector field in [Chapter 6](#). For instance, one can define a line as a path function with

$$\varphi(x, y) := ax + by + c, \quad (2.1)$$

where $a, b, c \in \mathbb{R}$ are given constants. The generic point $\mathbf{p}(t)$ intersects $\varphi(x, y)$ on a specific value of the z-axis. The concept is illustrated in [Figure 2.1](#) for c zero and a, b minus one and two respectively. The point intersects the plane formed by the path function

$$\varphi(x, y) := 2y - x, \quad (2.2)$$

at $z = \varphi(\mathbf{p})$. The path that the aerial robot follows is then $\varphi(x, y) = 0$, or more generally $\varphi(x, y) = h$. $\varphi(\mathbf{p}) - h$ is then the distance on the z-axis.

In this work, we use lines and circles as path functions. We connect these functions using some specific points—the triggering points. However, one can define any mathematical function, with the only requirement being continuity and twice differentiability. We use the first derivative for the vector field, the second derivative to derive the control action. We explain both derivatives further in [Chapter 6](#).

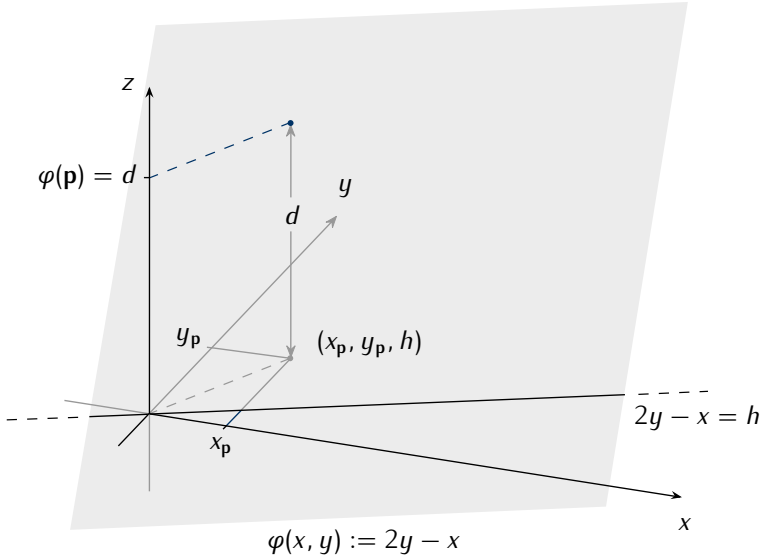


Fig. 2.1. The path defined as mathematical function $\varphi(p(t)) = h$ at a fixed altitude h . A generic point p in 2D space quantifies the distance $\varphi(p(t)) = d$ on the z -axis from h .

2.3 Definitions of stages and triggering points

Parameters are variable values that we use to plan dynamically the path and computations since they influence the computations/motion energy in [Definition 2.1.2](#). The path parameters are real-valued variable values (\mathbb{R}), the computations parameters are integer-valued variable values (\mathbb{Z}). We use the notation $c_{i,j}$ to denote the j th parameter of the i th parameters set c_i

$$c_i = \{c_{i,1}, c_{i,2}, \dots, c_{i,j}, \dots\}. \quad (2.3)$$

The user-defined plan, has a number of stages $i = \{1, 2, \dots\}$, and we assume that at each stage i the aerial robot runs a schedule and travels a path function φ_i using the parameters set c_i . Parameters are bounded. $\underline{c}_{i,j}$ is the lower bound of the parameter $c_{i,j}$, $\bar{c}_{i,j}$ is the upper bound

$$\underline{c}_{i,j} \leq c_{i,j} \leq \bar{c}_{i,j}. \quad (2.4)$$

We assume there are ρ path-specific parameters and σ computations-specific parameters for every stage. This means that the path at stage i can be replanned with ρ path parameters $c_i^\rho := \{c_{i,1}, c_{i,2}, \dots, c_{i,\rho}\}$, while the computations (i.e., the energy-demanding computational task executed on heterogeneous computing hardware in [Definition 2.1.1](#)) with σ computation parameters $c_i^\sigma := \{c_{i,\rho+1}, c_{i,\rho+2}, \dots, c_{i,\rho+\sigma}\}$.

Returning to [Section 2.2](#), by characterization of the path with parameters, we mean that we enhance φ_i with the path parameters c_i^ρ . $\varphi_i : \mathbb{R}^2 \times \mathbb{R}^\rho \rightarrow \mathbb{R}$ is thus a

(continuous twice differentiable) function of a point and the path parameters. The parameters are used to alter the path and thus change the energy consumption. Similarly, by characterization of the schedule with parameters, we mean that we express the computations as the value of the computations parameters. These are also employed for the purpose of energy alteration (by, e.g., decreasing the granularity of a given computation and thus lowering instantaneous energy consumption). We discuss the alteration of the energy with path parameters and computation parameters further in Section 4.4.2 and Section 4.4.3 respectively.

Since at every stage the aerial robot travels a path and executes a schedule both characterized by the parameters, we define the stage as a set containing the path and path and computations parameters.

Definition 2.3.1: Stage

Given $\mathbf{p}(t)$, the i th stage Γ_i at time instant t of a plan Γ is

$$\Gamma_i := \{\varphi_i(\mathbf{p}(t), c_i^\rho), c_i^\sigma \mid \forall j \in [\rho]_{>0}, c_{i,j} \in \mathcal{C}_{i,j}, \\ \forall k \in [\sigma]_{>0}, c_{i,\rho+k} \in \mathcal{S}_{i,k}\},$$

where $\mathcal{C}_{i,j} := [\underline{c}_{i,j}, \bar{c}_{i,j}] \subseteq \mathbb{R}$ is the j th path parameter constraint set, and $\mathcal{S}_{i,k} := [\underline{c}_{i,\rho+k}, \bar{c}_{i,\rho+k}] \subseteq \mathbb{Z}_{\geq 0}$ the k th computation parameter constraint set.

We explain in the next section why they stage contains the generic point of the aerial robot flying in 2D space.

For simplicity, we merge the computation constraint sets and the path constraint set in a single constraint set. The constraint set for the i th stage

$$\mathcal{U}_i := \begin{cases} \mathcal{C}_{i,j} & \text{for } c_{i,j} \text{ with } j \leq \rho \\ \mathcal{S}_{i,j-\rho} & \text{for } c_{i,j} \text{ with } \rho < j \leq \sigma \end{cases}. \quad (2.5)$$

To move from a given stage Γ_i to the next stage Γ_{i+1} , we define some specific points \mathbf{p}_{Γ_i} . As soon as the aerial robot reaches the proximity of these points

$$\mathbf{p}(t) - \mathbf{p}_{\Gamma_i} = \varepsilon, \quad (2.6)$$

where $\varepsilon \in \mathbb{R}$ is a given constant value expressing the radius of an imaginary circle over the point \mathbf{p}_{Γ_i} , it switches to the next stage.

Definition 2.3.2: Triggering, and final point

The point \mathbf{p}_{Γ_i} that allows the transition between Γ_i and Γ_{i+1} is called *triggering point*. The last triggering point \mathbf{p}_{Γ_l} relative to the last stage Γ_l is called *final point*.

2.4 Definition of the plan

Our dynamic planning relies on the concept of the aerial robot flying a set of paths and computations autonomously. Such an autonomous flight plan often presumes a certain degree of periodicity. One can observe the periodicity in the precision agriculture example in [Section 1.3.2](#). An ideal way to monitor the agricultural field in [Figure 1.6](#), is to define a basic pattern. The aerial robot flies over the field once and then iterates the basic pattern until it covers the desired area. It means that the plan can be defined just as a set of stages, triggering points, a final point, and finally a shift which tells the algorithm how these constructs (except final point) shifts in space per each period. We explain this eased definition of the plan later in this section and in the example in [Section 2.6](#). Alternatively, one can define the plan as a mere linear succession of stages along with the triggering and final points. In the latter case, the plan can be either periodic or aperiodic. Aperiodicity affects the energy modeling and thus future energy predictions. We discuss the concrete meaning of periodic, aperiodic, and semi-periodic plans in the context of energy modeling in [Section 4.4](#).

In this section we define the plan in [Definition 2.4.1](#) as a finite state machine using the constructs of path functions in [Definition 2.2.1](#), stage and triggering points in [Definitions 2.3.1–2.3.2](#). We later define the concept of period and shift. It is on the plan's user side to decide to what extent the plan has periodic patterns or a linear succession of stages. We illustrate these two cases in [Figure 2.4](#) and [Figure 2.2](#) respectively. The user has the freedom to define any plan which respects [Definition 2.4.1](#). We illustrate how the design of a plan looks like in [Section 2.6](#).

Definition 2.4.1: Plan

Given $\mathbf{p}(t)$, the *plan* is a finite state machine (FSM) Γ , where the state-transition function $s : \bigcup_i \Gamma_i \times \mathbb{R}^2 \rightarrow \bigcup_i \Gamma_i$ maps a stage and a point to the next stage

$$s(\Gamma_i, \mathbf{p}(t)) := \begin{cases} \Gamma_{i+1} & \text{if } \mathbf{p}(t) - \mathbf{p}_{\Gamma_i} = \varepsilon \\ \Gamma_i & \text{otherwise} \end{cases}.$$

The value ε in [Definition 2.4.1](#) is the same ε in [Equation \(2.6\)](#). We illustrate the definition of plan, stage, triggering, and final points in [Figures 2.2–2.4](#).

In [Figure 2.2](#) we illustrate a simple linear plan. The triggering point $\mathbf{p}_{\Gamma_{i-1}}$ allows the transition to the stage Γ_i . The robot remains in the stage with any generic point $\mathbf{p}(t_2)$, where $t_1 > t_2 > t_3$ are three different time instants. It eventually enters the stage Γ_{i+1} with the triggering point \mathbf{p}_{Γ_i} and so on, until it reaches the final point. Γ_f is the accepting stage (it indicates that the robot has completed the plan). In [Figure 2.3](#) we illustrate that generally, one can express the basic constructs—such as path functions and triggering points—in function of the i th trajectory parameters c_i^ρ , or any previous

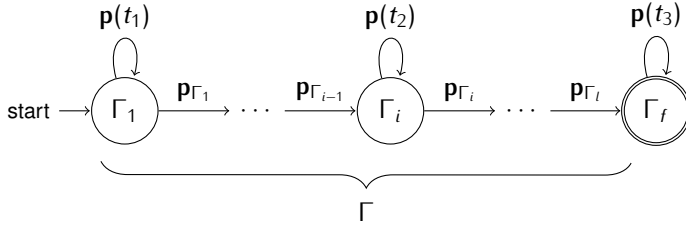


Fig. 2.2. Definition of a plan Γ as an FSM. Each state is a stage Γ_i , the transition happens in proximity of specific points called triggering points p_{Γ_i} . The accepting stage Γ_f indicates the termination of the plan.

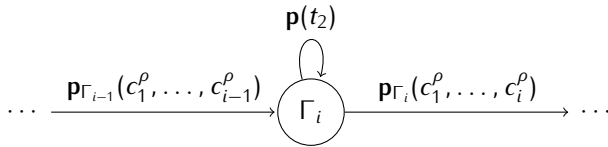


Fig. 2.3. Detail of the stage Γ_i in the FSM. The triggering points used to transition between stages (states in the FSM) are expressed in function of the last and/or previous triggering points.

trajectory parameters, propagating the information therein if necessary. We further expand on this notion in the example in Section 2.6.

In order to simplify the planning problem to the case of periodic plans with a pattern being iterated over time, we consider some *primitive paths*. All the other paths are built from these paths with a shift $\mathbf{d} := (x_d, y_d)$. Let us suppose the plan is composed of l stages. Given $n \in \mathbb{Z}_{>0}$ ($n < l$, $l/n \in \mathbb{Z}$) primitive paths $\varphi_1, \dots, \varphi_n$, a generic starting point $\mathbf{p}(t_0)$ at the initial time t_0 , and some given initial values of the path parameters c_1^ρ , all the other paths $\varphi_{n+1}, \dots, \varphi_l$ are built

$$\varphi_{(i-1)n+j}(\mathbf{p} + (i-1)\mathbf{d}, c_1^\rho) - \varphi_{in+j}(\mathbf{p} + i\mathbf{d}, c_1^\rho) = e_j, \quad (2.7)$$

$\forall i \in [l/n - 1]_{>0}$, $j \in [n]_{>0}$, where $e_j \in \mathbb{R}$ is the j th constant difference.

In Figure 2.4 we illustrate a plan composed of n primitive stages $\Gamma_1, \Gamma_2, \dots, \Gamma_n$ (containing primitive paths $\varphi_1, \varphi_2, \dots, \varphi_n$) that are reiterated with the shift \mathbf{d} . A concept that we use in the remainder of this work, and particularly in energy modeling in Chapter 4 and estimation in Chapter 5, is the concept of period—the time required to fly the primitive paths $\varphi_1, \varphi_2, \dots, \varphi_n$ (or generally $\varphi_{(i-1)n+1}, \varphi_{(i-1)n+2}, \dots, \varphi_{(i-1)n+n}$).

Definition 2.4.2: Period

The period $T \in \mathbb{R}_{>0}$ is the time between $\varphi_{(i-1)n+j}$ and φ_{in+j} in Equation (2.7).

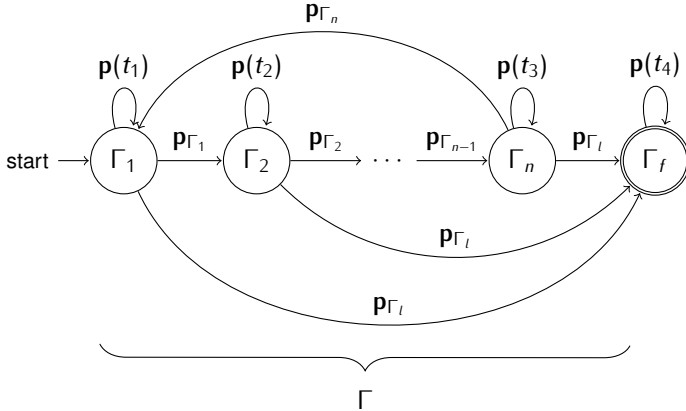


Fig. 2.4. Definition of a plan Γ that contain a loop. Stages $\Gamma_1, \Gamma_2, \dots, \Gamma_i$ containing primitive paths $\varphi_1, \varphi_2, \dots, \varphi_n$ are iterated with a shift d .

We assume the initial period is one and measure the period required to fly the paths physically or in simulation. The periods might be different for different j s due to atmospheric interferences. For the path functions, one can define the plan using primitive paths $\varphi_1, \varphi_2, \dots, \varphi_n$ or define all the stages explicitly and find n searching the value which satisfies the [Equation \(2.7\)](#). If there is no such value, (e.g., when the plan is composed of only one stage or the plan is aperiodic), the period T from [Definition 2.4.2](#) can be determined empirically from energy data or assumed as the total flight time. The latter eventuality has an effect on the energy model. We discuss the period estimation further in [Section 5.4.1](#).

2.5 Planning problem

The planning problem is then the problem of finding the optimal configurations of the parameters within some criteria. In our approach, we focus on energy criteria, such as the battery constraints. In particular, in the solution to the planning problem in [Section 7.6.3](#), we use a cost function (i.e., the function to maximize) which incorporates the energy model in [Section 4.4](#). Solving the planning problem by finding the optimal configurations within different criteria, such as shortest time, highest security, path tracking with the shortest detour, or others is equally possible. In the context of the TeamPlay project that funded a considerable part of this work, we aim to find, for instance, the tradeoffs between time, energy, and security criteria for a variety of use-cases. We discuss the eventuality of solving the planning problem with criteria different from energy in [Chapter 8](#). We now use the concepts that we introduced in

the previous sections and provide a formal definition of the planning problem that we are interested in solving in the remainder of this work.

Problem 2.5.1: Planning problem

Consider an initial plan Γ in Definition 2.3.1. It is either composed of l stages, or n stages and a shift \mathbf{d} . We are interested in the *planning* of the *path* and *computations parameters* c_i , $\forall i \in [l]_{>0}$, or $\forall i \in \{1, 2, \dots\}^a$ under energy constraints and uncertainty.

We are further interested in the guidance to the path and the scheduling of the computations resulting from such planning.

^aThere is a fixed number of stages in case all the stages were defined explicitly. Otherwise there is a variable number of stages in the sense that all the stages are reiterated up until the aerial robot reached the last triggering point \mathbf{p}_l .

2.6 Precision agriculture example

In this section, we discuss an example of a plan for the Opterra autonomous aerial robot in a precision agriculture scenario addressing the covering problem in Figure 1.6. Path-wise, the aerial robot covers a polygon with variable quality of coverage. Computation-wise, it detects ground hazards and communicates eventual detection with other ground-based actors. To simplify the notation, we split the plan into two sub-plans, one containing exclusively the paths and the other the computations. We discuss the paths sub-plan in Section 2.6.1 and the computations sub-plan in Section 2.6.2.

2.6.1 paths sub-plan

In the paths sub-plan, we define the paths that form the plan of the agricultural scenario. We recall that in the scenario, the aerial robot covers the polygon in Figure 1.6 path-wise. For simplicity, we assume the polygon has four sides (it is a rectangle). An intuitive static plan Γ can be composed of lines connected by circles. The distance between the lines can be then used as a measure of the quality of the coverage. Such intuitive static plan is illustrated in Figure 2.5.

The intuitive plan can be used to solve the covering problem with a rotary-wing aerial robot. However, it is unsuitable for a fixed-wing aerial robot such as the Opterra. Fixed-wing aerial robots have considerably reduced maneuverability compared to rotary-wings. They are generally unable to perform quick turns in flight. An updated version of the intuitive plan for fixed-wing aerial robots is illustrated in Figure 2.6. The paths that correspond to the fixed-wing aerial robot's plan are composed of four

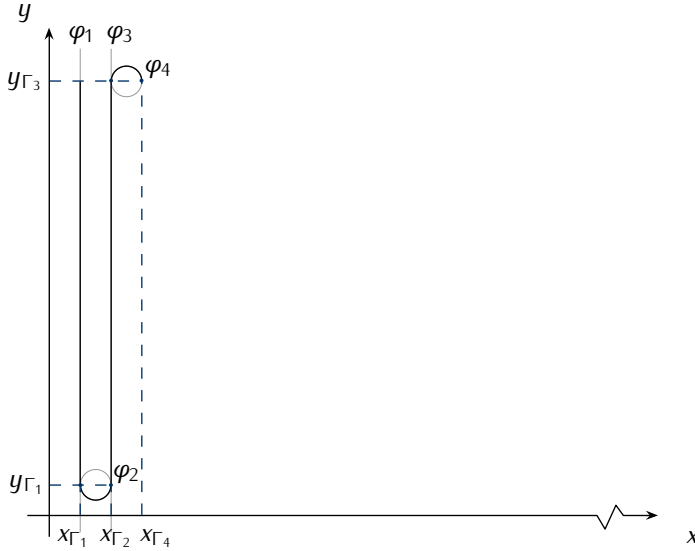


Fig. 2.5. An intuitive plan to cover a regular polygon with four sides. The plan is composed of circles φ_2, φ_4 and lines φ_1, φ_3 . To switch between paths the aerial robot reaches the proximity of triggering points ($\mathbf{p}_{\Gamma_1} := (x_{\Gamma_1}, y_{\Gamma_1}), \mathbf{p}_{\Gamma_2}, \mathbf{p}_{\Gamma_3}, \mathbf{p}_{\Gamma_4}$). The dashed blue line indicates the triggering points, and the black line is the planned flight. The rest of the polygon is covered iterating these primitive paths $\varphi_1, \varphi_2, \varphi_3, \varphi_4$.

primitives

$$\varphi_1(\mathbf{p}(t)) := x - 10, \quad (2.8a)$$

$$\varphi_2(\mathbf{p}(t)) := (x - 85)^2 + (y - 10)^2 - 5625, \quad (2.8b)$$

$$\varphi_3(\mathbf{p}(t)) := x - 160, \quad (2.8c)$$

$$\varphi_4(\mathbf{p}(t)) := (x - 90)^2 + (y - 140)^2 - 4900, \quad (2.8d)$$

where x, y are the x - and y -coordinates of a generic point $\mathbf{p}(t)$. The triggering points (the points in which proximity occurs the change of stages) are then the points

$$\mathbf{p}_{\Gamma_1} := (10, 10), \mathbf{p}_{\Gamma_2} := (160, 10), \mathbf{p}_{\Gamma_3} := (160, 140), \mathbf{p}_{\Gamma_4} := (20, 140). \quad (2.9)$$

The covering problem can be solved using the paths in [Equation \(2.8\)](#), the triggering points in [Equation \(2.9\)](#), the remaining paths $\varphi_5, \varphi_6, \dots, \varphi_l$, and triggering points $\mathbf{p}_{\Gamma_5}, \mathbf{p}_{\Gamma_6}, \dots, \mathbf{p}_{\Gamma_l}$ defined similarly to [Equations \(2.8–2.9\)](#). A generic solution for the covering problem is then defined with the paths

$$\varphi_i(\mathbf{p}(t)) := x - x_{\Gamma_1} - \lfloor i/4 \rfloor x_d, \quad (2.10a)$$

$$\varphi_{i+2}(\mathbf{p}(t)) := x - x_{\Gamma_2} - \lfloor i/4 \rfloor x_d, \quad (2.10b)$$

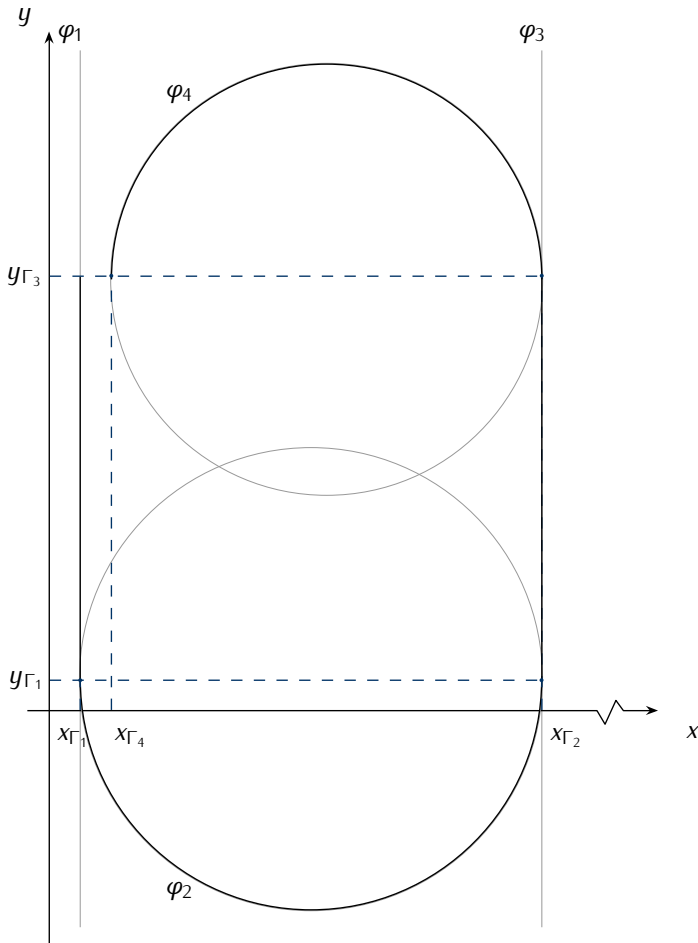


Fig. 2.6. Fixed-wing aerial robot plan to cover a regular polygon with four sides. The plan covers the polygon with the same principle of the intuitive plan in [Figure 2.5](#) but preserving long turns necessary for the flight of a fixed-wing craft. Likewise in [Figure 2.5](#), the entire polygon is covered iterating the primitive paths $\varphi_1, \varphi_2, \varphi_3, \varphi_4$ (gray lines). The dashed blue line indicates the triggering points, and the black line is the planned flight. The height and length of the polygon are $y_{\Gamma_3} - y_{\Gamma_1}$ and $lx_d/4$.

$\forall i \in \{1, 5, 9, \dots, l-3\}$ (i is used to iterate all the paths up to the last path φ_l), x_d is a shift on the x -axis, $\lfloor i/4 \rfloor$ is the integer division. The expressions in [Equation \(2.10\)](#) correspond to the generalizations of the lines in [Equation \(2.8a\)](#) and [Equation \(2.8c\)](#). The generalizations of the circles in [Equation \(2.8b\)](#) and [Equation \(2.8d\)](#) are

$$\varphi_{i+1}(\mathbf{p}(t)) := (x - x_{\Gamma_1} - r_1 - \lfloor i/4 \rfloor x_d)^2 + (y - y_{\Gamma_1})^2 - r_1^2, \quad (2.11a)$$

$$\varphi_{i+3}(\mathbf{p}(t)) := (x - x_{\Gamma_2} + r_2 - \lfloor i/4 \rfloor x_d)^2 + (y - y_{\Gamma_3})^2 - r_2^2, \quad (2.11b)$$

where index i is defined the same way as in [Equation \(2.10\)](#) along the shift and integer division. r_1 and r_2 are given radii of the circles φ_2 and φ_4 (see [Figure 2.6](#)).

The triggering points can be expressed similarly with the expressions

$$\mathbf{p}_{\Gamma_i} := (x_{\Gamma_1} + \lfloor i/4 \rfloor x_d, y_{\Gamma_1}), \quad (2.12a)$$

$$\mathbf{p}_{\Gamma_{i+1}} := (x_{\Gamma_1} + 2r_1 + \lfloor i/4 \rfloor x_d, y_{\Gamma_1}), \quad (2.12b)$$

$$\mathbf{p}_{\Gamma_{i+2}} := (x_{\Gamma_1} + 2r_1 + \lfloor i/4 \rfloor x_d, y_{\Gamma_3}), \quad (2.12c)$$

$$\mathbf{p}_{\Gamma_{i+3}} := (x_{\Gamma_1} + 2r_1 - 2r_2 + \lfloor i/4 \rfloor x_d, y_{\Gamma_3}). \quad (2.12d)$$

We note from [Figure 2.6](#) and [Equations \(2.10–2.12\)](#) that $y_{\Gamma_3} - y_{\Gamma_1}$ is the height of the polygon to be covered, $2(r_1 - r_2)$ the distance between the covering lines (which is equal to the shift x_d), and $lx_d/4$ is the length of the polygon.

The plan in [Equations \(2.10–2.12\)](#) is static. There is no path parameter that allows to alter the plan. We can easily transform such plan with the addition of a path parameter $c_{4,1}$ relative to the radius of the second circle φ_4 in [Figure 2.6](#)

$$r_2(c_{4,1}) := (r + c_{4,1}), \quad (2.13)$$

where $r < r_1$ is a given positive constant initial radius and $c_{4,1} \in (-r, 0]$. We assume that the highest value is thus $\bar{c}_{4,1} = 0$, the lowest is strictly higher than the constant initial radius $\underline{c}_{4,1} > -r$.

We note from the expression in [Equation \(2.13\)](#) that [Equation \(2.12d\)](#) and [Equation \(2.11b\)](#) depend on the parameter $c_{4,1}$ (they contain r_2 , which depend on $c_{4,1}$). They can be thereby dynamically replanned, resulting in an alteration of the quality of the coverage. They indeed change the distance between the survey lines. We can bound the alteration with

$$c_{i,1} \in [\underline{c}_{4,1}, \bar{c}_{4,1}] := \mathcal{C}_{4,1} = (-r, 0], \quad \forall i. \quad (2.14)$$

The concept is illustrated in [Figure 2.7](#). The black line is the un-altered path, the blue line the replanned path. The gray area delimits the bound $\mathcal{C}_{4,1}$. The alteration of the plan using path parameter $c_{4,1}$ shortens or extends the flying time and thus influence the energy consumption over time. Since the last path φ_4 is a function of the parameter $c_{4,1}$, the correct expression for [Equation \(2.11b\)](#) is

$$\varphi_{i+3}(\mathbf{p}(t), c_{4,1}) := (x - x_{\Gamma_2} + r_2(c_{4,1}) - \lfloor i/4 \rfloor x_d)^2 + (y - y_{\Gamma_3})^2 - r_2(c_{4,1})^2. \quad (2.15)$$

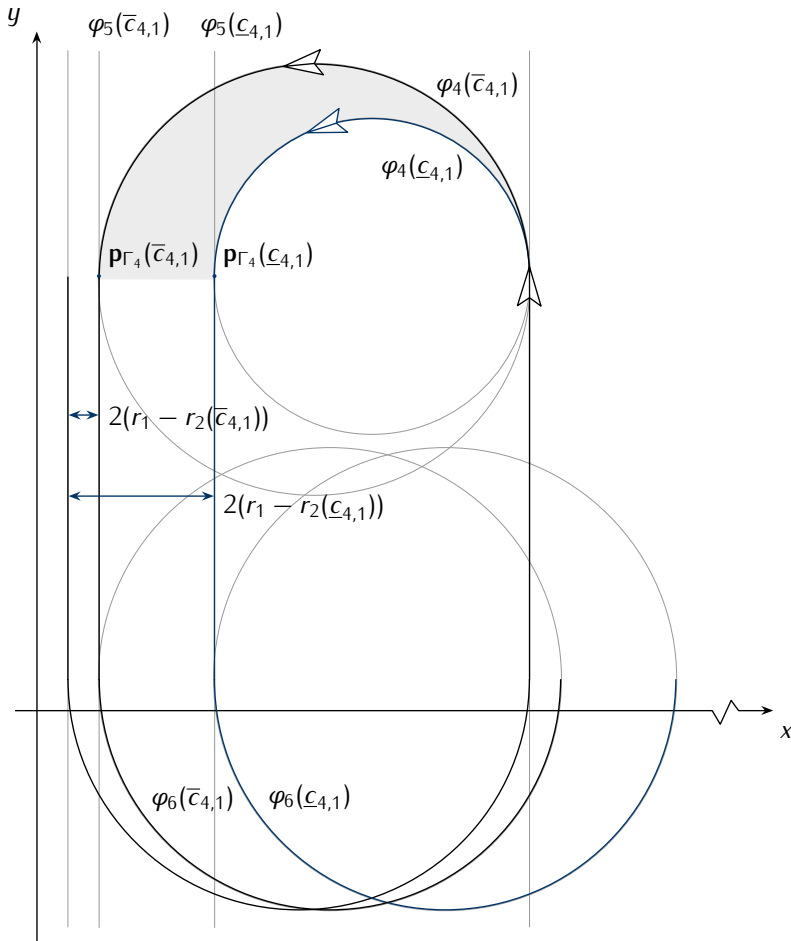


Fig. 2.7. Alteration of a path parameter of the fixed-wing aerial robot's plan in Figure 2.6. The black line is the un-altered path, the dashed blue line the altered path. The gray area delimits the bound $\mathcal{C}_{4,1}$. The alteration changes the distance between the survey lines hence extending or shortening the flying time. The figures show the concept for the path parameter $c_{4,1}$. Same principle applies to path parameter $c_{8,1}$ for the next two survey lines, $c_{12,1}$, and so on.

The last triggering point \mathbf{p}_{Γ_4} of the example in [Equation \(2.12d\)](#) is likewise a function of the parameter $c_{4,1}$,

$$\mathbf{p}_{\Gamma_{i+3}} := (x_{\Gamma_1} + 2r_1 - 2r_2(c_{4,1}) + \lfloor i/4 \rfloor x_d, y_{\Gamma_3}) \quad (2.16)$$

as it depends on the radius r_2 of the circle φ_4 . The same applies to all the following functions $\varphi_5, \varphi_6, \varphi_7$, since these are all a function of the triggering point \mathbf{p}_{Γ_4} . The path φ_8 is then a function of the parameter $c_{4,1}$ and $c_{8,1}$ propagating the parameters for all the following paths $\varphi_9, \varphi_{10}, \varphi_{11}$ and so on.

2.6.2 Computations sub-plan

In the computations sub-plan, we define the computations that form the plan of the agricultural scenario, opposed to the paths that we defined in the previous section. In the scenario, we are interested in monitoring the field in [Figure 1.6](#), and thus in the detection ground hazard and communication with the some others ground-based actors. To detect the ground hazard we utilize a CNN implemented in a Robot Operating System (ROS) ([Quigley et al., 2009](#)) node. The CNN detects hazards from image frames from a downward-facing camera on the aerial robot. To communicate with ground-based actors, we assume there is one centralized work station on the ground. The communication between the aerial robot and the centralized work station occurs on another ROS node, which utilizes the technical standard for wireless communication IEEE 802.11 ([Crow et al., 1997](#)). It sends the detected images either unencrypted or using public key infrastructure for encryption. We refer to this two computations as CNN and encryption ROS nodes respectively. Their schedule is characterized by the FPS rate for the CNN ROS node, by a binary value which indicate whenever the encryption is enabled for the encryption node.

There are two computations parameters. A computation parameter is the FPS rate at which the frames are sent from the camera to the CNN ROS node, and another computation parameter says whenever the communication between the aerial robot and the work station is encrypted. For simplicity, we assume that we have the same computations for all the stages in the plan. The CNN ROS node computation parameter is $c_{i,2}$, and to the encryption ROS node computation parameter is $c_{i,3}$.

The upper and lower bounds of $c_{i,3}$ are

$$c_{i,3} \in \{0, 1\} := \mathcal{S}_{i,3}, \forall i \quad (2.17)$$

the parameter value is binary and it indicates if the encryption is active (one) or data are sent unencrypted (zero).

For the upper and lower bound of $c_{i,2}$, we first note from the path plan in [Section 2.6.1](#) that during the turns the aerial robot is not surveying the polygon. We thus place different constraints for different paths. For the circles in [Equation \(2.20b\)](#) and

Equation (2.20d) the computation parameter constraint set are

$$c_{i+1,2}, c_{i+3,2} \in \mathcal{S}_{i+1,2} = \mathcal{S}_{i+3,2} := \{0\}, \forall i \in \{1, 5, 9, \dots\}, \quad (2.18)$$

and thus the CNN ROS node is not detecting any hazard when it flies out of the polygon. On the contrary, for the lines in Equation (2.20a) and Equation (2.20c)

$$c_{i,2}, c_{i+2,2} \in \mathcal{S}_{i,2} = \mathcal{S}_{i+2,2} := [2, 10], \forall i \in \{1, 5, 9, \dots\}, \quad (2.19)$$

the the CNN ROS node is detecting hazard on the ground with a FPS rate between two and ten.

Energy-wise we expect the highest configuration of computations parameters to correspond to the highest instantaneous energy consumption. We use `powprofiler`, the profiling and modeling tool that we briefly outlined in [Section 1.4](#) and that we introduce in [Section 4.1](#), to measure and model the future energy consumption of different computations configurations.

2.6.3 Planning problem with paths and computations sub-plans

The plan for the precision agriculture scenario is thus composed of stages containing the primitive paths in [Equations \(2.10–2.11\)](#), and the parameter dependent version in [Equation \(2.15\)](#). It further contains the path parameter $c_{i,1}$, the computations parameters $c_{i,2}$ and $c_{i,3}$, and some given triggering and final points. In particular, the stages corresponding to the primitive paths are

$$\Gamma_i := \{\varphi_i(\mathbf{p}(t), c_{4,1}, c_{8,1}, \dots, c_{i-1,1}), c_{i,2}, c_{i,3}\}, \quad (2.20a)$$

$$\Gamma_{i+1} := \{\varphi_{i+1}(\mathbf{p}(t), c_{4,1}, c_{8,1}, \dots, c_{i-1,1}), c_{i+1,2}, c_{i+1,3}\}, \quad (2.20b)$$

$$\Gamma_{i+2} := \{\varphi_{i+2}(\mathbf{p}(t), c_{4,1}, c_{8,1}, \dots, c_{i-1,1}), c_{i+2,2}, c_{i+2,3}\}, \quad (2.20c)$$

$$\Gamma_{i+3} := \{\varphi_{i+3}(\mathbf{p}(t), c_{4,1}, c_{8,1}, \dots, c_{i-1,1}, c_{i+3,1}), c_{i+3,2}, c_{i+3,3}\}, \quad (2.20d)$$

$\forall i \in \{1, 5, 9, \dots\}$. The path constraint set for the path parameter $c_{i,1}$ is then defined in [Equation \(2.14\)](#), the computation constraint set for the computation parameter $c_{i,2}$ in [Equation \(2.18\)](#) and for the computation parameter $c_{i,3}$ in [Equation \(2.19\)](#). The triggering points

$$\mathbf{p}_{\Gamma_i}(c_{4,1}, \dots, c_{i-1,1}) := (x_{\Gamma_{i-4}}(c_{4,1}, \dots, c_{i-1,1}) + \lfloor i/4 \rfloor x_d, y_{\Gamma_1}), \quad (2.21a)$$

$$\mathbf{p}_{\Gamma_{i+1}}(c_{4,1}, \dots, c_{i-1,1}) := (x_{\Gamma_{i-4}}(c_{4,1}, \dots, c_{i-1,1}) + 2r_1 + \lfloor i/4 \rfloor x_d, y_{\Gamma_1}), \quad (2.21b)$$

$$\mathbf{p}_{\Gamma_{i+2}}(c_{4,1}, \dots, c_{i-1,1}) := (x_{\Gamma_{i-4}}(c_{4,1}, \dots, c_{i-1,1}) + 2r_1 + \lfloor i/4 \rfloor x_d, y_{\Gamma_3}), \quad (2.21c)$$

$$\begin{aligned} \mathbf{p}_{\Gamma_{i+3}}(c_{4,1}, \dots, c_{i+3,1}) := & (x_{\Gamma_{i-4}}(c_{4,1}, \dots, c_{i-1,1}) + 2r_1 - 2r_2(c_{i+3,1}) \\ & + \lfloor i/4 \rfloor x_d, y_{\Gamma_3}). \end{aligned} \quad (2.21d)$$

$\forall i \in \{5, 9, \dots\}$. The initial points x_{Γ_1} , y_{Γ_1} , and y_{Γ_3} are given along the shift x_d on the x -axis, and the radius of the larger circle r_1 . The function r_2 which returns the radius of the smaller circle and it is a function of the path parameter $c_{i,1}$, $\forall i \in \{4, 8, \dots\}$ is given in [Equation \(2.13\)](#). The last triggering point \mathbf{p}_l is likewise given.

The solution to the planning problem is thus the three trajectories $c_i^*(t) = \{c_{i,1}^*(t), c_{i,2}^*(t), c_{i,3}^*(t)\}$, $\forall i \in \{1, 2, \dots\}$ that are optimal energy-wise under given energy constraint and uncertainty. Given that each quadruple of stages in [Equation \(2.20\)](#) and triggering points [Equation \(2.21\)](#) depends only on the last path parameter (of the quadruple), we further assume that $c_{1,1} = c_{1,2} = c_{1,3} = c_{1,4}$ and more generally

$$c_{i,1} = c_{i+1,1} = c_{i+2,1} = c_{i+3,1}, \forall i \in \{1, 5, 9, \dots\}. \quad (2.22)$$

We derive the solution for the planning problem of the precision agriculture example in [Section 7.6.1](#).

2.7 Summary

Chapter 3

State of the Art

3.1 Energy Modeling

Marowka developed a power-metrics based analytical model, to exploit the possibility of considerably increasing energy efficiency by choosing an optimal chip configuration, which we extended to evaluate the impact of different architectural design choices on energy efficiency ([Marowka, 2017](#)). Marowka's theoretical contribution shows three processing schemes for heterogeneous computing with a comparison of their respective energy efficiency. Variations in chip configurations are done to investigate the impact on energy, power, and performance. Symmetric processor scheme consists of only a multicore CPU. Asymmetric CPU-GPU processor scheme consists of both CPU and GPU on the hardware side, and of a program running on CPU or GPU, but not on both in the same time interval, on the software side. CPU-GPU simultaneous processing scheme consists of a program running on CPU and GPU simultaneously. Our work extends and starts from Marowka's approach by building an experimental method to the CPU-GPU simultaneous processing scheme.

For evaluating the effects of a battery as an energy source, we used the work done by ([R. Rao et al., 2003](#)). Their work summarizes state-of-the-art battery modeling into four classes of models that capture the battery state and its non-linearities. The lowest class contains the physical models that are accurate and model battery state evolution through a set of ordinary and partial differential equations. However, they suffer from a significant level of complexity that reflects on the time needed to produce predictions. The work proceeds by showing empirical models, that predict battery state from empirical trials. The third class consists of abstract models that we incorporated into our approach, in particular, by deriving the equation from the model developed by ([Hasan et al., 2018](#)) (they model battery state through an equivalent electrical circuit and its

evolution in time). The fourth class consists of mixed models where experimental data are collected and subsequently refined with analytical expressions to determine the models' parameters.

System-level optimization techniques, such as dynamic voltage scaling, have been used for lowering the power consumption (Chowdhury and Chakrabarti, 2005; I. Hong et al., 1999; Luo and Jha, 2001). These techniques are available for hardware featuring dynamic voltage scaling and aim to achieve higher energy efficiency by including information about configuration parameters into the scheduler. They however focus on homogeneous systems, unlike our work which is designed to work for heterogeneous systems. This approach to modeling has nevertheless been extended to include GPU features (S. Hong and H. Kim, 2010), to heterogeneous systems (Bailey et al., 2014), to optimal software partitioning (Goraczko et al., 2008), and by Wu et al. to machine learning techniques (Wu et al., 2015). The work by Wu et al. mostly relies on neural networks and has been introduced only recently in the field of power estimation and modeling for heterogeneous systems. In particular, for a collection of applications, Wu et al. train a neural network by measuring a number of performance counters for different configurations. Even if these techniques perform well for defining static optimization strategies, they are generally not suitable for heterogeneous parallel systems in aerial robotics. In these cases, systems suffer from a considerable level of uncertainty, for which reason a statically defined energy model often would not model the real energy behavior. An overview of energy estimation in the context of machine learning approaches has recently been presented by (García-Martín et al., 2019). They present a literature review motivated by a belief that the machine learning community is unfamiliar with energy models, but do not relate to GPU-featured devices nor in general heterogeneous devices. In contrast, in our work we aim at automating the generation of application-level power estimation models that can be adapted for machine learning algorithms. Our approach does not yet take detailed scheduling decisions into account, unlike the black-box approach for CPU-GPU energy-aware scheduling presented by (Barik et al., 2016): they model the power by relating execution time to power consumption but otherwise do not focus on energy models.

Our approach shares the same principle of differentiating the microcontroller from the companion computer with (Mei et al., 2004, 2005). The controller acts on the actuators and reads the sensors, while the companion computer (can be found with different names in literature, such as secondary or embedded computer), performs computationally heavy operations. A similar approach for mobile robots is presented by (Dressler and Fuchs, 2005). However, both contributions neither elaborate further on computational elements of a heterogeneous platform, such as GPU, nor focus on different robots except the one under analysis.

The majority of other contributions in the literature focus on optimizing motion planning to increase power efficiency. For instance, approaches to minimize UAV

power consumption, such as the work by (Kreciglowa et al., 2017), aim to determine the best trajectory generation method for an aerial vehicle to travel from one configuration to another. Uragun suggests the use of power-efficient components (Uragun, 2011): an energy-efficient UAV system can either be built using conceptual product development with emerging technologies or using energy-efficient components. Kanellakis et al. affirm that integrating visual sensors in the UAV ecosystem still lacks solid experimental evaluation (Kanellakis and Nikolakopoulos, 2017). They suggest that to save energy, the available payload for sensing and computing has to be restricted. Our approach towards energy modeling shares a similar principle as the one presented by (Sadpour et al., 2013a,b) for Unmanned Ground Vehicles or UGVs. They propose a linear regression-based technique in the absence of real measurements and a Bayesian networks-based one in their presence. We used a simplified approximation technique to limit the number of computations needed while focusing rather on an accurate battery prediction.

To validate our approach and quantify its outcomes, we used the models previously developed for fine-grained energy modeling by (Nunez-Yanez and Lore, 2013), and (Nikov et al., 2015) respectively. In summary, fine-grained energy modeling uses hardware event registers to capture the CPU state under a representative workload. The energy-modeling consists of three stages. In data collection, the first stage, a benchmark runs on the platform and data are collected. The second and third stage, data processing and model generation, are performed offline on a different architecture. In these two stages, data are analyzed and a model that predicts possible future usage is generated.

Calore et al. develop an approach for measuring power efficiency for High-Performance Computing or HPC systems (Calore et al., 2015). An external board is used to measure the power consumption, while the data are collected from NVIDIA Jetson TK1 board running one benchmark. Our initial analysis presented at HLPGPU 2019 was made using a similar technique (Seewald, Ebeid, et al., 2019). A shunt resistor and digital multimeter integrated into the external board was used to evaluate the power efficiency. In this paper we extend our experiments to use internal power monitors and address a broader range of platforms. We now build a proper energy model that reflects the computational behavior of the device under study and shows the energy evolution. An early report on our work has been presented in the TeamPlay project's deliverable D4.3 (*Public Deliverables of the TeamPlay Horizon2020 Project 2019*) "Report on Energy, Timing and Security Modeling of Complex Architectures".

3.2 Motion Planning

Planning algorithms literature for mobile robots includes topics such as trajectory generation and path planning. Generally, the algorithms select an energy-optimized

trajectory [Mei et al., 2004](#), e.g., by maximizing the operational time [Wahab et al., 2015](#). However, they apply to a small number of robots [C. H. Kim and B. K. Kim, 2005](#) and focus exclusively on planning the trajectory [H. Kim and B.-K. Kim, 2008](#), despite compelling evidence for the energy consumption also being significantly influenced by computations [Mei et al., 2005](#). Given the availability of powerful GPU-equipped mobile hardware [Rizvi et al., 2017](#), the use of computations is expected to increase in the near future [Abramov et al., 2012](#); [Jaramillo-Avila et al., 2019](#); [Satria et al., 2016](#). More complex planning, which includes a broader concept of the plan being a set of tasks and a path, all focus on the trajectory [Mei et al., 2005, 2006](#) and apply to a small number of robots [Sadrpour et al., 2013a,b](#). For UAVs specifically, rotorcrafts have also gained interest in terms of algorithms for energy-optimized trajectory generation [Kreciglowa et al., 2017](#); [Morbidi et al., 2016](#).

3.3 Planning with Dynamics

3.4 Planning for Autonomous Aerial Robots

3.4.1 Flight controllers

3.4.2 Energy models in aerial robotics

3.4.3 State estimation in aerial robotics

3.4.4 Optimal control in aerial robotics

3.5 Planning Computations with Motion

3.6 Summary

Chapter 4

Energy Models

4.1 Energy Model of the Computations

Numerous new challenges have been introduced in embedded systems through evolution from small and predictable to large and complex architectures featuring different computational units. Limited energy availability, security considerations, and time requirements are among the most common challenges and significantly impact the level of autonomy of modern heterogeneous systems. These systems use many-core architectures, where a CPU executes along a general-purpose GPU or GPGPU with energy-efficient small cores. A parallel CPU-GPU execution is a core aspect to achieve the best possible energy efficiency and speed-up (Woo and Lee, 2008).

In this paper, we focus on limited energy availability for mobile heterogeneous devices powered by a battery and present a coarse-grained computation-oriented energy modeling approach.

The model *describes energy usage as a function of component configuration* and is based on physical measurements of power consumption of the on-board computing elements.

The term *computing* is used here to denote the energy consumed by the software components of a complex embedded system. Estimates indicate that more than 50% of power consumption of complex devices featuring mechanical and computational units can occur due to computational operations, with the motion accounting for the remaining (Mei et al., 2004, 2005). Energy efficiency concerns are not limited to battery-powered devices, but also to the high-end systems (Mudge, 2001), and thus it is becoming more important for computer architects as power consumption is growing with the introduction of new processors.

Complex software applications are often composed of many components interacting concurrently to achieve a specific functionality. Our approach aims to predict the energy consumption of a provided set of software components, in a specific configuration, executed according to a given scheduling policy. Statistical methods are used to derive a predictive model allowing prediction of the components' total power consumption as scheduling and configuration parameters are varied. High-level modeling of using a battery as energy-source is used to model the energy that would be drained from the system during computation. The energy model is segmented into two layers: the measurement layer, which describes energy consumption as a function of time, and the predictive layer, which describes energy consumption as a function of component configuration and scheduling. The model generation process starts from the developer, who specifies the configuration space within which software components can run on a given system. A profiling process collects power samples for every component configuration (measurement layer). A model that maps configuration parameters to an energy metric, such as overall energy or average power, is generated from the data, showing the energy evolution for every possible configuration (predictive layer).

4.1.1 Computational energy of the aerial robot

We use software for drones as a case study for energy efficiency. Drones (known also as aerial robots, Unmanned Aerial Vehicles, or UAVs) are often composed of two computational units. A controller that manages real-time control of the physical aspects of the drone, and a companion computer that handles heavy computations. The latter is often a heterogeneous parallel system. A coarse-grained model of these systems can be used for energy-aware planning and optimization from a computational point of view. Moreover, energy constraints are of particular interest for drones, since their level of autonomy is directly proportional to the power-to-compute (Fabiani et al., 2007). Unlike their grounded counterparts, drones must trade-off size, weight, and power, resulting in strict limits to their energy source that may not accommodate their computational needs. Operating from a limited energy source, typically a lithium-ion battery, can significantly reduce the amount of autonomy that the drone can carry on. One of the reasons why this happens is the high energy demand required by complex parallel algorithms used in several use cases, from computer vision to data processing. To this extent, many tasks in aerial robotics are still not fully autonomous. Advanced operations that require a significant level of autonomy, such as path planning, obstacle avoidance, environment mapping, and object detection, often involve human interaction. Thus there is still little difference between flying robots and their manned counterparts, except that the pilot operates from a ground station rather than onboard (Siciliano and Khatib, 2016).

As a concrete example, we present the drone use case that recognize an object while performing some computationally heavy operations. The use case is composed of two components, object detection algorithm (`darknet-gpu`) that recognize a pattern using a neural network, and matrix exponentiation (`matrix-gpu`) that simulates heavy operations with varying scheduling patterns using sleep of different durations between consecutive operations. Both the components execute mostly on GPU. In a configuration file, the developer specifies these parameters per component:

- a) for `darknet-gpu` a frame-per-seconds rate [5.8, 32] from the lowest acceptable, to the highest achievable, and
- b) for `matrix-gpu` two sets of rates, the matrix size [256, 4096] from smallest to largest, and sleep interval [0, 10] from no sleep to 10 seconds.

A profiling process generates models that map time to power, one per combination in the configuration file. Based on this a high-level model is generated which combines component parameters to energy consumption. The energy consumption is estimated for any parameter combinations not profiled. This information is useful to define a proper trade-off between parameters and decide eventually, what configuration has to be used to optimize energy consumption. The information about the battery state, included in the analysis, enables the developer to select a specific run-time configuration (for instance, one that will allow completing the mission without recharging the battery by just adjusting the combinations of components and their parameters).

In our experiments, the resulting model shows an almost linear behavior for the `darknet-gpu` component, highlighting the energy behavior for any configuration in the interval [5.8, 32]. The `matrix-gpu` model shows the energy evolution with different scheduling options and addresses the impact of different scheduling to the battery depletion. Results for both components are presented and further discussed in Section ??.

With this work we have:

1. designed a computation-oriented energy modeling approach for heterogeneous platforms,
2. evaluated the outcomes of the model on several benchmarks and devices,
3. assessed the model's validity against external measurements and a fine-grained approach, and
4. developed a profiling tool for computation-oriented energy modeling.

The tool, named `powprofiler`, is written in C++ and distributed under MIT license.¹ The tool was used to perform all of the experiments reported in this paper and is de-

¹<https://bitbucket.org/adamseew/powprofiler>

signed to be used, among others, in mobile robotics scenarios. It can profile a set of components being executed in a number of possible configurations and from this, build an energy model. The model allows the system under analysis to define an appropriate tradeoff between consumed energy and computations performed. This information can be used to increase energy efficiency, often linked to the level of autonomy in many modern scenarios, and meet the power requirements. For example, a drone can dynamically adjust autonomous detection capabilities to fit the current battery state of charge (referred to in this paper as SoC). Similarly, an autonomous vehicle can increase the amount of computation only when the collision detection system is required, and a mobile robot can automatically schedule tasks to compute in an energy-aware fashion. In these examples, awareness of precise computational energy cost can potentially lead to significant energy savings. Key to the approach is flexibility in terms of easy support for different heterogeneous platforms and extensibility to other classes of systems outside the mobile robotics domain.

4.1.2 Energy modeling for heterogeneous hardware

In this paper, we aim to provide a tool for automatic generation of hardware-specific energy models of a given application. The energy model is generated through a profiling process which collects several power samples and builds an energy abstraction upon them. Computational energy is addressed by mapping a component configuration to an energy metric, such as average power or overall energy. Our approach includes several on-board computing elements, such as CPU and GPU, and analyzes their role in the tradeoff related power decisions.

Figure 4.1 shows an overview of our approach. For a specific application on the system under study, the developer describes how components behave in a configuration file. For each component, any parameter range or value can be specified. By varying the parameters and scheduling policy, the tool generates n combinations of components called configurations $\mathcal{D} = \{d_1, d_2, \dots, d_n\}$. Once the set \mathcal{D} is generated, the profiling process starts by collecting a set of samples and by generating a layer 1 model for every configuration d_k (with $1 \leq k \leq n$). The layer 1 model maps a time interval t to a power measure $f(t)$ and estimates the power-to-compute value for a given component. Later, the model is integrated with battery state evolution and quantified in the amount of SoC left in the battery. Finally, both $f(t)$ and SoC are used to generate a layer 2 model, that maps a set of configurations \mathcal{D} to the energy metric (i.e., average power consumption or overall energy usage) and SoC $g(\mathcal{D})$. This information can be used to select the best configuration and define a better scheduling policy to optimize the average computational energy.

The modeling approach is tested across four different platforms, ODROID XU3, NVIDIA TK1, TX2, and Nano (see Section ?? for details), and a selection of bench-

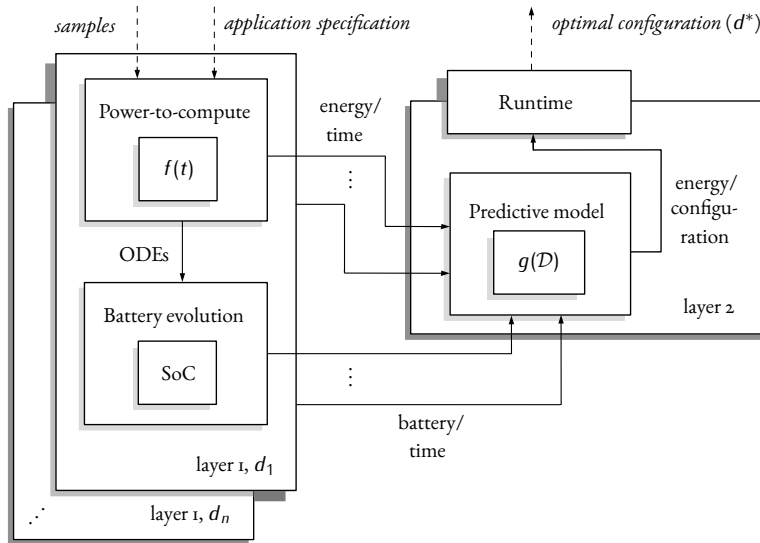


Fig. 4.1. Overview of energy modeling for heterogeneous hardware.

mark components is used. Each component has a set of configuration parameters varied inside defined boundaries, that represent the acceptable rate of quality of service or QoS. We use the following benchmark components: a random matrix of a predefined size that is multiplied by another or exponentiated by a given exponent on CPU (`matrix-cpu`) or GPU (`matrix-gpu`). A computer vision component built upon the darknet (Redmon, 2013–2016; Redmon and Farhadi, 2017) implementation of the YOLO library (Redmon, Divvala, et al., 2016), that uses a deep neural network to detect an object from a video stream on CPU (`darknet-cpu`) or GPU (`darknet-gpu`), and NVIDIA custom-made benchmarks, modified so they can be iterated several times over a time interval, that perform matrix multiplication (`nvidia-matrix`) and quicksort (`nvidia-quicks`) of a given size on GPU.

4.1.3 Measurement layer

The measurement layer describes an energy sample for a given configuration and scheduling of a component executed on specific hardware as a function of time. It provides average power or overall energy over a time interval for every computational unit that allows power measurement.

The developer provides for every application a number of components in the configuration file along with their parameters. An application in this layer is structured as several configured components that execute in parallel according to a specific scheduling policy. First, immediate power consumption is measured. This information is used

to model the power into the power-to-compute and battery drain. An *application specification*, described later in this section, is used to define all the possible configurations of an application in the configuration file. The power is measured throughout a time interval set by the developer. Multiple metrics can be captured at this level and sampled at a fixed rate specified in the application specification, including CPU, GPU, and total power. Other metrics, as the system’s load and sensors’ evolution, can be added by extending the approach. Based on the information obtained at this layer, the energy that the computation would draw from a battery can be estimated using the *battery model*, also described later in this section. As a concrete example, Figure ?? shows the total energy usage as a function of time for CPU and GPU of the NVIDIA TX2 board executing the `darknet-gpu` component in four different QoS configurations.

4.1.4 Application specification

The application specification is used to define all the computations to run for a specific energy model. It depends on the schedule that is used when performing measurements, in the sense that scheduling policies will be specific to the kind of scheduling supported by this scheduler. Currently, only a basic application specification is supported that corresponds to the capabilities of the `powprofiler` tool described later in Subsection ???. Support for more advanced models is considered future work. In particular, a dynamic measurement-oriented scheduler should be adopted in the future to define the optimal scheduling policy during computation.

The basic application specification is defined as follows. The choice between component implementations (if needed) is implicitly supported by requiring the developer to select the specific component implementation to use for the measurement. Components are configured by providing concrete, fixed values for all of their configuration parameters. A scheduling policy is implicitly supported by requiring each component to provide parameters that explicitly control fixed scheduling patterns in time (e.g., what rate to execute, when to execute). Components are assumed to implicitly control scheduling in space, for example by having different implementations for CPU and GPU (and hence being explicitly selected as part of the application configuration).

4.1.5 Predictive layer

The predictive model is expressed in terms of the measurement layer and describes “average power over time frame” and other similar coarse-grained metrics as a function of component configuration parameters and scheduling policies.

The predictive model concerns the average power over a time frame as a function of varying application models (i.e., configuration parameters, scheduling policy, …). The average power can be any of the outputs of the measuring layer, such as aver-

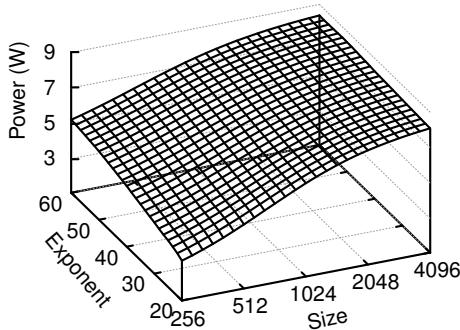


Fig. 4.2. Average power

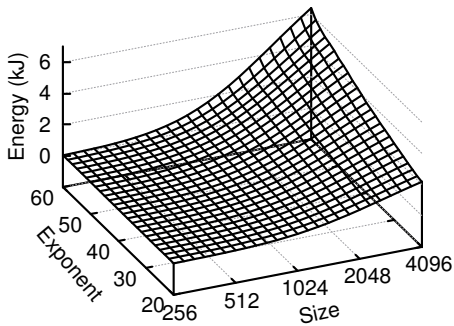


Fig. 4.3. Overall energy

age power used by the embedded board, or average power drained from a battery. First-layer measurements are used to generate functions that map application models to energy metrics. Any aspect of the application model can be varied, as defined by the *sampling strategy* described later in this section. Varying selected aspects of the application model corresponds to changes in component configuration parameters and scheduling policies, thus making it possible to determine the average power as a function of specific variations of selected component configuration parameters and aspects of the scheduling policy. Due to the potentially large configuration space, it is critical that a model covering all relevant parameter/scheduling variations can be generated from a subset of samples. This is handled by the *approximation method*, also described later in this section.

As a concrete example, Figure 4.3 shows the total average energy usage of the TX2 board executing the `matrix-gpu` component as a function of the size and exponent parameters. Results are discussed in further detail in the context of experimental results, see Section ??.

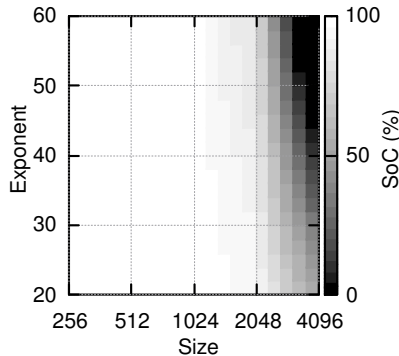


Fig. 4.4. Remaining battery capacity

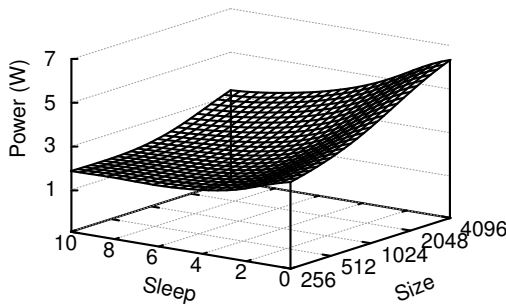


Fig. 4.5. Average power

4.1.6 Hardware platforms and benchmarks

In the following section, we present hardware platforms under study, the two measuring technique to obtain power metrics, and a summary of the profiling tool. Finally, Experimental Methodology outlines our experimental approach before introducing results in the next Section.

We studied four different hardware platforms, ODROID XU3, NVIDIA Jetson TK1, TX2, and Nano that are shown in Figure ??

ODROID XU3 Provides an ARM Cortex-A15 and -A7 CPU, 2 GBytes of LPDDR₃ RAM, a MALI GPU, and storage via microSD. It includes built-in sensors that enable accurate power measurements of the two CPUs, RAM, and GPU.

NVIDIA TK1 Provides an ARM Cortex-A15 CPU, 2 GBytes of DDR_{3L} RAM, 16 GB of non-volatile storage, and an NVIDIA Kepler GPU with 192 CUDA cores. The TK1 does not provide any built-in sensor for power measurement, so an external sensor is used to measure the total power consumed.

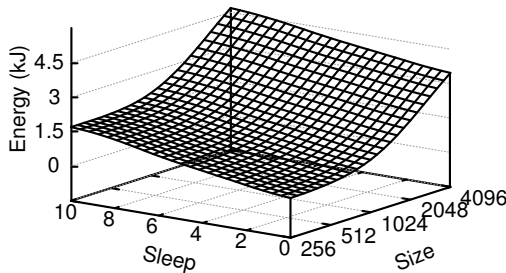


Fig. 4.6. Overall energy

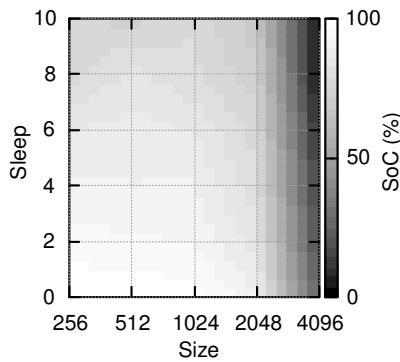


Fig. 4.7. Remaining battery capacity

NVIDIA TX2 Provides an ARM Cortex-A57 CPU, 8 GBytes of LPDDR4 RAM, 32 GB of non-volatile storage, and an NVIDIA Pascal GPU with 256 CUDA cores. The TX2 comes with on-board power measurement functionality that can measure the power of different components, and was used in our model to gather independently the instantaneous power usage of the CPU, GPU, and the whole board.

NVIDIA Nano Provides an ARM Cortex-A57 CPU, 4 GBytes of LPDDR4 RAM, an NVIDIA Maxwell GPU with 128 CUDA cores, and storage via microSD. Similarly to the TX2, the Nano comes with on-board power measurement functionality that is able to measure the power of different components and can be used within our model to gather independently the instantaneous power usage of the CPU, GPU, and the whole board.

Several benchmarks (see Section ??) have been performed on the four hardware platforms under study. (Not all benchmarks components are compatible with every platform, e.g., GPU-based benchmarks are implemented in CUDA which only runs on NVIDIA platforms, limiting the set of experiments that can be performed.)

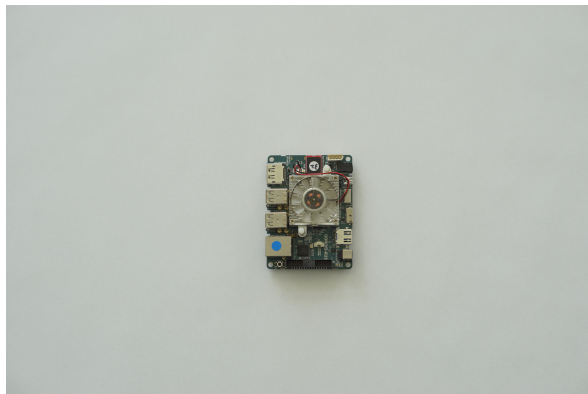


Fig. 4.8. ODROID XU3



Fig. 4.9. NVIDIA Jetson TK1

4.1.7 Power measurements

We use two different power measurements techniques for our experiments: the current shunt and current probe. With the current shunt method, an internal circuit on the embedded board composed of a shunt resistor is used, along with a digital acquisition unit. It is the preferred approach as it can precisely sample the power consumption of specific computing elements as CPU and GPU. Such circuits are present on the ODROID XU3 and NVIDIA TX2 or Nano boards and can be sampled directly by the `powprofiler` tool described in Subection ??.

As an alternative to the current shunt method, we have also implemented the current probe method, where an external circuit measures the power on the connection to the main embedded board (i.e., the carrier board). We adopted the current probe method to measure the overall power consumption of the NVIDIA TK1. This mea-



Fig. 4.10. NVIDIA Jetson TX2



Fig. 4.11. NVIDIA Jetson Nano

surement setup consists of three hardware units, henceforth referred to as nodes. The first node is the board under analysis, the second node a multimeter that performs the sampling of the power consumption at a specific sampling frequency, and the third node is an external computer that collects the data for subsequent processing by `powprofiler`. The whole setup is described in detail in our prior work ([Seewald, Ebeid, et al., 2019](#)). Data and metrics are stored for use with `powprofiler`, essentially allowing an arbitrary power measurement technique for the system under analysis. This means that a layer 2 model can be generated from the data with no distinction of what type of measuring device was used to obtain the layer 1 model.

All experiments reported in this section are performed using the standard performance governor present in each of the systems under observation. In particular, dynamic effects such as DVFS have not been disabled. Our experiments have not revealed

Platform	CPU	GPU	RAM	Memory	Board	Sensors
ODROID	A15, A7	MALI	2 GB	microSD	94x70	✓
TK1	A15	Kepler	2 GB	16 GB	125x95	-
TX2	A57	Pascal	8 GB	32 GB	170x170	✓
Nano	A57	Maxwell	4 GB	microSD	100x80	✓

Table 1. Summary of hardware platforms under analysis.

Component \ Platform	Odroid-XU3	NVIDIA		
		TK1	TX2	Nano
CPU	A15+A7	A15	A57	A57
GPU	MALI	Kepler	Pascal	Maxwell
matrix-cpu	✓	✓	✓	✓
matrix-gpu	-	✓	✓	✓
darknet-cpu	(✓)	(✓)	✓	(✓)
darknet-gpu	-	-	✓	(✓)
nvidia-matrix	-	(✓)	✓	(✓)
nvidia-quicks	-	(✓)	✓	(✓)

Table 2. Benchmark components: platforms and modeling approach. ✓: supported and included in this paper, (✓): supported but not included in this paper, -: not supported.

any effects on performance due to, e.g., ambient temperature or the temperature of the embedded systems increasing.

4.1.8 The powprofiler tool

The `powprofiler` tool implements all the features described in this paper and is designed to be useable for heterogeneous parallel embedded systems. The tool supports all the platforms described in Section ???. It is designed for extensibility and can, in principle, support any Linux-based embedded device that provides power measurement metrics. Concretely, to support a new embedded device, a subclass defining the device-specific features can be derived from a virtual class, and only requires the implementation of a function that returns the current measurements in the form of a weighted vector where every element can represent a different metric. In a first iteration, the tool profiles a set of configurations of a component and builds a layer 1 model as described in Section ???. Once `powprofiler` obtains power profiles and other metrics that are considered useful for the purpose of energy modeling, it builds a predictive model as described in Section ???. The tool relies on `gnuplot` utility to visualize energy evolution if the configuration search space allows it. Automatically generated

output includes CSV files containing measured data as well as the 2D- and 3D-plots shown in this paper.

The tool measures the instantaneous energy consumption of a subset of possible computation parameters within the computation constraint sets and builds an energy model: a linear interpolation, one per computation.

The computations are implemented by software components, e.g., ROS nodes in a ROS-based system (see [Subsection 4.1.10](#)). The user implements these nodes such that they change the computational load according to node-specific ROS parameters—the computation parameters. In a generic software component system, the user maps the computational load to the arguments ([Seewald, Schultz, et al., 2019](#)).

We note that while the path can differ for each stage, the tasks remain the same. However, the user can inhibit or enable a computation varying its computation constraint set.

Let us define the output from `powprofiler` formally.

Definition 4.1.1: Instantaneous computational energy

$g : \mathbb{Z}_{\geq 0} \rightarrow \mathbb{R}_{\geq 0}$ as the instantaneous computational energy consumption value obtained using the `powprofiler` tool.

4.1.9 Energy-aware design of algorithms

4.1.10 ROS integration

4.1.11 Experimental evaluation

The power modeling experiments described in this paper are, unless otherwise mentioned, done using `powprofiler` tool. The tool uses two temporal schemes to profile data. A component can be profiled for a specific amount of time with the first, or until it terminates its computation with the second. The second scheme is used for all the components that end in a specific amount of time, i.e., matrix multiplication. The first for components that run continuously, i.e., an image detection algorithm operating on an image stream. For both, the longer the profiling, the better the accuracy.

Ideally, any component combination can be profiled by specifying possible sets of parameters in the configuration file. Each entry corresponds to a component and defines how its execution is varied as described in application specification described in [Subsection 4.1.4](#). In summary, a layer 1 model is evaluated and stored for every possible combination. The layer 1 model is then integrated with the battery model. Data containing energy consumption, battery drain, and other information as system load, are evaluated into the layer 2 model. This model builds an n -dimensional function and provides energy consumption data for every possible combination. The missing data are integrated using estimation with the approximation technique describe in

Subsection ???. The n -dimensional space is derived by the use of the battery model to map each value with a weight describing the SoC.

As an example of energy modeling, we implemented a combination of three different parameters and generated a surface that shows approximately where the minimum power consumption is expected. Figure 4.3 and Figure 4.7 show how the output of the predictive model includes, but is not limited to, overall energy in Figure 4.3 and Figure 4.6 and average power consumption in Figure 4.2 and Figure 4.5 for all the combinations.

4.2 Battery Model

4.2.1 Batteries for aerial robots

4.2.2 Derivation of differential battery model

The battery model is a mathematical abstraction that models draining energy from a battery used to power the mobile robot. It was derived from the state-space problem representation of the empirical battery model through an equivalent electrical circuit, presented by Hasan et al. [Hasan et al., 2018](#). The battery evolution model can be represented in this way using an ordinary differential equation that is a function of the power drained from the system, and represents the SoC of the battery at a given instant

$$\frac{d}{dt} \text{SoC}(t) = -\frac{i_{\text{int}}(t)}{Q_c}, \quad (4.1)$$

$$i_{\text{int}}(t) = \frac{U_{\text{int}} - \sqrt{U_{\text{int}}^2 - 4 \cdot R_{\text{int}} \cdot U_{\text{sta}} \cdot I_{\text{load}}(t)}}{2 \cdot R_{\text{int}}}, \quad (4.2)$$

where Q_c is the constant nominal capacity, U_{int} is the internal battery voltage, i_{int} is the current load that depends on the power requirements, R_{int} is the internal resistance of the battery, U_{ext} is the external battery voltage, U_{sta} is the stabilized voltage (a fixed value determined by the load of the system), and I_{load} is the current required by the load. The constants are chosen to describe a small drone battery. The external battery voltage U_{ext} can be also expressed as follows:

$$U_{\text{ext}}(t) = U_{\text{int}} - R_{\text{int}} \cdot i_{\text{int}}(t) \quad (4.3)$$

The approach allows modeling the computational system not only in terms of the overall power consumption but also in terms of the actual amount of power drained from the battery. This is especially important with a mobile robot dependent on a limited and time-dependent energy supply, running computationally heavy parallel algorithms. Critically, although this mathematical model is a simple abstraction, it models how a stable power consumption over time can induce less drain from the

battery compared to using the same amount of energy distributed in a number of spikes. The battery model allows this information to be determined for specific usage scenarios and thus provides a useful way to determine what configuration corresponds to the best power usage combination for a mobile use case.

4.3 Energy Model of the Motion

4.3.1 Mechanical energy of the aerial robot

In this subsection, a regression technique to build a mechanical energy model is described. The model is specific for an Opterra drone, but an equivalent technique can be applied to any fixed-wing drone. Key to the technique is the distinction between three phases of the flight: take-off, cruise, and landing. The distinction between these three phases follows from experimental data, as we observed that different flights present similar behavior and almost identical tendencies. This means that each phase has a different altitude and overall time evolution concerning motor torque and power drain. In particular, less variability in energy evolution is observed during the cruise and take-off. This applies when we analyze a single test flight, and when we analyze a set of flights regarding their phases. In the latter, we observed little variability in the cruise phase of different flights, as this is performed mostly by the autopilot with variability often due to wind conditions, while take-off of a fixed-wing drone usually presents a similar set of controls with little variability. Landing is observed to be the phase that presents the largest variability in the collected data, as the procedure requires specific and conditions-dependent maneuvers. Furthermore, glide slope and ground effect, specific to landing site conditions, also affect the controls sequence.

A weighted average time derived from collected data of 28 seconds, 10 minutes, and 1 minute, for respectively take-off, cruise, and landing, is assumed to model a test mission that we use in this paper. The information is used in the regression technique to map time to the current energy consumption. Regression itself consists of a phase-specific third-order Fourier series, as the data often presents a periodic behavior and tends to diverge for higher orders while not mapping precisely to the power evolution in time for lower ones. The following equation represents the power as a function of time t for each of the three phases:

$$f(t) = \sum_{n=0}^3 a_n \cos\left(\frac{nt}{\xi}\right) + b_n \sin\left(\frac{nt}{\xi}\right), \quad (4.4)$$

where a_n, b_n are the Fourier series coefficients, ξ is a characteristic time, and:

$$f(t), t, a_n, b_n, \xi \in \mathbb{R}, \quad (4.5)$$

The Mechanical energy evolution in time can be expressed through a three-dimensional vector \mathbf{f} :

$$\mathbf{f}(t) = \begin{bmatrix} f_1(t) & f_2(t) & f_3(t) \end{bmatrix}^T, \quad (4.6)$$

where $f_1(t), f_2(t), f_3(t)$ are the energy evolutions in time for take-off, cruise, and landing respectively.

The mechanical energy model from Equations (4.4–4.6), can also be expressed in a matrix form:

$$\mathbf{f}(t) = \begin{bmatrix} {}^1a_0 & {}^1b_0 & \dots & {}^1a_3 & {}^1b_3 \\ {}^2a_0 & {}^2b_0 & \dots & {}^2a_3 & {}^2b_3 \\ {}^3a_0 & {}^3b_0 & \dots & {}^3a_3 & {}^3b_3 \end{bmatrix} \begin{bmatrix} \cos \frac{0t}{\xi} \\ \sin \frac{0t}{\xi} \\ \vdots \\ \cos \frac{3t}{\xi} \\ \sin \frac{3t}{\xi} \end{bmatrix}. \quad (4.7)$$

The constants a_n, b_n , and ξ , for the regressions $f_i(t)$ with $i \in 1, 2, 3$ (and thus for $\mathbf{f}(t)$) were found using the Levenberg-Marquardt algorithm implemented in Matlab. The above procedure, however, just accounts for one flight. A further analysis concerns the generation of power trajectories through the technique for each test flight. An interpolating curve is then built using a probabilistic approach, that simply indicates a weight for a given flight k . This can be particularly useful as some flights can be affected by other conditions such as wind, temperature, or battery state at the beginning of the mission, thus affecting the model behavior unexpectedly. Given k flights and a vector of weights \mathbf{w} , the mechanical model can be in this fashion expressed using an equivalent expression to Equation (4.5):

$$\tilde{\mathbf{f}}(t) = \begin{bmatrix} f_{1,1}(t) & f_{1,2}(t) & f_{1,3}(t) \\ \vdots & \vdots & \vdots \\ f_{k,1}(t) & f_{k,2}(t) & f_{k,3}(t) \end{bmatrix}^T \begin{bmatrix} w_1 \\ \vdots \\ w_k \end{bmatrix}, \quad (4.8)$$

where w_i is the associated weight for a specific flight i , that expresses its accuracy according to the set of all the collected flights, and:

$$\begin{aligned} \mathbf{w} &\in \mathbb{R}^k, \\ w_i &\in [0, 1], \\ w_1 + w_2 + \dots + w_k &= 1. \end{aligned} \quad (4.9)$$

Based on a simple reordering, Equations (4.7–4.9) can be also expressed:

$$\tilde{\mathbf{f}}(t) = \begin{bmatrix} 1,1 a_0 & 1,2 a_0 & 1,3 a_0 \\ 1,1 b_0 & 1,2 b_0 & 1,3 b_0 \\ \vdots & \vdots & \vdots \\ 1,1 a_3 & 1,2 a_3 & 1,3 a_3 \\ 1,1 b_3 & 1,2 b_3 & 1,3 b_3 \\ 2,1 a_0 & 2,2 a_0 & 2,3 a_0 \\ 2,1 b_0 & 2,2 b_0 & 2,3 b_0 \\ \vdots & \vdots & \vdots \\ k,1 a_3 & k,2 a_3 & k,3 a_3 \\ k,1 b_3 & k,2 b_3 & k,3 b_3 \end{bmatrix}^T \begin{bmatrix} w_1 \cos \frac{0t}{\xi} \\ w_1 \sin \frac{0t}{\xi} \\ \vdots \\ w_1 \cos \frac{3t}{\xi} \\ w_1 \sin \frac{3t}{\xi} \\ w_2 \cos \frac{0t}{\xi} \\ w_2 \sin \frac{0t}{\xi} \\ \vdots \\ w_k \cos \frac{3t}{\xi} \\ w_k \sin \frac{3t}{\xi} \end{bmatrix}. \quad (4.10)$$

Equation (4.10) can be used to derive all the constants for the three phases of the flight, and thus to describe the power consumption in the function of time for take-off, cruise, and landing. Table 3 outlines the constants that we obtained on the Opterra fixed-wing drone test flights of the agricultural use-case.

Table 3. Constants for the mechanical energy model

	take-off	cruise	landing
a_0	29.97	27.22	27.21
a_1	1.57	0.3737	-0.9512
b_1	-1.963	1.194	1.276
a_2	0.3876	0.6513	0.9357
b_2	-1.552	0.2954	0.965
a_3	-0.2869	0.5039	0.4913
b_3	-0.547	-0.2864	-0.1192
ξ	0.1525	0.1799	0.1296

4.3.2 Fourier series of empirical data

Some collected energy data from the Opterra (in Figure 1.1) adapted for precision agriculture scenario along its power spectrum back the choice of the periodic energy model. A periodic energy evolution of a fixed-wing aerial robot flying a plan and covering the polygon in Figure 1.6 (we describe the fixed-wing aerial robot plan in detail in Section 2.6) is shown in Figure 4.12a. Figure 4.12b shows its frequency spectrum (the data are uniformly sampled). The spectrum is centered at zero frequency, which peaks at $4 \cdot 10^5$ and indicates the shift on the power-axis in Figure 4.12a. The power spectrum shows that the energy evolution from Figure 4.12a needs approximately three

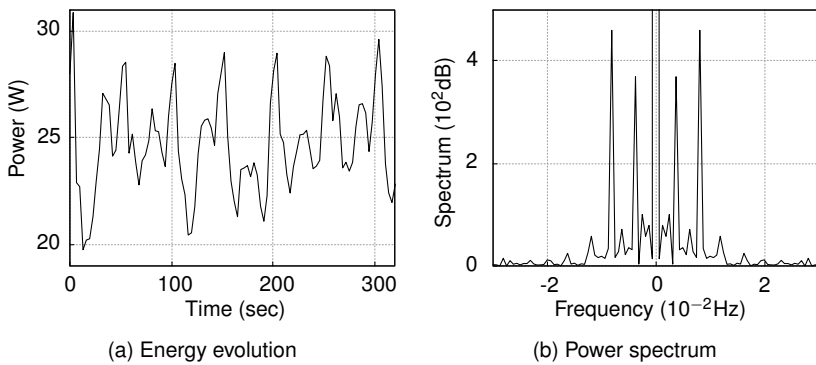


Fig. 4.12. Empirical energy data collected flying a fixed-wing aerial robot's plan and covering the polygon in Figure 1.6. The data shows that the energy signal is periodic over time with the fixed-wing aerial robot reiterating a set of paths.

frequencies to be modeled. To obtain the spectrum in frequency space, we computed the Fourier transform.

4.4 Periodic Energy Model

Let us suppose the aerial robot is operating in an autonomous scenario. Such a robot is often expected to iterate a set of tasks and paths periodically (see Section 1.4). For instance, the aerial robot might be covering a polygon such as the one proposed in Section 2.6. Since the paths and tasks are periodically iterated over time, we expect the energy to evolve similarly. We will ease the assumption of the periodic evolution in practice to periodic with disturbance or aperiodic evolutions in Section 4.4.4.

We motivate the choice of a periodic energy model further with some empirical energy data of the Opterra fixed-wing aerial robot flying the agricultural scenario in Figure 4.12a and Figure 4.12b.

In the remainder of this section, we first derive a differential periodic energy model and provide a formal proof in Section 4.4.1. We enhance the model with the path and computations parameters in Section 4.4.2, to predict the energy consumption of a given configuration of parameters. We explain how we convert the parameters into actual energy consumption in Section 4.4.3, and discuss the model's behavior for aperiodic energy evolutions in Section 4.4.4.

4.4.1 Derivation of the differential periodic model

In the remainder of this section, we refer to the instantaneous energy consumption evolution simply as the energy signal. We model the energy using energy coefficients $\mathbf{q} \in \mathbb{R}^m$ that characterize such energy signal. The coefficients are derived from Fourier

analysis (the size of the energy coefficients vector m is related to the order of the Fourier series in [Section 4.3.2](#)) and estimated using a state estimator in [Chapter 5](#). We prove a relation between the energy signal and the energy coefficients in [Lemma 4.4.1](#).

Let us consider a periodic energy signal of period T , and a Fourier series of an arbitrary order $r \in \mathbb{Z}_{\geq 0}$ for the purpose of modeling of the energy signal

$$h(t) = a_0/T + (2/T) \sum_{j=1}^r (a_j \cos \omega j t + b_j \sin \omega j t), \quad (4.11)$$

where $h : \mathbb{R}_{\geq 0} \rightarrow \mathbb{R}$ maps time to the instantaneous energy consumption, $\omega := 2\pi/T$ is the angular frequency, and $a_j, b_j \in \mathbb{R}$ the Fourier series coefficients $\forall j \in [r]_{>0}$.

The energy signal can be modeled by [Equation \(4.11\)](#) and by the output of a linear model

$$\dot{\mathbf{q}}(t) = A\mathbf{q}(t) + B\mathbf{u}(t), \quad (4.12a)$$

$$y(t) = C\mathbf{q}(t), \quad (4.12b)$$

where $y(t) \in \mathbb{R}$ is the instantaneous energy consumption. We discuss matrices A , C , and B in [Equation \(4.14\)](#), [Equation \(4.16\)](#), and [Equation \(4.48\)](#) respectively.

The state $\mathbf{q}(t)$ contains the energy coefficients

$$\mathbf{q}(t) = \begin{bmatrix} \alpha_0(t) & \alpha_1(t) & \beta_1(t) & \cdots & \alpha_r(t) & \beta_r(t) \end{bmatrix}', \quad (4.13)$$

where $\mathbf{q}(t) \in \mathbb{R}^m$ with $m = 2r + 1$. The state transition matrix

$$A = \begin{bmatrix} 0 & 0^{1 \times 2} & 0^{1 \times 2} & \cdots & 0^{1 \times 2} \\ 0^{2 \times 1} & A_1 & 0^{2 \times 2} & \cdots & 0^{2 \times 2} \\ 0^{2 \times 1} & 0^{2 \times 2} & A_2 & \cdots & 0^{2 \times 2} \\ \vdots & \vdots & \vdots & \ddots & \vdots \\ 0^{2 \times 1} & 0^{2 \times 2} & 0^{2 \times 2} & \cdots & A_r \end{bmatrix}, \quad (4.14)$$

where $A \in \mathbb{R}^{m \times m}$. In matrix A , the top left entry is zero, the diagonal entries are A_1, \dots, A_r , the remaining entries are zeros. Matrix $0^{i \times j}$ is a zero matrix of i rows and j columns. The submatrices A_1, A_2, \dots, A_r are defined

$$A_j := \begin{bmatrix} 0 & \omega j \\ -\omega j & 0 \end{bmatrix}, \quad (4.15)$$

$\forall j \in [r]_{>0}$. The output matrix

$$C = (1/T) \begin{bmatrix} 1 & 1 & 0 & \cdots & 1 & 0 \end{bmatrix}, \quad (4.16)$$

where $C \in \mathbb{R}^m$.

The linear model in [Equation \(4.12\)](#) allows us to include the control in the model of [Equation \(4.11\)](#) as described in [Section 4.4.2](#). In the remainder we formally proof the equivalence and equality of the models in [Equation \(4.11\)](#) and [Equation \(4.12\)](#).

Lemma 4.4.1: Signal, output equality

Suppose control u is a zero vector, matrices A, C are described by [Equations \(4.14–4.16\)](#), and the initial guess q_0 is

$$q_0 = \begin{bmatrix} a_0 & a_1/2 & b_1/2 & \cdots & a_r/2 & b_r/2 \end{bmatrix}'.$$

Then, the signal h in [Equation \(4.11\)](#) is equal to the output y in [Equation \(4.12\)](#).

Proof. The proof justifies the choice of the items of the matrices A, C and of the initial guess q_0 in [Equations \(4.13–4.16\)](#). We write these elements such that the coefficients of the series a_0, \dots, b_r are the same as the coefficients of the state α_0, \dots, β_r .

Let us re-write the Fourier series expression in [Equation \(4.11\)](#) in its complex form with the well-known Euler's formula

$$e^{it} = \cos t + i \sin t, \quad (4.17)$$

where i is the imaginary unit.

With $t = \omega jt$, we find the expression for

$$\cos \omega jt = (e^{i\omega jt} + e^{-i\omega jt})/2, \quad (4.18a)$$

$$\sin \omega jt = (e^{i\omega jt} - e^{-i\omega jt})/(2i), \quad (4.18b)$$

by substitution of $\sin \omega jt$ and $\cos \omega jt$ respectively. This leads ([Kuo, 1967](#))

$$h(t) = a_0/T + (1/T) \sum_{j=1}^r e^{i\omega jt} (a_j - ib_j) + (1/T) \sum_{j=1}^r e^{-i\omega jt} (a_j + ib_j). \quad (4.19)$$

The solution at time t of the model in [Equation \(4.12\)](#) under the assumptions in in the lemma (the control is a zero vector) can be expressed

$$q(t) = e^{At} q_0. \quad (4.20)$$

Both the solution and the system in [Equation \(4.12\)](#) are well-established expressions derived using standard textbooks ([Kuo, 1967; Ogata, 2002](#)).

To solve the matrix exponential e^{At} , we use the eigenvectors matrix decomposition method (Moler and Van Loan, 2003).

The method works on the similarity transformation

$$A = VDV^{-1}. \quad (4.21)$$

The power series definition of e^{At} implies (Moler and Van Loan, 2003)

$$e^{At} = Ve^{Dt}V^{-1}. \quad (4.22)$$

We consider the non-singular matrix V , whose columns are eigenvectors of A

$$V := \begin{bmatrix} v_0 & v_1^0 & v_1^1 & \dots & v_r^0 & v_r^1 \end{bmatrix}. \quad (4.23)$$

We then consider the diagonal matrix of eigenvalues

$$D = \text{diag}(\lambda_0, \lambda_1^0, \lambda_1^1, \dots, \lambda_r^0, \lambda_r^1). \quad (4.24)$$

λ_0 is the eigenvalue associated to the first item of A . λ_j^0, λ_j^1 are the two eigenvalues associated with the block A_j . We can write

$$AV = VD. \quad (4.25)$$

We apply the approach in terms of Equation (4.12) (under the assumptions made in the lemma)

$$\dot{\mathbf{q}}(t) = A\mathbf{q}(t). \quad (4.26)$$

The linear combination of the initial guess and the generic solution

$$F\mathbf{q}(0) = \gamma_0 v_0 + \sum_{k=0}^1 \sum_{j=1}^r \gamma_j v_j^k, \quad (4.27a)$$

$$F\mathbf{q}(t) = \gamma_0 e^{\lambda_0 t} v_0 + \sum_{k=0}^1 \sum_{j=1}^r \gamma_j e^{\lambda_j t} v_j^k, \quad (4.27b)$$

where

$$F = \begin{bmatrix} 1 & \dots & 1 \end{bmatrix}, \quad (4.28)$$

$F \in \mathbb{R}^m$ is a column vector of ones.

Let us consider the expression in Equation (4.27b). It represents the linear combination of all the coefficients of the state at time t . It can also be expressed in the following form

$$\begin{aligned} F\mathbf{q}(t)/T &= \gamma_0 e^{\lambda_0 t} v_0/T + (1/T) \sum_{j=1}^r \gamma_j e^{\lambda_j^0 t} v_j^0 + \\ &\quad (1/T) \sum_{j=1}^r \gamma_j e^{\lambda_j^1 t} v_j^1. \end{aligned} \quad (4.29)$$

We prove that the eigenvalues λ and eigenvectors V are such that [Equation \(4.29\)](#) is equivalent to [Equation \(4.19\)](#).

The matrix A is a block diagonal matrix, so we can express its determinant as the multiplication of the determinants of its blocks

$$\det(A) = \det(0) \det(A_1) \det(A_2) \cdots \det(A_r). \quad (4.30)$$

We now conclude the proof by computing the first determinant and the others separately.

By computing the first determinant, we prove that the first terms in [Equation \(4.19\)](#) and [Equation \(4.29\)](#) match. We find the eigenvalue from $\det(0) = 0$, which is $\lambda_0 = 0$. The corresponding eigenvector can be chosen arbitrarily

$$(0 - \lambda_0)v_0 = \begin{bmatrix} 0 & \cdots & 0 \end{bmatrix}, \quad (4.31)$$

$\forall v_0$, thus we choose

$$v_0 = \begin{bmatrix} 1 & 0 & \cdots & 0 \end{bmatrix}. \quad (4.32)$$

The sizes of the zero vector and of v_0 in [Equations \(4.31–4.32\)](#) are both \mathbb{R}^m .

We find the value y_0 in [Equation \(4.29\)](#) so that the terms are equal

$$y_0 = \begin{bmatrix} a_0 & 0 & \cdots & 0 \end{bmatrix}, \quad (4.33)$$

where $y_0 \in \mathbb{R}^m$.

Then, we prove the other determinants. In this way, we prove that all the terms in the sum of both [Equation \(4.19\)](#) and [Equation \(4.29\)](#) match.

By computing the second determinant, we prove that the first terms in both summaries in [Equation \(4.19\)](#) and [Equation \(4.29\)](#) match. We thus focus on the first block A_1 , and find the eigenvalues from

$$\det(A_1 - \lambda I) = 0. \quad (4.34)$$

The polynomial $\lambda^2 + \omega^2$, gives two complex roots—the two eigenvalues

$$\lambda_1^0 = i\omega, \quad (4.35a)$$

$$\lambda_1^1 = -i\omega. \quad (4.35b)$$

The eigenvector associated with the eigenvalue λ_1^0 is

$$v_1^0 = \begin{bmatrix} 0 & -i & 1 & 0 & \cdots & 0 \end{bmatrix}'. \quad (4.36)$$

The eigenvector associated with the eigenvalue λ_1^1 is

$$v_1^1 = \begin{bmatrix} 0 & i & 1 & 0 & \cdots & 0 \end{bmatrix}'. \quad (4.37)$$

Both eigenvectors are equally sized $v_1^0, v_1^1 \in \mathbb{R}^m$.

Again, we find the values γ_1 in [Equation \(4.29\)](#) such that the equivalences

$$\begin{cases} e^{i\omega t}(a_1 - ib_1) &= \gamma_1 e^{i\omega t} v_1^0 \\ e^{-i\omega t}(a_1 + ib_1) &= \gamma_1 e^{i\omega t} v_1^1 \end{cases}, \quad (4.38)$$

hold. They hold for

$$\gamma_1 = \begin{bmatrix} 0 & b_1 & a_1 & 0 & \cdots & 0 \end{bmatrix}. \quad (4.39)$$

The proof for the remaining $r - 1$ blocks is equivalent.

The initial guess \mathbf{q}_0 is build such that the sum of the coefficients is the same in both the signals. In the output matrix, the frequency $1/T$ accounts for the period in [Equation \(4.19\)](#), [Equation \(4.29\)](#), and [Equation \(4.11\)](#). At time instant zero, the coefficients b_j are not present and the coefficients a_j are doubled for each $j = 1, 2, \dots, r$ (thus we multiply by a half the corresponding coefficients in \mathbf{q}_0). To match the outputs $h(t) = y(t)$, or equivalently

$$F\mathbf{q}(t)/T = C\mathbf{q}(t), \quad (4.40)$$

we define

$$C := (1/T) \begin{bmatrix} 1 & 1 & 0 & \cdots & 1 & 0 \end{bmatrix}. \quad (4.41)$$

We thus conclude that the signal and the output are equal and that the lemma holds. ■

We note for practical reasons that the signal would still be periodic with another linear combination of coefficients. For instance

$$C := d \begin{bmatrix} 1 & 1 & 0 & \cdots & 1 & 0 \end{bmatrix}, \quad (4.42)$$

equivalent to

$$C := d \begin{bmatrix} 1 & 0 & 1 & \cdots & 0 & 1 \end{bmatrix}, \quad (4.43)$$

or

$$C := d \begin{bmatrix} 1 & \cdots & 1 \end{bmatrix}, \quad (4.44)$$

for a constant value $d \in \mathbb{R}$.

4.4.2 Nominal control

Let us suppose that at time instant t the plan (see [Definition 2.4.1](#)) reached the i th stage Γ_i and the control contains the configuration of path and computations parameters

$$c_i(t) = \begin{bmatrix} c_i^\rho(t) & c_i^\sigma(t) \end{bmatrix}', \quad (4.45)$$

where $c_i(t) \in \mathbb{R}^n$ with $n = \rho + \sigma$ differs from the nominal control $\mathbf{u}(t)$ in Equation (4.12). We include the control in the nominal control exploiting the following observation.

Observation

We observe that:

- A change in path parameters affects the energy indirectly. It alters the time when the aerial robot reaches the final point \mathbf{p}_{Γ_f} , and enters the accepting stage Γ_f .
- A change in computation parameters affects the energy directly. It alters the instantaneous energy consumption as more computations require more power (and vice versa).

The second bullet point in the observation is easily verified. The `powprofiler` profiling tool models the energy consumption of the heterogeneous computing hardware the mobile robot is caring. A variation in the computation parameter affects the schedule and hence the instantaneous energy consumption of the mobile robot.

The first bullet point in the observation can be verified by inspection of the example in Section 2.6. It is clear that if we increase the parameter $c_{4,1}$, which is relative to the radius of the circle, the flying time decreases. This is further shown in Figure 4.13 and Figure 4.14. Figure 4.13 illustrates the trajectory of the aerial robot (composed of all the paths $\varphi_1, \varphi_2, \dots, \varphi_l$) flying at the highest configuration of the path parameter $c_{4,1} = \bar{c}_{4,1}$. Figure 4.14 then illustrate the trajectory flying at the lowest configuration $c_{i,1} = \underline{c}_{4,1}$. The flying time differs significantly, along with the quality of the coverage of the polygon (the agricultural field in Figure 1.6).

In Figure 4.14, the parameter $c_{4,1}$ that alters the radius and center of the upper circle (defined originally in Section 2.6) is replanned as, e.g., averse atmospheric conditions do not allow to terminate the original plan in Figure 4.13.

We use the observation later in Section 7.6.2 to check that the time to completely discharge the battery is greater than the flight time and replan the path parameters accordingly. We replan the computation parameters to maximize the instantaneous energy consumption against the maximum battery discharge rate.

The nominal control is

$$\mathbf{u}(t) := \hat{\mathbf{u}}(t) - \hat{\mathbf{u}}(t - \Delta t), \quad (4.46)$$

where $\hat{\mathbf{u}}(t)$ is defined as the energy estimate of a given control sequence at time instant t , $\hat{\mathbf{u}}(t - \Delta t)$ at the previous time instant $t - \Delta t$

$$\hat{\mathbf{u}}(t) := \text{diag}(\nu_i)c_i(t) + \tau_i, \quad (4.47)$$

where $\text{diag}(\nu_i)$ is a diagonal matrix with the parameters $\nu_{i,j} \in \nu_i, \forall j \in [n]_{>0}$.

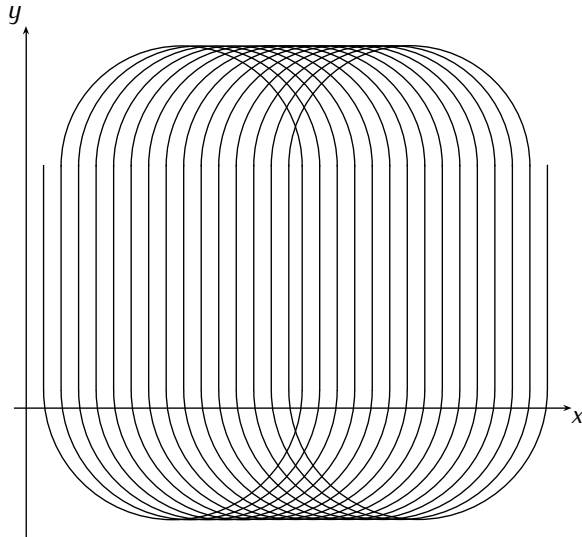


Fig. 4.13. The trajectory of the aerial robot flying paths $\varphi_1, \varphi_2, \dots, \varphi_l$ from Section 2.6 with the highest configuration of the path parameter $c_{4,1} = \bar{c}_{4,1}$. This configuration of path parameter has the longest time but the shortest distance between the lines and thus the highest quality of the coverage in [Figure 1.6](#).

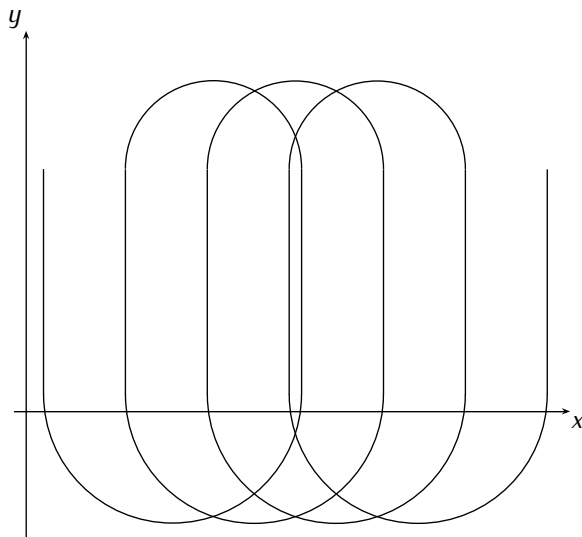


Fig. 4.14. The trajectory of the aerial robot similarly as in [Figure 4.13](#) but with the lowest configuration of the path parameter $c_{4,1} = \underline{c}_{4,1}$. This configuration has the longest distance between the lines and thus the lowest quality of the coverage in [Figure 1.6](#).

The input matrix is then

$$B = \begin{bmatrix} 0^{1 \times \rho} & 1 & \dots & 1 \\ 0^{1 \times \rho} & 0 & \dots & 0 \\ \vdots & \vdots & \ddots & \vdots \\ 0^{1 \times \rho} & 0 & \dots & 0 \end{bmatrix}, \quad (4.48)$$

where $B \in \mathbb{R}^{m \times n}$ contains zeros except the first row where the first ρ columns are still zeros and the remaining σ are ones.

$\hat{\mathbf{u}}(t)$ is a stage-dependent scale transformation with

$$\nu_i = \begin{bmatrix} v_i^\rho & v_i^\sigma \end{bmatrix}', \quad (4.49a)$$

$$\tau_i = \begin{bmatrix} \tau_i^\rho & \tau_i^\sigma \end{bmatrix}', \quad (4.49b)$$

scaling factors. They quantify the contribution to the plan of a given parameter in terms of time for the first ρ parameters, and instantaneous energy consumption for the remaining σ (we use the same notation for the path and computation scaling factors as for the parameters).

The nominal control $\mathbf{u}(t)$ is then the difference of these contributions of two consecutive controls $\mathbf{u}(t - \Delta t)$, $\mathbf{u}(t)$ applied to the system.

$B\mathbf{u}(t)$ merely includes the difference in the instantaneous energy consumption into the model in Equation (4.12).

4.4.3 Parameters scale transformation

To transform the control $c_i(t)$ at i th stage and time instant t we use different approaches for the path and computation scaling factors.

The scaling factors for the path parameters from Equation (4.49) are derived empirically. For example, we can obtain the scaling factor $v_{4,1}$ relative to the alteration of the upper circle $c_{4,1}$ from Section 2.6 by measuring the time needed to compute the path with the lowest configuration $\underline{c}_{4,1}$, \underline{t} in Figure 4.14, and the highest \bar{t} in Figure 4.13.

The variation of the control hence results in an approximate measure of the plans' time variation with factors

$$v_{i,j} = ((\bar{t} - \underline{t}) / (\bar{c}_{i,j} - \underline{c}_{i,j})) / \rho, \quad (4.50a)$$

$$\tau_{i,j} = (\underline{c}_{i,j}(\bar{t} - \underline{t}) / (\bar{c}_{i,j} - \underline{c}_{i,j})) + \underline{t} / \rho, \quad (4.50b)$$

$\forall j \in [\rho]^+$. Moreover, let the factors be zero when the parameters set $c_i^\rho = \{\emptyset\}$.

The scaling factors for the computations parameters from Equation (4.49) are derived using `powprofiler`, the open-source modeling tool from Section 4.1.8. We estimate the energy cost of a given schedule (a given computations configuration) with

the function g from [Definition 4.1.1](#). For instance, if the computation is an object detector, a computation parameter $c_{1,2}$ might correspond to frames-per-second (fps) rate. The tool then measures power according to the detection frequency.

The scaling factors add the computational energy component to the model in [Equation \(4.12\)](#). They are derived similarly to [Equation \(4.50\)](#)

$$\nu_{i,j} = (g(\bar{c}_{i,j}) - g(c_{i,j})) / (\bar{c}_{i,j} - c_{i,j}), \quad (4.51a)$$

$$\tau_{i,j} = c_{i,j} (g(c_{i,j}) - g(\bar{c}_{i,j})) / (\bar{c}_{i,j} - c_{i,j}) + g(c_{i,j}), \quad (4.51b)$$

$\forall j \in [\rho + 1, n]$. Moreover, let the factors be zero when the parameters set $c_i^\sigma = \{\emptyset\}$.

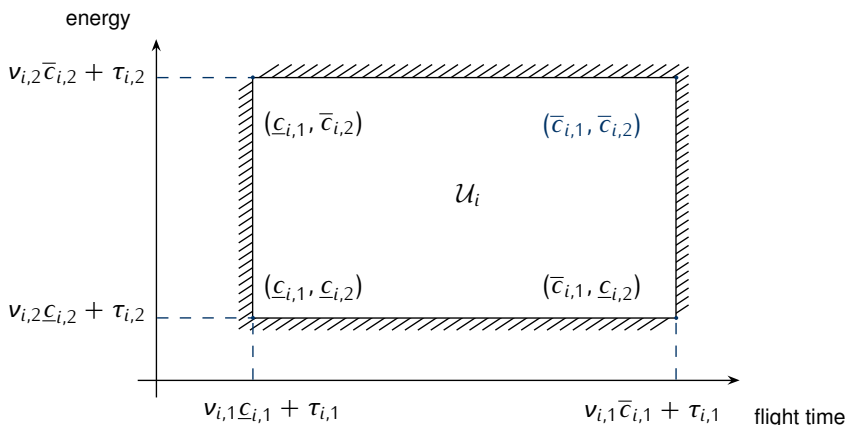


[Fig. 4.15](#). The concept of a path and computation parameter scale transformation. Without any battery constraints, the dynamic energy planning selects the highest configuration which respects the control constraint (inner rectangle) from [Equation \(2.5\)](#).

The concept of a path and a computation parameter scale transformation is illustrated in [Figure 4.15](#). The energy domain is bounded by the output of `powprofiler`, while the flight time domain by the empirical data. The dynamic energy planning selects the highest possible configuration under the constraints. Currently, the highest configuration of parameters corresponds to the highest configuration of parameters $(\bar{c}_{i,1}, \bar{c}_{i,2})$ (blue point in the figure). We will show in [Section 7.6.1](#) the optimal control derivation over a time horizon N under given battery constraints.

4.4.4 Aperiodic energy evolution

4.5 Contribution

4.6 Results

This Section shows and assesses experimental results for the benchmarks, and validates the presented approach.

We now describe the experimental results of the benchmarks previously introduced. A summary of these results is outlined in [Table 4](#).

Component	ODROID XU3	NVIDIA		
		TK1	TX2	Nano
matrix-cpu	5284 J	4067 J	2413 J	2736 J
matrix-gpu	-	81 J	45 J	39 J
darknet-cpu	(-)	(-)	2400 J	(-)
darknet-gpu	-	-	5255 J	(-)
nvidia-matrix	-	(-)	4054 J	(-)
nvidia-quicks	-	(-)	1995 J	(-)

[Table 4](#). The overall energy consumption for each benchmark. Unsupported platforms are indicated by ‘-’ and ‘(-)’ indicates supported but not included in this paper.

Matrix Exponentiation

Execution of GPU matrix exponentiation, while varying size and exponent parameters, was previously shown in [Figure 4.3](#). The figure shows the average power as well as overall energy consumption along with the battery depletion as a function of size and exponent parameters. Average power consumption is reported independently of the running time of the component and thus does not reflect the total power consumption. For small problem sizes, the computation terminates before reaching the maximal power level. This effect is visible in [Figure ??](#) (also previously shown), where power consumption is low at the beginning and then reaches the maximum, for which reason the average power consumption is low for small problem sizes. Battery depletion is reported in terms of the total amount of energy consumed by the computation for the duration of the execution. The effect of introducing “scheduling” in the form of sleep of various durations in between iterations of the matrix computations can be seen in [Figure 4.7](#). Here, the duration of the sleep affects the total power consumption: the higher the sleep value in between the iterations, the greater the battery depletion.

CPU vs GPU comparison shows, expectedly, that `matrix-gpu` is very performant compared to `matrix-cpu`. While the `matrix-cpu` requires 2 413 J, `matrix-gpu` requires only 45 J for the same operation on the TX2 board. Therefore, running the benchmark on GPU results in 16% more SoC against the same trial on CPU. Such a high speed-up is observed due to the highly parallelizable nature of the matrix exponentiation and hence cannot be used as a general rule. From our experiments, we

Fig. 4.16. Layer 2 model of `darknet-gpu` component running under four configurations, respectively 5.8, 10, 25 and 32 frames-per-second. The figure shows the per-minute energy consumption in terms of CPU, GPU, and overall. On the right side, energy consumption for any possible frame per second rate is shown along with SoC (the y2-axis, the y-axis is shared with the left side).

additionally observe the power-related effect of running components sequentially versus in parallel on different computational units. Although the CPU and GPU are different computational units, the energy consumed by running components independently (i.e., sequentially in some order) on CPU and GPU is 20% larger compared to running them in parallel, even when subtracting the base power consumed by the board. Thus energy can be conserved by running computations in parallel on the CPU and GPU, compared to scheduling them sequentially.

Darknet

We modified the `darknet` component to simulate different scheduling options and evaluated the outcome on a video stream: `darknet` now accepts an argument that indicates the amount of sleep between two invocations of the image recognition algorithm. In this way, we were able to simulate different frames-per-second options and assess the power evolution using the model.

Our experimental data depicted in Figure 4.16 shows that an increment in frames-per-second corresponds to an increased power consumption along with a higher battery depletion. The resulting model can be used to define an appropriate trade-off that represents an acceptable rate of QoS, by i.e., correlating the FPS rate to the battery depletion and hence highlighting the dynamic behavior of a mobile scenario. Moreover, we observe that `darknet-cpu` consumes less energy per minute compared to the `darknet-gpu` component, but is considerably slower: while running `darknet-cpu` for one minute on TX2 board requires 2 400 J, `darknet-gpu` requires 5 255 J. When considering the energy cost per frame the computation is however considerably more efficient on GPU, where it requires just 1.3 J per frame, against the 175 J on GPU.

NVIDIA

The `nvidia-matrix` benchmark differs from `matrix-gpu`, even if both perform matrix multiplication on GPU, since `nvidia-matrix` includes a significant CPU computation after GPU matrix multiplication to check whether the two match. The `matrix-gpu` benchmark was similarly tested during development, but does not perform this test at runtime. We observe that the `nvidia-matrix` benchmark has a similar energy behavior to `matrix-gpu`, with the problem size affecting the overall energy and henceforth battery depletion. Average power consumption on GPU is however

higher for `matrix-gpu` while it is approximately the same on CPU for both benchmarks (presumably none of the two benchmarks focus on energy efficiency on CPU). For the quicksort benchmark, as expected energy consumption increases with the problem size, as more operations are performed. Nevertheless quicksort differs from matrix multiplication: there is more noise due to a higher dependence on the random data that is being sorted.

4.6.1 Validation

We validate our approach by: a) demonstrating that `powprofiler` can be used on a number of heterogeneous platforms, b) comparing model generated with internal metrics to external physical measurements on the TX2, and c) comparing the model to a fine-grained one.

A cross-platform comparison shows energy-related behavior of running the same benchmark on different boards. We observed, for instance, that the most energy-efficient board for `matrix-cpu` benchmark is TX2, which consumes 2 413 J to perform the operation, followed by Nano with 2 736 J, TK1 with 4 067 J, and ODROID with 5 284 J.

A measurement analysis is used to compare internal against external power metrics on the TX2 board. We observe that both externally and internally measured power models are close one to each other, with an error of less than 3% measured over one minute. The externally measured power exceeds the internally measured power — this is natural as the externally measured power also includes the carrier board, which requires additional energy to operate. Moreover, the measurements performed using `powprofiler` include the power consumed by `powprofiler` itself, while the multimeter setup excludes `powprofiler`'s energy from the evaluation. We therefore assume that the tool has a marginal effect on power consumption and that the model is showing realistic behavior.

In a last validation step, we compared our approach to fine-grained energy model of Nunez et al. ([Nunez-Yanez and Lore, 2013](#)) and Nikov et al. ([Nikov et al., 2015](#)) for the ODROID-XU3 embedded board. To relate the two approaches for energy-modeling, we used the `matrix-cpu` benchmark component as follows. First, we evaluated the matrix exponentiation benchmark by raising a 512 by 512 matrix to the 30th power (512^{30}) to train the fine-grained model. We obtained a value of expected energy per operation that we compared to the measured one and measured a relative error of 3.42%. Second, we applied an equivalent approach to our model. We sampled some configurations that were distant from the expected one, concretely we ran configurations 512^x with $x \in \{5, 15, 25, 35, \dots\}$, and we used the approximation method described in [Section ??](#) to evaluate the energy of the configuration 512^{30} . This value was then compared to the measured one and we obtained a relative error of 2.25%. We

can conclude that both models produce similar results on this benchmark, and have a similar relative error even if they adopt a different approach towards energy-modeling.

4.6.2 Assessment

We performed a number of experiments on different boards. Most of the data in this paper were obtained from NVIDIA TX2 due to the similarity with TK1 and Nano and the easy accessibility of the internal power measurement units. These data allowed us to validate our model, and to show that different scheduling options can correspond to different energy models. The model can describe energy consumption and instantaneous power, together with the battery depletion.

Coarse-grained whole-system energy modeling can take into account some behaviors that cannot otherwise easily be observed. As an example, consider the effect of simple scheduling previously shown in [Figure 4.7](#). Here, we expected that introducing a higher sleep period between executions would result in an energy cost. We used the model to investigate this assumption, and we found that it is not always happening. For instance, a period of 2.5s between two consecutive schedules of 512^{12} matrix exponentiation iterated for 12 times is more energy-efficient than executing the whole 512^{144} operation. The model can relate these observations, provide information about the battery depletion, and predict the total time the system can operate on a given energy source. It can also highlight battery-specific behaviors since different scheduling options drain battery differently. In particular, Using the `powprofiler` tool on the NVIDIA TX2, we experimentally observe that:

- Running a set of components separately, and simply adding their energy consumption (while excluding base energy), leads to a different model versus running them in parallel ([Section 4.6](#)). This behavior was observed for matrix exponentiation components running on separate computational units (CPU, GPU).
- Scheduling of computations directly impacts the battery drain: processing a computation in its entirety with a steady power load drains the battery less than scheduling that same computation into smaller steps with resulting spikes in the power load ([Section 4.6.2](#)). This behavior was observed for a matrix exponentiation component running on CPU.

4.7 Summary

Chapter 5

State Estimation

5.1 A Brief History of State Estimation

5.2 A Necessary Background on Probability Theory

5.3 The Curve Fitting Problem

5.3.1 Least square fitting

5.3.2 Levenberg-Marquardt algorithm

5.4 Periodic Model Estimation

5.4.1 Period estimation

5.4.2 Minimization of the estimate error

5.4.3 Period and horizon in continuous estimation

5.5 Filtering

5.5.1 Discrete time Kalman filter

As the environment uncertainty and measurement error evolve in a normal distribution, we use a Kalman filter (Simon, 2006; Stengel, 1994) for the purpose of state estimation.

The prediction is done using

$$\hat{\mathbf{q}}_{k+1}^- = A\hat{\mathbf{q}}_k + B\mathbf{u}_k, \quad (5.1a)$$

$$P_{k+1}^- = AP_k A' + Q, \quad (5.1b)$$

where $\hat{\mathbf{q}}_k^-, \hat{\mathbf{q}}_k \in \mathbb{R}^j$ depicts the estimate of the state before and after measurement (or simply estimate), and $P_k, P_k^- \in \mathbb{R}^{j \times j}$ the error covariance matrix (i.e., the variance of the estimate).

The estimation of the state and the update of the predicted output is done using

$$K_k = (CP_{k+1}^- C' + R)^{-1}(P_{k+1}^- C'), \quad (5.2a)$$

$$\hat{\mathbf{q}}_{k+1} = \hat{\mathbf{q}}_{k+1}^- + K_k(y_k^s + y_k^c - C\hat{\mathbf{q}}_{k+1}^-), \quad (5.2b)$$

$$P_{k+1} = (I - K_k C)P_{k+1}^-, \quad (5.2c)$$

$$\hat{y}_k = C\hat{\mathbf{q}}_{k+1}, \quad (5.2d)$$

where $K_k \in \mathbb{R}^j$ is the gain of the Kalman filter, and I the identity matrix. y_k^s, y_k^c are the instantaneous energy readings: $y_k^s \in \mathbb{R}_{\geq 0}$ the robot sensor, i.e., the energy due to the trajectory, and y_k^c the energy of a given software configuration described in The noise covariance matrices $Q \in \mathbb{R}^{j \times j}, R \in \mathbb{R}$ indicates the uncertainty and measurement error covariance respectively, and $\hat{y}_k \in \mathbb{R}_{\geq 0}$ is the estimated energy.

Equations (5.1–5.2) converge to the predicted energy evolution as follows. An initial guess of the values $\hat{\mathbf{q}}_0, P_0$ is derived empirically from collected data. It is worth considering that an appropriate guess of these parameters allows the algorithm to converge to the desired energy evolution in a shorter amount of time. The tuning parameters Q, R are also derived from the collected data, and may differ due to i.e., different sensors used to measure the instantaneous energy consumption, or different atmospheric conditions accounting for the process noise.

At time $k = 0$, the initial estimate before measurement of the state and of the error covariance matrix is updated in Equations (5.1a–5.1b) respectively. The value of $\hat{\mathbf{q}}_1^-$ is then used in Equation (5.2b) to estimate the current state along with the data from the sensor y_0 (e.g., the energy sensor of the flight controller of the fixed-wing craft), where the sensor noise covariance matrix R accounts for the amount of uncertainty in the measurement. The estimated output \hat{y}_0 is then obtained from Equation (5.2d). The algorithm is iterative. At time $k = 1$ the values $\hat{\mathbf{q}}_1, P_1$ computed at previous step are used to estimate the values $\hat{\mathbf{q}}_2, P_2$, and y_1 .

5.5.2 Continuous time Kalman filter

5.5.3 Nonlinear filtering

5.6 Results

5.7 Summary

Chapter 6

Guidance

6.1 Vector Fields for Guidance

The use of vector fields for guidance is widely discussed in the literature (De Marina et al., 2017; Gonçalves et al., 2010; Kapitanyuk et al., 2017; Lindemann and LaValle, 2005; Panagou, 2014; Zhou and Schwager, 2014).

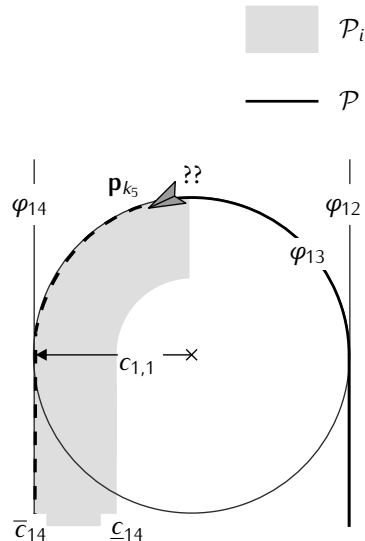


Fig. 6.1. A path parameter in the flight of an aerial robot can be used to alter the overall energy consumption

The set

$$\mathcal{P}_i := \{\mathbf{p}(t) \mid \varphi_i(\mathbf{p}(t), c_i^\rho), c_i^\rho \in \mathcal{U}_i\}, \quad (6.1)$$

delimits the area where the i th path φ_i is free to evolve using the path parameters c_i^ρ (the gray area in Figure 6.1). φ_i is a function of the two coordinates and the path parameters, and is equal to zero when a point $\mathbf{p}(t)$ is on the path. Physically, this means the aerial robot is flying exactly over the nominal trajectory.

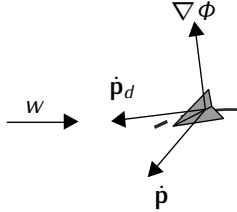


Fig. 6.2. Effects of the external interference (wind) on the flight.

We derive the new position \mathbf{p}_{k+1} computing the vector field

$$\nabla \varphi_i := \begin{bmatrix} \partial \varphi_i / \partial x \\ \partial \varphi_i / \partial y \end{bmatrix}, \quad (6.2)$$

and the direction to follow in the form of velocity vector De Marina et al., 2017

$$\dot{\mathbf{p}}_d(\mathbf{p}_k) := E \nabla \varphi_i - k_e \varphi_i \nabla \varphi_i, \quad (6.3)$$

where E specifies the rotation (it influence the tracking direction). For instance

$$E = \begin{bmatrix} 0 & 1 \\ -1 & 0 \end{bmatrix}, \quad (6.4)$$

is the counter clockwise direction, $-E$ the clockwise direction.

$k_e \in \mathbb{R}_{\geq 0}$ is the gain to adjusts the speed of convergence. The direction the velocity vector $\dot{\mathbf{p}}_d$ is pointing at is generally different from the course heading $\dot{\mathbf{p}}$ due to the atmospheric interferences (wind $w \in \mathbb{R}$ in the top of Figure 6.1).

6.2 Derivation of the Guidance Action

6.2.1 Motion simulations

6.2.2 Energy simulations

6.3 Alteration of the Path

6.4 Results

6.5 Summary

Chapter 7

Optimal Control Generation

THIS chapter provides essential theoretical background on optimal control theory necessary to derive an optimal configuration of the path and computations of the mobile robot. It solves the problem posed in [Section 2](#) and illustrate an algorithm that generates the optimal configuration dynamically. The algorithm relies on a modern optimal control technique known as model predictive control (MPC), where the optimal control trajectory is evaluated on a receding horizon for each optimization step ([Rawlings et al., 2017](#)).

Optimal control deals with finding optimal ways to control a dynamic system ([Sethi, 2019](#)). It determines the control signal—the evolution in time of the decision variables—such that the model satisfies the dynamics and simultaneously optimizes a performance index ([Kirk, 2004](#)).

Many optimization problems originating in fields such as robotics, economics, and aeronautics can be formulated as optimal control problems (OCPs) ([Von Stryk and Bulirsch, 1992](#)). Optimization is often called mathematical programming ([Nocedal and Wright, 2006](#)) a term that means finding ways to solve the optimization problem. One can often find programming in this context in terms such as linear program (LP), quadratic program (QP), and nonlinear program (NLP). NLPs is the class of optimization problems that we use to derive the optimal configuration. OCPs can be seen as optimization problems with the added difficulty of continuous dynamics. The latter is to be integrated over the optimization horizon using numerical simulation. In the algorithm, we formulate the dynamic planning problem as an OCP that we solve with a numerical method: we transform the OCP in an NLP using numerical simulation and solve the NLP using numerical optimization, as proposed in ([Rawlings et al., 2017](#)). The process is illustrated in [Fig. 7.1](#).

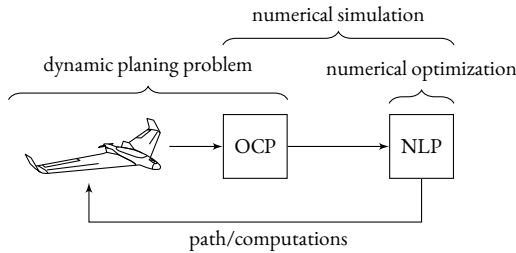


Fig. 7.1. Summary of the optimal control approach. The problem is formulated as an OCP, into finite-dimensional discrete NLP using numerical simulation. NLP is solved using numerical optimization and the optimal configuration for a given time horizon is returned to the aerial robot. The following horizon is evaluated again in a technique known as MPC.

A typical performance measure for an OCP is built such that the system: reaches a target set \mathcal{Q}_f in minor time, reaches a given final state \mathbf{q}_f with minimum deviation, maintains the state evolution as close as possible to a given desired evolution, or reaches the target set with the minimum control expenditure effort (Kirk, 2004). In energy planning, it is desired to focus on the latter performance measure.

The outline of the chapter is as follows. After a brief history of optimal control, we introduce formally the OCP subject to continuous dynamics. We then illustrate numerical simulation approaches to convert the infinite-dimensional continuous dynamics into finite-dimensional discrete dynamics. We formulate later in the chapter the dynamic planning problem for the optimal configuration of the path and computations with proper constraints. Finally, we illustrate MPC to solve OCP on a receding horizon. We propose an algorithm to solve such OCP using a numerical method on the horizon along with the analysis of its practical feasibility.

The chapter builds on the rest of the work as follows. In the OCP formulation, we use the estimated state from Chapter 5 of a perfect model in Chapter 4 to solve the planning problem in Section 2 and guide the aerial robot with the obtained optimal configuration from this chapter with the technique in Chapter 6.

7.1 A Brief History of Optimal Control

Optimal control originates from the calculus of variations (Sethi, 2019), based on the work of Euler and Lagrange. Calculus of variations solves the problem of determining the arguments of an integral, such that its value is maximum (or minimum). The equivalent problem in calculus is to determine the argument of a function where the function is maximum (or minimum). The work by Euler and Lagrange was later extended by Legendre, Hamilton, and Weierstrass (Paulen and Fikar, 2016). It has gained a renewed interest in the mid-twentieth century, as modern calculators offered prac-

tical ways of solving some OCPs for nonlinear and time-varying systems that were earlier impracticable (Bryson and Ho, 1975).

The conversion of the calculus of variation problems in OCPs requires the addition of the control variable to the dynamics (Sethi, 2019).

There are numerous methods to analytically and numerically solve these continuous time OCPs, although analytical solution is often impracticable except for very limited state dimensions (Rawlings et al., 2017). In the early day of optimal control, some analytical solutions were proposed with dynamic programming (Bellman, 1957), and with maximum (or minimum) principle (Pontryagin et al., 1962).

In computer science dynamic programming is fundamental to compute optimal solutions, yet it's original form was developed to solve optimal control problems (LaValle, 2006). Dynamic programming in optimal control theory is based on a partial differential equation of the performance index named Hamilton-Jacobi-Bellman (HJB) equation, which is solved either analytically for small dimensional state space problems, or numerically (Rawlings et al., 2017). Dynamic programming can be shown to be equivalent to the principle (Paulen and Fikar, 2016). The principle is related to HJB equation in that it provides optimality conditions an optimal trajectory must satisfy (LaValle, 2006). HJB offer sufficient conditions for optimality while the principle necessary; yet it is useful to find suitable candidates for optimality (LaValle, 2006).

All the numerical approaches discretize infinite-dimensional problems at a certain point (Rawlings et al., 2017).

A first class of these approaches solves the optimality conditions in continuous time using first-order necessary conditions of optimality from the principle (Böhme and Frank, 2017). This is done by algebraic manipulation using an expression that is similar to the HJB equation, and results in a boundary-value problem (BVP) (Rawlings et al., 2017). The class is commonly referred to as the indirect methods. The BVP is solved by discretization at the very end (Rawlings et al., 2017) and/or gradient-based resolution (Paulen and Fikar, 2016).

On the contrary, modern optimal control often first discretize all the control and state variables in the OCP to a finite dimensional optimization problem (usually NLP), which is then solved with numerical optimization (using gradient-based techniques). This other class of numerical approaches is referred to as direct methods. Some direct methods are single and multiple shooting and collocation methods. We employ direct methods in this chapter.

Modern OCPs are often solved on a finite and receding horizon using an approximation of the true dynamics using MPC techniques. It is a more systematic technique which allow to control a model by re-optimizing the OCP repeatedly (Paulen and Fikar, 2016; Poe and Mokhatab, 2017). It takes into account external interferences by re-estimating the model's state (with techniques that we introduced in Chapter 5).

MPC is extensively treated in modern optimal control literature (Camacho and Alba, 2007; Kwon and Han, 2005; Rawlings et al., 2017; Rossiter, 2004; L. Wang, 2009).

7.2 Optimization Problems with Dynamics

7.2.1 Continuous systems: unconstrained case

Given a state variable \mathbf{q} composed of m states and a control variable \mathbf{u} composed of n controls, the state variable dynamics at a given time instant t can be described by a differential model

$$\dot{\mathbf{q}}(t) = f(\mathbf{q}(t), \mathbf{u}(t), t), \quad \mathbf{q}(t_0) = \mathbf{q}_0 \text{ given, } \forall t \in [t_0, T], \quad (7.1)$$

where $t_0 \in \mathbb{R}_{\geq 0}$ is a given initial time instant, and $\mathbf{q}_0 \in \mathbb{R}^m$ a given initial state guess. The latest can be derived empirically from a previous execution or using some initial sensor data. $f : \mathbb{R}^m \times \mathbb{R}^n \times \mathbb{R}_{\geq 0} \rightarrow \mathbb{R}^m$ maps the current state, control and time to the next state. The notations for $\dot{\mathbf{q}}(t) := d\mathbf{q}(t)/dt$, \mathbf{q} , and \mathbf{u} are the same from Chapter 4. The function f is assumed to be continuously differentiable. Physically, Equation (7.1) specifies the instantaneous change in state variable of a perfect model with no disturbances.

If the control trajectory $\mathbf{u}(t_0), \mathbf{u}(t_1), \dots, \mathbf{u}(T - \Delta t)$ is known for a given time horizon $t_0 \leq t \leq T$, the model in Equation (7.1) can be derived to obtain the state trajectory $\mathbf{q}(t_0), \mathbf{q}(t_1), \dots, \mathbf{q}(T)$, where Δt is the instantaneous change in time. The last state at the final time instant T is derived from the last control at the time instant $T - \Delta t$. The state trajectory has indeed one item more than the control trajectory.

Optimal control finds a control trajectory which maximizes (or minimizes) a performance index

$$L = l_f(\mathbf{q}(T), T) + \int_{t_0}^T l(\mathbf{q}(t), \mathbf{u}(t), t) dt, \quad (7.2)$$

where l, l_f are given instantaneous and final cost functions. The instantaneous cost function maps state, controls, and time to a value that quantifies the cost of a given instant $l : \mathbb{R}^m \times \mathbb{R}^n \times \mathbb{R}_{\geq 0} \rightarrow \mathbb{R}$. The final cost function maps the state and time to a value which quantifies the cost of the final instant $l_f : \mathbb{R}^m \times \mathbb{R}_{\geq 0} \rightarrow \mathbb{R}$. The performance index $L \in \mathbb{R}$ is then the sum of all the contribution on the time horizon.

Performance index found in (Bryson and Ho, 1975) is also found in literature as cost function in (Simon, 2006; Stengel, 1994), objective function in (S. S. Rao, 2019; Rawlings et al., 2017; Sethi, 2019), or performance measure (Kirk, 2004).

The control variable is usually constrained

$$\mathbf{u}(t) \in \mathcal{U}(t), \quad \forall t \in [t_0, T], \quad (7.3)$$

where $\mathcal{U}(t) \subseteq \mathbb{R}^m$ is the control constraint set. It delimits all the feasible values of the control for the horizon. There can be different control constraint sets for different instants.

The Equations (7.1–7.3) forms unconstrained OCPs. These problems are formalized

$$\begin{aligned} & \max_{\mathbf{q}(t), \mathbf{u}(t)} l_f(\mathbf{q}(T), T) + \int_{t_0}^T l(\mathbf{q}(t), \mathbf{u}(t), t) dt, \\ & \text{s.t. } \dot{\mathbf{q}}(t) = f(\mathbf{q}(t), \mathbf{u}(t), t), \\ & \quad \mathbf{u}(t) \in \mathcal{U}(t), \quad \mathbf{q}(t) \in \mathcal{Q}(t), \\ & \quad \mathbf{q}(t_0) = \mathbf{q}_0 \text{ given.} \end{aligned} \tag{7.4}$$

The evolution of the model is used to derive an optimal control trajectory $\mathbf{u}(t)$ from an initial guess of the state \mathbf{q}_0 and the horizon. This initial simplistic controller does not represent a realistic scenario. The controller implies that the horizon is known. However, it is often the case that only the initial time step of the horizon $[t_0, T]$ is known. In the model from Chapter 4 it is indeed unknown apriori when the aerial robot plan terminates. Moreover the controller does not include any constraint on the state \mathbf{q} , although mobile robots are often bounded by strict battery requirements. Lastly, the optimal control generated with such controller is static given the initial state and the horizon. It is unrealistic to assume that the state of the aerial robot travelling the optimal control \mathbf{u} does not change for instants $t_0 + \Delta t, t_0 + 2\Delta t, \dots, T$.

All these initial assumption (known final time step, absence of state constraints, static optimal control law) will be eased in the remaining of the chapter.

7.2.2 Continuous systems: constrained case

7.2.3 Perturbed systems

7.2.4 Multistage systems

7.3 Numerical Simulation and Differentiation

7.3.1 Euler method

7.3.2 Runge-Kutta methods

7.3.3 Algorithmic differentiation

7.4 Direct Optimal Control Methods

7.4.1 Direct single shooting

7.4.2 Direct multiple shooting

7.4.3 Direct collocation

7.5 Numerical Optimization

7.5.1 Convexity

7.5.2 Optimality conditions

7.5.3 First order optimality conditions

7.5.4 Second order optimality conditions

7.5.5 Sequential quadratic programming

7.5.6 Nonlinear interior point methods

7.6 Model Predictive Control

7.6.1 Output model predictive control

In this section, we address the problem of deriving the optimal control over a finite time horizon N for an estimated state $\hat{\mathbf{q}}$. The control is the configuration of the path and computations parameters, and it differs from the nominal control. In [Section 4.4.2](#) we presented a motivation for such control against the nominal control, based on empirical observations.

To derive the optimal control, we use the estimated state $\hat{\mathbf{q}}$ in [Chapter 5](#), opposed to the perfect state in [Chapter 4](#). The estimated state differs from the perfect state \mathbf{q} due to the uncertainty. In fact, the name of output model predictive control in the literature refers to the notion that some available outputs are used to estimate the not fully known state ([Rawlings et al., 2017](#)). For a differential model, such as the periodic model in [Equation \(4.12\)](#) in [Section 4.4](#), state estimation is done utilizing techniques such as Kalman filtering that we introduced in [Chapter 5](#).

Before defining and solving the OCP in the case of uncertainty over the finite horizon, let us re-evaluate the output constraints. The output of the model in [Equation \(4.12\)](#) is the instantaneous energy consumption y . We stated earlier that it evolves in \mathbb{R} . This is an inexact simplification as aerial robots are bounded by strict energy budgets due to battery limitations, as we motivated in [Section 1.3](#). Let us hence redefine the original output constraint (\mathbb{R}) to include the battery model in [Section 4.2](#). We consider SoC b of the mobile robot's battery with the simplistic differential model in [Equations \(4.1–4.2\)](#)

$$\dot{b}(y(t), t) = -k_b \left(V - \sqrt{V^2 - 4R_r y(t)} \right) / (2R_r Q_c), \quad (7.5)$$

where k_b is the battery coefficient determined experimentally, $V \in \mathbb{R}$ is the internal battery voltage measured in volts, $R_r \in \mathbb{R}$ the resistance measured in ohms, and $Q_c \in \mathbb{R}$ the constant nominal capacity measured in amperes per hour.

We note that the maximum instantaneous energy consumption can be computed by multiplying the constant nominal capacity, the SoC, and the internal battery voltage. We assume the maximum energy consumption cannot be negative

$$0 \leq y(t) \leq b(y(t), t)Q_c V, \quad (7.6)$$

and therefore, we define a time-varying constraint for the output in [Definition 7.6.1](#), being the maximum instantaneous energy consumption dependent on the SoC b from [Equation \(7.5\)](#), which is dependent on time and the instantaneous energy consumption (at the previous time step).

Definition 7.6.1: Output constraint

The *output constraint* is the set

$$\mathcal{Y}(t) := \{y \mid y \in [0, b(y(t), t)Q_c V] \subseteq \mathbb{R}_{\geq 0}\},$$

where $b(y(t), t)Q_c V$ is the maximum instantaneous energy consumption.

We assume the mobile robot carries a battery energy sensor and obtain the initial state of charge $b(y(t_0), t_0)$ utilizing the output of such sensor. This is often the case of aerial robots with a flight controller, which returns various metrics including the battery state of charge.

The evaluation of the output constraint requires numerical simulation being the battery model in [Equation \(7.5\)](#) differential, similarly to the energy dynamics of the periodic model in [Equation \(4.12\)](#). The numerical simulation can be computed using the Euler method in [Section 7.3.1](#). or the Runge-Kutta method in [Section 7.3.2](#).

The OCP can be stated similarly as in [Section 7.2.2](#), with the constraints: the control constraint in [Equation \(2.5\)](#), the output constraint in [Definition 7.6.1](#), and the dynamics with the ideal state evolution in [Equation \(4.12\)](#)

$$\max_{\mathbf{q}(t), c_i(t)} l_f(\mathbf{q}(T), T) + \int_{t_0}^T l(\mathbf{q}(t), c_i(t), t) dt, \quad (7.7a)$$

$$\text{s.t. } \dot{\mathbf{q}} = f(\mathbf{q}(t), c_i(t), t), \quad (7.7b)$$

$$c_i(t) \in \mathcal{U}_i, \mathbf{q}(t) \in \mathbb{R}^m, \quad (7.7c)$$

$$y(t) \in \mathcal{Y}(t), \quad (7.7d)$$

$$\mathbf{q}(t_0) = \hat{\mathbf{q}}_0 \text{ given (last estimate state), and} \quad (7.7e)$$

$$b(y(t_0), t_0) = b_0 \text{ given,} \quad (7.7f)$$

where constraints in [Equations \(7.7b–7.7d\)](#) are evaluated on $t \in [t_0, T]$. $\mathbf{q}(t)$ and $c_i(t)$ are the state and control trajectories.

The sizes of the state and control (m and n) are defined in [Section 4.4](#) and [Section 4.4.2](#).

The dynamic evolution in [Equation \(7.7b\)](#) is then the periodic model in [Equation \(4.12\)](#) together with the scale transformation from [Section 4.4.3](#)

$$f(\mathbf{q}(t), c_i(t), t) = A\mathbf{q}(t) + B\text{diag}(v_i)(c_i(t) - c_i(t - \Delta t)), \quad (7.8)$$

where $c_i(t - \Delta t)$ is the control at the time instant preceding t .

The instantaneous cost function is defined with the quadratic expression

$$l(\mathbf{q}(t), c_i(t), t) = \mathbf{q}'(t)Q\mathbf{q}(t) + c'_i(t)Rc_i(t), \quad (7.9)$$

where $Q \in \mathbb{R}^{m \times m}$, $R \in \mathbb{R}^{n \times n}$ are positive semidefinite matrices.

The final cost function is alike defined with a quadratic expression but with no control

$$l_f(\mathbf{q}(T), T) = \mathbf{q}'(T)Q_f\mathbf{q}(T), \quad (7.10)$$

where $Q_f \in \mathbb{R}^{m \times m}$ is a positive semidefinite matrix.

The optimization horizon is limited to N measured in seconds, meaning the controller will select the optimal control trajectory $c_i^*(t)$ over $[t_0, T]$, with $T = t_0 + N$. At each time instant, the controller refines the control trajectory which respects the constraints: the dynamics in [Equation \(7.7b\)](#) and [Equation \(7.8\)](#), and the control constraint in [Equation \(7.7c\)](#). To evaluate the state trajectory-needed for the instantaneous cost function l and the final cost function l_f —the controller evaluates the battery trajectory $b(y(t), t)$. It then maximizes the instantaneous cost function l for all the time instants but T ($t_0 \leq t < t_0 + N$), and the final cost function l_f in [Equation \(7.10\)](#) for the time instant T ($t = t_0 + N$).

The dynamics constraint satisfaction requires to evolve the perfect model f in [Equation \(7.8\)](#) over horizon $[t_0, t_0 + N]$ beginning from the last estimated state $\mathbf{q}_0 = \dot{\mathbf{q}}(t_0)$ at time instant t_0 . The battery constraint is likewise evolved beginning from the last battery measurement b_0 obtained from the battery energy sensor also at time instant t_0 .

The OCP from [Equation \(7.7\)](#) is infinite dimensional, being the system dynamics in [Equation \(7.7b\)](#) and the battery dynamics in [Equation \(7.5\)](#) given in continuous opposed to discrete time. Such an infinite dimensional OCP has an infinite dimension of constraints and decision variables since there are infinite time instants between t_0 and $t_0 + N$. We discretize the infinite dimensional OCP and discuss the solution to the planning problem in [Chapter 2](#) in [Section 7.6.2](#).

7.6.2 Optimal control generation with model predictive control

In this section we combine the notions from the previous sections in this chapter and [Chapters 4–6](#) and provide a solution to the planning problem in [Chapter 2](#).

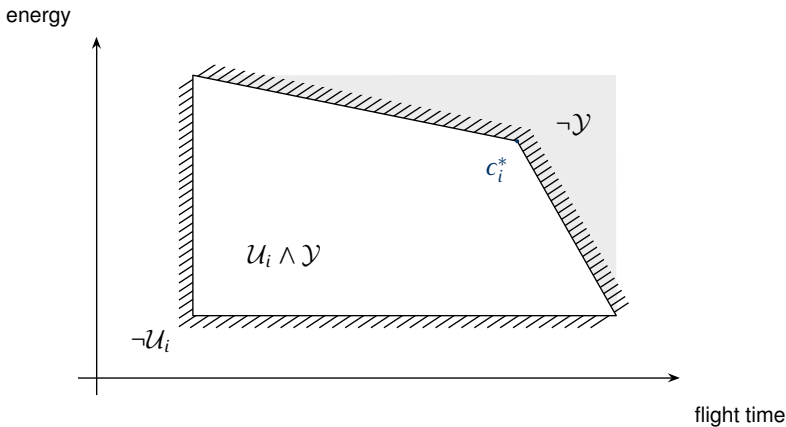


Fig. 7.2. .

First, we need to transform the OCP in [Equation \(7.7\)](#) into an NLP. The optimization problem to be solved numerically in the discrete form is effectively an NLP, due to the nonlinearity in the cost functions l , l_f , and in the constraints

$$\max_{\mathbf{q}(k), c_i(k)} l_f(\mathbf{q}(T), T) + \sum_{k \in \mathcal{K}} l_d(\mathbf{q}(k), c_i(k), k), \quad (7.11a)$$

$$\text{s.t. } \mathbf{q}(k + h) = f_d(\mathbf{q}(k), c_i(k), k), \quad (7.11b)$$

$$c_i(k) \in \mathcal{U}_i, \mathbf{q}(k) \in \mathbb{R}^m, \quad (7.11c)$$

$$y(k) \in \mathcal{Y}(k), \quad (7.11d)$$

$$\mathbf{q}(t_0) = \hat{\mathbf{q}}_0 \text{ given (last estimated state), and} \quad (7.11e)$$

$$b(y(t_0), t_0) = b_0 \text{ given,} \quad (7.11f)$$

where the constraints in [Equations \(7.11b–7.11d\)](#) are now evaluated on a finite interval $k \in \mathcal{K} = \{t_0, t_0 + h, t_0 + 2h, \dots, T\}$, and h is a given distance between two time instants; the smaller the distance the more precise the simulation. The other expressions are analogous to [Equation \(7.7\)](#).

We use numerical simulation to transform [Equation \(7.7\)](#) into [Equation \(7.11\)](#). We can use either the Runge-Kutta methods in [Section 7.3.2](#), or the Euler method in [Section 7.3.1](#). For simplicity, we show the transformation with the Euler method. The instantaneous cost function l_d

$$l_d(\mathbf{q}(k), c_i(k), k) = h l(\mathbf{q}(k), c_i(k), k), \quad (7.12)$$

where l is given in [Equation \(7.9\)](#).

The discrete dynamic evolution in [Equation \(7.11b\)](#)

$$f_d(\mathbf{q}(k), c_i(k), k) = A_d \mathbf{q}(k) + B \text{diag}(\mathbf{v}_i)(c_i(k) - c_i(k-h)), \quad (7.13)$$

where A_d is the discretized version of the state transition matrix A and for small enough interval of h

$$A_d = (hA + \text{diag}(1, 1, \dots, 1)), \quad (7.14)$$

where $\text{diag}(1, 1, \dots, 1) \in \mathbb{R}^{m \times m}$ is a diagonal matrix of ones. We discretize the battery dynamics in [Equation \(7.5\)](#)

$$b_d(y(k + h), k + h) = b(y(k), k) + hb(y(k + h), k + h). \quad (7.15)$$

We transformed the OCP in [Equation \(7.7\)](#) into an NLP in [Equation \(7.11\)](#) by first discretizing and thus effectively implementing the direct multiple shooting method in [Section 7.4.2](#). We note that we can implement the single shooting method by keeping only the initial state as the decision variable $\hat{\mathbf{q}}_0$ opposed to using the interval boundary time points as a decision variable in the multiple shooting method ([Rawlings et al., 2017](#)).

—

7.6.3 Dynamic planning algorithm

7.7 Results

7.8 Summary

Chapter 8

Summary and Future Directions

8.1 Summary

8.2 Contribution

8.3 Future Directions

8.4 Conclusion

Appendix A

Implementation

A.1 Energy Models

To build the model in MATLAB(R) one can use the function `build_model` from Listing A.1.

```
1 function [model] = build_model(dat)
2
3     m = 2*dat.r+1;
4
5     Aj = @(dat.omega,j) [0 dat.omega*j;-dat.omega*j 0];
6     A = zeros(m);
7     A(1,1) = 0;
8
9     B = [zeros(1,dat.rho) ones(1,dat.sigma)];
10
11    C = [1];
12
13    for i = 1:dat.r
14        A(2*i:2*i+1,2*i:2*i+1) = Aj(dat.omega,i);
15        C = [C 1 0];
16        B = [B;zeros(1,dat.rho+dat.sigma)];
17    end
18
19    model.A = A;
20    model.B = B;
21    model.C = C;
22
23    model.est_u = @(c) dat.nu*c+dat.tau;
24    model.u = @(u1,u0) u1-u0;
```

```
26 end
```

Listing A.1. Function `build_model` that creates the energy model.

The function builds the matrices from [Equation \(4.12\)](#). In particular matrix A from [Equation \(4.14\)](#), B from [Equation \(4.48\)](#), and C from [Equation \(4.16\)](#). The term $1/T$ is missing in C as we motivated in the proof of [Lemma 4.4.1](#) in [Equation \(4.42\)](#). The nominal control from [Equation \(4.46\)](#) is u , and the energy estimate of a given control sequence at time instant t and the previous time instant $t - \Delta t$ from [Equation \(4.47\)](#) is `est_u`.

The function requires the structure `dat` illustrated in [Listing A.2](#). The structure contains some information about the model. In particular, `r` is the order r of the model from [Subsection 4.4](#), `omega` is the angular frequency ω , `rho` the number of path parameters to alter the path ρ , and `sigma` the number of computation parameters to alter the computations σ . The path parameters are defined in [Equation \(??\)](#), and the computation parameters are defined in [Equation \(??\)](#). Furthermore, `delta_T` is the sampling step Δt , and `nu` and `tau` are scaling factors (v and τ) from [Equation \(4.49\)](#).

```
1 dat.r = 3;
2 dat.omega = 2*pi/period;
3 dat.rho = 1;
4 dat.sigma = 1;
5 dat.delta_T = .01;
6 dat.nu = nu;
7 dat.tau = tau;
```

Listing A.2. Struct `dat` used by function `build_model` to build the model.

The function `build_model` and the structure `dat` can be used along an initial guess of parameters and a time horizon to model the future energy consumption using the Euler or Runge-Kutta methods for numerical integration. The Euler method is described in [Subsection 7.3.1](#) and implemented in [Listing A.3](#), the Runge-Kutta method in [Subsection 7.3.2](#) and [Listing A.5](#). For the Runge-Kutta method, we use the fourth-order fixed size standard method.

```
1 function [q,y] = evolve_model_euler(model,dat,init)
2
3 m = 2*dat.r+1;
4 Ad = model.A*dat.delta_T+eye();
5
6 q0 = init.q0;
7
8 q = q0;
9 y = C*q0;
10
11 est_u0 = init.est_u0;
12 est_u1 = model.est_u(init.c_chain(1));
```

```

14     i = 2;

16     for init.t0+dat.delta_T:dat.delta_T:init.tf
17         q0 = Ad*q0+model.B*model.u(est_u1,est_u0);
18         est_u0 = est_u1;

20         if i <= size(init.c_chain,2)
21             est_u1 = model.est_u(init.c_chain(i));
22             i = i+1;
23         end

25         q = [q;q0.'];
26         y = [y;c*q0];
27     end
28 end

```

Listing A.3. Euler method for numerical integration of the model.

The function `evolve_model_euler` in Listing A.3 evolve the model in Equation (4.12) from an initial time t_0 to the final time t_f . This information is passed to function using the structure `init` from Listing A.4.

```

1 init.t0 = 0;
2 init.tf = 60;
3 init.q0 = q0;
4 init.est_u0 = est_u0;
5 init.c_chain = c_chain;

```

Listing A.4. Structure `init` with numerical integrator's initializations.

In Listing A.4, the field `t0` indicates the initial time t_0 (the mathematical simulation starts at $t_0 + \Delta t$ assuming the instant t_0 corresponds to the state $\mathbf{q}(t_0) = \mathbf{q}_0$). The field `tf` indicates the final time t_f when the simulation stops. This is usually $t_0 + N$ where N is the optimization horizon. Both fields are expressed in seconds. The field `q0` indicates the initial state guess at time instant t_0 , \mathbf{q}_0 , and finally `c_chain` the sequence of controls. If we assume that the horizon is $N := t_f - t_0$ with $(t_f - t_0) \in \mathbb{R}_{>0}$, then the user is expected to provide $N - 1$ controls. Finally, the field `est_u0` contains the control energy estimate at time t_0 , the value $\hat{\mathbf{u}}(t_{-1})$. If t_0 is the initial time step, then `est_u0` is set to zero.

```
1 % TODO
```

Listing A.5. Runge-Kutta fourth order method for numerical integration of the model.

Before calling structure `dat`, it is necessary to define the scaling factors v_1, v_2, \dots, v_ρ and $\tau_1, \tau_2, \dots, \tau_\rho$ for the path parameters, and $v_{\rho+1}, v_{\rho+2}, \dots, v_{\rho+\sigma}$ and $\tau_{\rho+1}, \tau_{\rho+2}, \dots, \tau_{\rho+\sigma}$ for the computation parameters. For example, we suppose there is one path and one computation parameters.

```
1 nu1 = -(max_t-min_t)/min_c1;
```

```

2 tau1 = -min_c1*(min_t-max_t)/min_c1+min_t;
4 nu2 = (g_max_c2-g_min_c2)/(max_c2-min_c2);
5 tau2 = min_c2*(g_min_c2-g_max_c2)/(max_c2-min_c2)+g_min_c2;
7 nu = [nu1;nu2];
8 tau = [tau1;tau2];

```

Listing A.6. Implementation of path and computation parameters scaling factors.

Listing A.6 has to run before **Listing A.2**.

The scaling factors can be defined according to [Equation \(4.50\)](#) for the path parameter on [Line 1](#) and according to [Equation \(4.51\)](#) for the computation parameter on [Line 4](#).

Let us assume that the one path parameter c_1 doesn't change for the stages $i = \{1, 2, \dots, l\}$. \max_t and \min_t are the maximum and minimum times that correspond to the time needed to hypothetically execute the path with parameter $c_1 = \bar{c}_1$ and with parameter value $c_1 = \underline{c}_1$. A guess for these values can be obtained empirically; we obtained them by running the simulation. They correspond to \bar{t} and \underline{t} in [Equation \(4.50\)](#).

Let us further assume that the one computation parameter c_2 doesn't change for the stages $i = \{1, 2, \dots, l\}$. \max_c2 and \min_c2 are the minimum and maximum configuration of the computation parameter c_2 defined in [Definition 2.3.1](#). g_{\max_c2} and g_{\min_c2} are values retrieved from `powprofiler` and they correspond to $g(\bar{c}_2)$ and $g(\underline{c}_2)$ in [Equation \(4.51\)](#). Function g is formally defined in [Definition 4.1.1](#).

A possible call to the functions `build_model` and `evolve_model_euler` or `evolve_model_rk4` from [Listing A.1](#) and [Listing A.3](#) or [Listing A.5](#) is illustrated in [Listing A.7](#).

```

1 model = build_model(dat);
2 [q,y] = evolve_model_euler(model,dat,init);

```

Listing A.7. An example to build a differential model and evolve it over a horizon N .

A generic routine to plot the resulting modeled energy and the coefficients \mathbf{q} in [Equation \(4.12\)](#) is illustrated in [Listing A.8](#).

```

1 time = dat.t0:model.delta_T:dat.tf;
3 figure;
4 plot(time,y)
5 title('energy evolution');
6 ylabel('power (W)');
7 xlabel('time (sec)');
9 figure;
10 m = 2*dat.r+1;
11 t = tiledlayout(m,1);

```

```

12 title_str = {'alpha','beta'};
13 nexttile, plot(time,q(1,1:end))
14 title(strcat(title_str(1),0));

16 for i=2:m
17     nexttile, plot(time,q(i,1:end))
18     title(strcat(title_str(mod(i,2)+1),i-1));
19 end

21 title(t,'coefs evolution');
22 xlabel(t,'time (sec)');
23 ylabel(t,'value');

```

Listing A.8. A generic plotting routine for them modeled energy and coefficients evolution.

We describe the estimation of T , the period in structure dat, in [Subsection A.2.1](#). We generate the $N - 1$ controls in [Section A.4](#). For benchmarking, one can define the lowest (or similarly the highest) level of parameters with [Listing A.9](#). It has to run before defining the structure init in [Listing A.4](#).

```

1 c_chain = min_c1*ones(1,N-1);
2 c_chain = [c_chain;min_c2*ones(1,N-1)];

```

Listing A.9. Implementation of the lowest possible control for benchmarking.

A.2 State Estimation

A.2.1 Estimation of the period

```

1 % iterating trajectories in the plan to get the constant n (to
    % measure the period)
2 d = [];
3 p = [0; 0];
4 n = 0;

6 for traj = transpose(path) % per each trajectory

8     traj = split(traj,';');
9     traj = str2sym(traj(3));

11    x = p(1);
12    y = p(1);
13    di = double(subs(traj));
14    x = p(1)-sp(1);
15    y = p(2)-sp(2);

17    if ismember(double(subs(traj)),d)
18        break;
19    else

```

```

20      d = [d di];
21  end

23      n = n+1;
24 end

26 fprintf('n is %d\n', n);

```

Listing A.10. Estimation of the period.

A.2.2 Estimation of the state

```

1 minus_q1 = Ad*q0+B*est_u();
3 minus_P1 = Ad*P0*Ad.'+Q;
5 K1 = (minus_P1*C.')(C*minus_P1*C.')+R)^-1;
6 q1 = minus_q1+K1*(pow(end)-C*minus_q1);
7 P1 = (eye(size(q0,1))+K1*C)*minus_P1;

9 q0 = q1;
10 P0 = P1;

12 y = [y;C*q1];
13 q = [q q0];

```

Listing A.11. Estimation of the state using Kalman filter.

A.3 Guidance

```

1 function [u_theta] = gvf_control_2D(p,dot_p,ke,kd,path,grad,
hess,dir)

3 if (nargin(path) > 1) % function handle has two arguments
    (circle)
4     e = path(p(:,1),p(:,2));
5     n = grad(p(:,1),p(:,2));
6 else % one argument (line)
7     e = path(p(:,1));
8     n = grad();
9 end

11 H = hess();
12 E = [0 -1;1 0];
13 tau = dir*E*n;

15 dot_pd = tau-ke*e*n; % (7)
16 ddot_pd = (E-ke*e*eye(2))*H*dot_p-ke*n'*dot_p*n; % (10)
17 ddot_pdhat = -E*(dot_pd*dot_pd')*E*ddot_pd/norm(dot_pd)^3;
    % (9)

```

```

19     dot_Xid = ddot_pdhat'*E*dot_pd/norm(dot_pd); % (13)

21     u_theta = dot_Xid+kd*dot_p'*E*dot_pd/(norm(dot_p)*norm(
22         dot_pd)); % (16)
22 end

```

Listing A.12. Guidance vector field.

```

1 u_theta = gvf_control_2D(log_p(:,end)',pdot,ke,kd,path,grad,
    hess,dir);

3 th_delta = kp*(hd-h)-kvv*vv;
4 wbx = dot(w,[cos(theta),sin(theta)]);
5 vs = cth*(th_nominal+th_delta)+wbx;
6 L = cl*vs*vs;
7 av = 1/m*(L-W);

9 vv = vv+av*delta_T;
10 h = h+vv*delta_T;

12 % Horizontal unicycle model
13 sh = cth*(th_nominal+th_delta);
14 pdot = sh*[cos(theta);sin(theta)]+w;

16 p = p+pdot*delta_T;
17 theta = theta+u_theta*delta_T;
18 theta = wrapToPi(theta); % normalizing between -pi and pi

```

Listing A.13. Call to the guidance function and dynamics evolution.

A.4 Optimal Control Generation

```

1 function [c_chain q_chain] = mpc(min_c1,max_c1,min_c2,max_c2,
    c1,c2,N,eu,b0,b,qc,int_v,q0,Ad,B,C,u,est_u,k,delta_T,r)
2     import casadi.* % import casadi for optimal control

4     interval = k+delta_T:delta_T:k+N; % no k+1 in the formula
        as we add the
5     % initial condition implicitly
6     hh = length(interval);

8     opti = casadi.Opti(); % define opt problem
9     Q = opti.variable(2*r+1,N);
10    U = opti.variable(2,N-1);
11    L = opti.variable(1,N);
12    log_Q = opti.variable(2*r+1,hh);
13    log_b = opti.variable(1,hh);

15    opti.set_initial(Q(:,1),q0);

```

```

17 opti.subject_to(C*Q(:,1)-b0*qc*int_v <= 0);
18 opti.subject_to(U(1,:) == c1);
19 opti.subject_to(min_c2 <= U(2,: ) <= max_c2);
20 opti.subject_to(min_c1 <= U(1,: ) <= max_c1);

22 eeu = eu; % control estimate (from model)
23 eeu = est_u(c1,c2);

25 jjj = 1;
26 dQ = q0; % initial state
27 log_Q(:,1) = dQ;

29 for jj=1:hh-1
30     dQ = Ad*dQ+B*u(eeu,eeu);
31     eeu = eeu;
32     b0 = b0+delta_T*b(C*dQ); % battery dynamics

34     log_Q(:,jj+1) = dQ;
35     log_b(jj+1) = b0;

37 if mod(jj,1/delta_T) == 0 % every sum in the MPC
38     L(jjj) = C*dQ;

40     if (jjj < N)
41         eeu = est_u(U(1,jjj),U(2,jjj));
42     end

44     opti.subject_to(Q(:,jjj+1)-dQ == 0); % dynamics
        const
45     opti.subject_to(C*Q(:,jjj+1)-b0*qc*int_v <= 0); %
        battery const

47     jjj = jjj+1;
48 end
49 end

51 opti.minimize(-sum(L.^2));
52 opti.solver('ipopt');

54 try
55     sol = opti.solve();
56     c_chain = sol.value(U); % optimal control u on N
57 catch
58     c_chain = [ones(1,N-1)*min_c1;ones(1,N-1)*min_c2]; %
        there is no control which sattisfies consts
59 end

61 q_chain = opti.debug.value(Q);

```

```
62 end
```

Listing A.14. Model predictive control.

References

1. Abramov, A., Pauwels, K., Papon, J., Worgotter, F., and Dellen, B. (2012). "Real-time segmentation of stereo videos on a portable system with a mobile gpu". In: *IEEE Transactions on Circuits and Systems for Video Technology* 22.9, pp. 1292–1305 (cit. on pp. 1, 34).
2. Aljanobi, A., Al-Hamed, S., and Al-Suhaimi, S. (2010). "A setup of mobile robotic unit for fruit harvesting". In: *19th International Workshop on Robotics in Alpe-Adria-Danube Region (RAAD 2010)*. IEEE, pp. 105–108 (cit. on p. 2).
3. De-An, Z., Jidong, L., Wei, J., Ying, Z., and Yu, C. (2011). "Design and control of an apple harvesting robot". In: *Biosystems engineering* 110.2, pp. 112–122 (cit. on p. 2).
4. Anderson, J. D. (2005). *Introduction to flight*. McGraw-Hill Higher Education (cit. on pp. 3–5).
5. Bailey, P. E., Lowenthal, D. K., Ravi, V., Rountree, B., Schulz, M., and De Supinski, B. R. (2014). "Adaptive configuration selection for power-constrained heterogeneous systems". In: *2014 43rd International Conference on Parallel Processing*. IEEE, pp. 371–380 (cit. on p. 32).
6. Barik, R., Farooqui, N., Lewis, B. T., Hu, C., and Shpeisman, T. (2016). "A black-box approach to energy-aware scheduling on integrated CPU-GPU systems". In: *Proceedings of the 2016 International Symposium on Code Generation and Optimization*. ACM, pp. 70–81 (cit. on p. 32).
7. Bellman, R. E. (1957). *Dynamic Programming*. Princeton: Princeton University Press (cit. on p. 77).
8. Böhme, T. J. and Frank, B. (2017). "Indirect Methods for Optimal Control". In: *Hybrid Systems, Optimal Control and Hybrid Vehicles: Theory, Methods and Applications*. Cham: Springer International Publishing, pp. 215–231 (cit. on p. 77).
9. Bryson, A. E. and Ho, Y.-C. (1975). *Applied optimal control: optimization, estimation and control*. Hemisphere Publishing Corporation (cit. on pp. 77, 78).
10. Bürkle, A. (2009). "Collaborating miniature drones for surveillance and reconnaissance". In: *Unmanned/Unattended Sensors and Sensor Networks VI*. Vol. 7480. International Society for Optics and Photonics, 74800H (cit. on p. 4).

11. Burri, M., Gasser, L., Käch, M., Krebs, M., Laube, S., Ledergerber, A., Meier, D., Michaud, R., Mosimann, L., Müri, L., et al. (2013). "Design and control of a spherical omnidirectional blimp". In: *2013 IEEE/RSJ International Conference on Intelligent Robots and Systems*. IEEE, pp. 1873–1879 (cit. on p. 6).
12. Calore, E., Schifano, S. F., and Tripiccione, R. (2015). "Energy-performance tradeoffs for HPC applications on low power processors". In: *European Conference on Parallel Processing*. Springer, pp. 737–748 (cit. on p. 33).
13. Camacho, E. F. and Alba, C. B. (2007). *Model predictive control*. London: Springer-Verlag (cit. on p. 78).
14. Chowdhury, P. and Chakrabarti, C. (2005). "Static task-scheduling algorithms for battery-powered DVS systems". In: *IEEE Transactions on Very Large Scale Integration (VLSI) Systems* 13.2, pp. 226–237 (cit. on p. 32).
15. Colombatti, G., Aboudan, A., La Gloria, N., Debei, S., and Flamini, E. (2011). "Lighter-Than-Air UAV with slam capabilities for mapping applications and atmosphere analysis." In: *Memorie della Società Astronomica Italiana Supplementi* 16, p. 42 (cit. on p. 6).
16. Corke, P. (2017). *Robotics, Vision and Control: Fundamental Algorithms in MATLAB*. 2nd. Springer Publishing Company, Incorporated (cit. on pp. 1, 6).
17. Crow, B. P., Widjaja, I., Kim, J. G., and Sakai, P. T. (1997). "IEEE 802.11 wireless local area networks". In: *IEEE Communications magazine* 35.9, pp. 116–126 (cit. on p. 28).
18. Cui, J. Q., Phang, S. K., Ang, K. Z., Wang, F., Dong, X., Ke, Y., Lai, S., Li, K., Li, X., Lin, F., et al. (2015). "Drones for cooperative search and rescue in post-disaster situation". In: *2015 IEEE 7th international conference on cybernetics and intelligent systems (CIS) and IEEE conference on robotics, automation and mechatronics (RAM)*. IEEE, pp. 167–174 (cit. on p. 4).
19. Daponte, P., De Vito, L., Glielmo, L., Iannelli, L., Liuzza, D., Picariello, F., and Silano, G. (2019). "A review on the use of drones for precision agriculture". In: *IOP Conference Series: Earth and Environmental Science*. Vol. 275. 1. IOP Publishing, p. 012022 (cit. on pp. 2, 4, 10).
20. De Marina, H. G., Kapitanyuk, Y. A., Bronz, M., Hattenberger, G., and Cao, M. (2017). "Guidance algorithm for smooth trajectory tracking of a fixed wing UAV flying in wind flows". In: *2017 IEEE International Conference on Robotics and Automation (ICRA)*. IEEE, pp. 5740–5745 (cit. on pp. 11, 71, 72).
21. Dong, F., Heinemann, W., and Kasper, R. (2011). "Development of a row guidance system for an autonomous robot for white asparagus harvesting". In: *Computers and Electronics in Agriculture* 79.2, pp. 216–225 (cit. on p. 2).
22. Dressler, F. and Fuchs, G. (2005). "Energy-aware operation and task allocation of autonomous robots". In: *Proceedings of the Fifth International Workshop on Robot Motion and Control, 2005. RoMoCo'05*. IEEE, pp. 163–168 (cit. on p. 32).
23. Edan, Y., Rogozin, D., Flash, T., and Miles, G. E. (2000). "Robotic melon harvesting". In: *IEEE Transactions on Robotics and Automation* 16.6, pp. 831–835 (cit. on p. 2).
24. Fabiani, P., Fuertes, V., Piquereau, A., Mampey, R., and Teichteil-Königsbuch, F. (2007). "Autonomous flight and navigation of VTOL UAVs: from autonomy demonstrations to out-of-sight flights". In: *Aerospace Science and Technology* 11.2-3, pp. 183–193 (cit. on p. 36).

25. Fisher, M., Dennis, L., and Webster, M. (2013). "Verifying autonomous systems". In: *Communications of the ACM* 56.9, pp. 84–93 (cit. on p. 1).
26. Floreano, D. and Wood, R. J. (2015). "Science, technology and the future of small autonomous drones". In: *Nature* 521.7553, pp. 460–466 (cit. on p. 5).
27. Fui Liew, C., DeLatte, D., Takeishi, N., and Yairi, T. (2017). "Recent Developments in Aerial Robotics: A Survey and Prototypes Overview". In: *arXiv e-prints*, arXiv–1711 (cit. on p. 6).
28. García-Martín, E., Rodrigues, C. F., Riley, G., and Grahn, H. (2019). "Estimation of energy consumption in machine learning". In: *Journal of Parallel and Distributed Computing* 134, pp. 75–88 (cit. on p. 32).
29. Gonçalves, V. M., Pimenta, L. C., Maia, C. A., Dutra, B. C., and Pereira, G. A. (2010). "Vector fields for robot navigation along time-varying curves in n -dimensions". In: *IEEE Transactions on Robotics* 26.4, pp. 647–659 (cit. on p. 71).
30. González-Jorge, H., Martínez-Sánchez, J., Bueno, M., et al. (2017). "Unmanned aerial systems for civil applications: A review". In: *Drones* 1.1, p. 2 (cit. on p. 4).
31. Goraczko, M., Liu, J., Lymberopoulos, D., Matic, S., Priyantha, B., and Zhao, F. (2008). "Energy-optimal software partitioning in heterogeneous multiprocessor embedded systems". In: *2008 45th ACM/IEEE Design Automation Conference*. IEEE, pp. 191–196 (cit. on p. 32).
32. Hajaj, S. S. H. and Sahari, K. S. M. (2014). "Review of research in the area of agriculture mobile robots". In: *The 8th International Conference on Robotic, Vision, Signal Processing & Power Applications*. Springer, pp. 107–117 (cit. on p. 2).
33. Hasan, A., Skriver, M., and Johansen, T. A. (2018). "Exogenous kalman filter for state-of-charge estimation in lithium-ion batteries". In: *2018 IEEE Conference on Control Technology and Applications (CCTA)*. IEEE, pp. 1403–1408 (cit. on pp. 31, 48).
34. Haugen, J. and Imsland, L. (2016). "Monitoring Moving Objects Using Aerial Mobile Sensors". In: *IEEE Transactions on Control Systems Technology* 24.2, pp. 475–486 (cit. on p. 6).
35. Hobby, H. (2020). *Opterra 2m Wing BNF Basic*. URL: <https://www.horizonhobby.com/opterra-2m-wing-bnf-basic-p-e6f11150> (visited on 02/02/2020) (cit. on p. 2).
36. Hong, I., Kirovski, D., Qu, G., Potkonjak, M., and B, S. M. (1999). "Power optimization of variable-voltage core-based systems". In: *IEEE Transactions on Computer-Aided Design of Integrated Circuits and Systems* 18.12, pp. 1702–1714 (cit. on p. 32).
37. Hong, S. and Kim, H. (2010). "An integrated GPU power and performance model". In: *ACM SIGARCH Computer Architecture News*. Vol. 38. 3. ACM, pp. 280–289 (cit. on p. 32).
38. Jaramillo-Avila, U., Aitken, J. M., and Anderson, S. R. (2019). "Visual saliency with foveated images for fast object detection and recognition in mobile robots using low-power embedded GPUs". In: *2019 19th International Conference on Advanced Robotics (ICAR)*. IEEE, pp. 773–778 (cit. on pp. 1, 34).
39. Kanellakis, C. and Nikolakopoulos, G. (2017). "Survey on computer vision for UAVs: Current developments and trends". In: *Journal of Intelligent & Robotic Systems* 87.1, pp. 141–168 (cit. on p. 33).

40. Kapitanyuk, Y. A., Proskurnikov, A. V., and Cao, M. (2017). "A guiding vector-field algorithm for path-following control of nonholonomic mobile robots". In: *IEEE Transactions on Control Systems Technology* 26.4, pp. 1372–1385 (cit. on p. 71).
41. Karaca, Y., Cicek, M., Tatli, O., Sahin, A., Pasli, S., Beser, M. F., and Turedi, S. (2018). "The potential use of unmanned aircraft systems (drones) in mountain search and rescue operations". In: *The American journal of emergency medicine* 36.4, pp. 583–588 (cit. on p. 4).
42. Keane, J. F. and Carr, S. S. (2013). "A brief history of early unmanned aircraft". In: *Johns Hopkins APL Technical Digest* 32.3, pp. 558–571 (cit. on p. 3).
43. Kellermann, R., Biehle, T., and Fischer, L. (2020). "Drones for parcel and passenger transportation: A literature review". In: *Transportation Research Interdisciplinary Perspectives* 4, p. 100088 (cit. on p. 4).
44. Kim, C. H. and Kim, B. K. (2005). "Energy-saving 3-step velocity control algorithm for battery-powered wheeled mobile robots". In: *Proceedings of the 2005 IEEE international conference on robotics and automation*. IEEE, pp. 2375–2380 (cit. on p. 34).
45. Kim, H. and Kim, B.-K. (2008). "Minimum-energy translational trajectory planning for battery-powered three-wheeled omni-directional mobile robots". In: *2008 10th International Conference on Control, Automation, Robotics and Vision*. IEEE, pp. 1730–1735 (cit. on p. 34).
46. Kirk, D. E. (2004). *Optimal control theory: an introduction*. Courier Corporation (cit. on pp. 75, 76, 78).
47. Kreciglowa, N., Karydis, K., and Kumar, V. (2017). "Energy efficiency of trajectory generation methods for stop-and-go aerial robot navigation". In: *2017 International Conference on Unmanned Aircraft Systems (ICUAS)*. IEEE, pp. 656–662 (cit. on pp. 33, 34).
48. Kuo, B. (1967). *Automatic Control Systems*. Electrical engineering series. Prentice-Hall (cit. on p. 54).
49. Kwon, W. H. and Han, S. H. (2005). *Receding horizon control: model predictive control for state models*. London: Springer-Verlag (cit. on p. 78).
50. LaValle, S. M. (2006). *Planning algorithms*. Cambridge university press (cit. on p. 77).
51. Li, Z., Liu, J., Li, P., and Li, W. (2008). "Analysis of workspace and kinematics for a tomato harvesting robot". In: *2008 International Conference on Intelligent Computation Technology and Automation (ICICTA)*. Vol. 1. IEEE, pp. 823–827 (cit. on p. 2).
52. Lindemann, S. R. and LaValle, S. M. (2005). "Smoothly blending vector fields for global robot navigation". In: *Proceedings of the 44th IEEE Conference on Decision and Control*. IEEE, pp. 3553–3559 (cit. on p. 71).
53. Luo, J. and Jha, N. K. (2001). "Battery-aware static scheduling for distributed real-time embedded systems". In: *Proceedings of the 38th annual Design Automation Conference*. ACM, pp. 444–449 (cit. on p. 32).
54. Marowka, A. (2017). "Energy-aware modeling of scaled heterogeneous systems". In: *International Journal of Parallel Programming* 45.5, pp. 1026–1045 (cit. on p. 31).

55. Mei, Y., Lu, Y.-H., Hu, Y. C., and Lee, C. G. (2004). "Energy-efficient motion planning for mobile robots". In: *IEEE International Conference on Robotics and Automation, 2004. Proceedings. ICRA'04. 2004*. Vol. 5. IEEE, pp. 4344–4349 (cit. on pp. 1, 32, 34, 35).
56. — (2005). "A case study of mobile robot's energy consumption and conservation techniques". In: *ICAR'05. Proceedings., 12th International Conference on Advanced Robotics, 2005*. IEEE, pp. 492–497 (cit. on pp. 1, 32, 34, 35).
57. Mei, Y., Lu, Y.-H., Hu, Y. C., and Lee, C. G. (2006). "Deployment of mobile robots with energy and timing constraints". In: *IEEE Transactions on robotics* 22.3, pp. 507–522 (cit. on pp. 1, 34).
58. Milas, A. S., Cracknell, A. P., and Warner, T. A. (2018). "Drones - the third generation source of remote sensing data". In: *International Journal of Remote Sensing* 39.21, pp. 7125–7137 (cit. on p. 4).
59. Moler, C. and Van Loan, C. (2003). "Nineteen dubious ways to compute the exponential of a matrix, twenty-five years later". In: *SIAM review* 45.1, pp. 3–49 (cit. on p. 55).
60. Morbidi, F., Cano, R., and Lara, D. (2016). "Minimum-energy path generation for a quadrotor UAV". In: *2016 IEEE International Conference on Robotics and Automation (ICRA)*. IEEE, pp. 1492–1498 (cit. on p. 34).
61. Mudge, T. (2001). "Power: A first-class architectural design constraint". In: *Computer* 34.4, pp. 52–58 (cit. on p. 35).
62. Nikov, K., Nunez-Yanez, J. L., and Horsnell, M. (2015). "Evaluation of hybrid run-time power models for the ARM big. LITTLE architecture". In: *2015 IEEE 13th International Conference on Embedded and Ubiquitous Computing*. IEEE, pp. 205–210 (cit. on pp. 33, 64).
63. Nocedal, J. and Wright, S. (2006). *Numerical optimization*. Springer Science & Business Media (cit. on p. 75).
64. Noor, N. M., Abdullah, A., and Hashim, M. (2018). "Remote sensing UAV/drones and its applications for urban areas: a review". In: *IOP conference series: Earth and environmental science*. Vol. 169. 1. IOP Publishing, p. 012003 (cit. on p. 4).
65. Nunez-Yanez, J. and Lore, G. (2013). "Enabling accurate modeling of power and energy consumption in an ARM-based System-on-Chip". In: *Microprocessors and Microsystems* 37.3, pp. 319–332 (cit. on pp. 33, 64).
66. Ogata, K. (2002). *Modern Control Engineering*. Prentice Hall (cit. on p. 54).
67. Panagou, D. (2014). "Motion planning and collision avoidance using navigation vector fields". In: *2014 IEEE International Conference on Robotics and Automation (ICRA)*. IEEE, pp. 2513–2518 (cit. on p. 71).
68. Paparazzi (2016). *UAV open-source project*. URL: <http://wiki.paparazziuav.org/> (visited on 09/01/2016) (cit. on p. 10).
69. Paucar, C., Morales, L., Pinto, K., Sánchez, M., Rodríguez, R., Gutierrez, M., and Palacios, L. (2018). "Use of drones for surveillance and reconnaissance of military areas". In: *International Conference of Research Applied to Defense and Security*. Springer, pp. 119–132 (cit. on p. 4).
70. Paulen, R. and Fikar, M. (2016). "Solution of Optimal Control Problems". In: *Optimal Operation of Batch Membrane Processes*. Cham: Springer International Publishing, pp. 37–56 (cit. on pp. 76, 77).

71. Pensieri, M. G., Garau, M., and Barone, P. M. (2020). "Drones as an Integral Part of Remote Sensing Technologies to Help Missing People". In: *Drones* 4.2, p. 15 (cit. on p. 4).
72. Percin, M., Eisma, J., Van Oudheusden, B., Remes, B., Ruijsink, R., and De Wagter, C. (2012). "Flow Visualization in the Wake of the Flapping-Wing MAV 'DelFly II' in Forward Flight". In: *30th AIAA Applied Aerodynamics Conference*. AIAA (cit. on p. 6).
73. Poe, W. A. and Mokhatab, S. (2017). "Process Control". In: *Modeling, Control, and Optimization of Natural Gas Processing Plants*. Ed. by W. A. Poe and S. Mokhatab. Boston: Gulf Professional Publishing, pp. 97–172 (cit. on p. 77).
74. Pontryagin, L. S., Mishchenko, E., Boltyanskii, V., and Gamkrelidze, R. (1962). *The mathematical theory of optimal processes*. Wiley (cit. on p. 77).
75. *Public Deliverables of the TeamPlay Horizon2020 Project* (2019). <https://teamplay-h2020.eu/index.php?page=deliverables>. Accessed: 2019-08-25 (cit. on p. 33).
76. Puri, V., Nayyar, A., and Raja, L. (2017). "Agriculture drones: A modern breakthrough in precision agriculture". In: *Journal of Statistics and Management Systems* 20.4, pp. 507–518 (cit. on pp. 2, 4).
77. PX4 (2016). *PX4 open-source autopilot*. URL: <https://px4.io/> (visited on 09/01/2016) (cit. on p. 10).
78. Qingchun, F., Wengang, Z., Quan, Q., Kai, J., and Rui, G. (2012). "Study on strawberry robotic harvesting system". In: *2012 IEEE International Conference on Computer Science and Automation Engineering (CSAE)*. Vol. 1. IEEE, pp. 320–324 (cit. on p. 2).
79. Quigley, M., Conley, K., Gerkey, B., Faust, J., Foote, T., Leibs, J., Wheeler, R., and Ng, A. Y. (2009). "ROS: an open-source Robot Operating System". In: *ICRA workshop on open source software*. Vol. 3. 3.2, p. 5 (cit. on p. 28).
80. Rao, R., Vrudhula, S., and Rakhmatov, D. N. (2003). "Battery modeling for energy aware system design". In: *Computer* 36.12, pp. 77–87 (cit. on p. 31).
81. Rao, S. S. (2019). *Engineering optimization: theory and practice*. John Wiley & Sons (cit. on p. 78).
82. Rawlings, J. B., Mayne, D. Q., and Diehl, M. (2017). *Model predictive control: theory, computation, and design*. Vol. 2. Madison, Wisconsin: Nob Hill Publishing (cit. on pp. 11, 75, 77, 78, 80, 84).
83. Redmon, J. (2013–2016). *Darknet: Open Source Neural Networks in C*. <http://pjreddie.com/darknet/> (cit. on p. 39).
84. Redmon, J., Divvala, S., Girshick, R., and Farhadi, A. (2016). "You only look once: Unified, real-time object detection". In: *Proceedings of the IEEE conference on computer vision and pattern recognition*, pp. 779–788 (cit. on p. 39).
85. Redmon, J. and Farhadi, A. (2017). "YOLO9000: Better, Faster, Stronger". In: *IEEE Conference on Computer Vision and Pattern Recognition (CVPR)*. Honolulu, USA, pp. 6517–6525 (cit. on p. 39).
86. Rizvi, S. T. H., Cabodi, G., Patti, D., and Gulzar, M. M. (2017). "A general-purpose graphics processing unit (gpgpu)-accelerated robotic controller using a low power mobile platform". In: *Journal of Low Power Electronics and Applications* 7.2, p. 10 (cit. on pp. 1, 34).

87. Rossiter, J. A. (2004). *Model-based predictive control: a practical approach*. Boca Raton, Florida: CRC press (cit. on p. 78).
88. Sadrpour, A., Jin, J., and Ulsoy, A. G. (2013a). "Mission Energy Prediction for Unmanned Ground Vehicles Using Real-time Measurements and Prior Knowledge". In: *Journal of Field Robotics* 30.3, pp. 399–414 (cit. on pp. 33, 34).
89. Sadrpour, A., Jin, J., and Ulsoy, A. G. (2013b). "Experimental validation of mission energy prediction model for unmanned ground vehicles". In: *2013 American Control Conference*. IEEE, pp. 5960–5965 (cit. on pp. 33, 34).
90. Satria, M. T., Gurumani, S., Zheng, W., Tee, K. P., Koh, A., Yu, P., Rupnow, K., and Chen, D. (2016). "Real-time system-level implementation of a telepresence robot using an embedded GPU platform". In: *2016 Design, Automation & Test in Europe Conference & Exhibition (DATE)*. IEEE, pp. 1445–1448 (cit. on pp. 1, 34).
91. Schuyler, T. J., Gohari, S., Pundsack, G., Berchoff, D., and Guzman, M. I. (2019). "Using a balloon-launched unmanned glider to validate real-time WRF modeling". In: *Sensors* 19.8, p. 1914 (cit. on p. 4).
92. Seewald, A. (2020). "Beyond Traditional Energy Planning: the Weight of Computations in Planetary Exploration". In: *IROS Workshop on Planetary Exploration Robots: Challenges and Opportunities (PLANROBO20)*. ETH Zurich, Department of Mechanical and Process Engineering, p. 3 (cit. on p. 11).
93. Seewald, A., Ebeid, E., and Schultz, U. P. (2019). "Dynamic Energy Modelling for SoC Boards: Initial Experiments". In: *HLPGPU 2019: High-Level Programming for Heterogeneous and Hierarchical Parallel Systems*, p. 4 (cit. on pp. 33, 45).
94. Seewald, A., Garcia de Marina, H., Midtiby, H. S., and Schultz, U. P. (2020). "Mechanical and Computational Energy Estimation of a Fixed-Wing Drone". In: *2020 Fourth IEEE International Conference on Robotic Computing (IRC)*. IEEE, pp. 135–142 (cit. on pp. 1, 11).
95. Seewald, A., Schultz, U. P., Roeder, J., Rouxel, B., and Grelck, C. (2019). "Component-based computation-energy modeling for embedded systems". In: *Proceedings Companion of the 2019 ACM SIGPLAN International Conference on Systems, Programming, Languages, and Applications: Software for Humanity*. ACM, pp. 5–6 (cit. on p. 47).
96. Seguin, C., Blaqui  re, G., Loundou, A., Michelet, P., and Markarian, T. (2018). "Unmanned aerial vehicles (drones) to prevent drowning". In: *Resuscitation* 127, pp. 63–67 (cit. on p. 4).
97. Sethi, S. P. (2019). *Optimal Control Theory: Applications to Management Science and Economics*. Cham: Springer International Publishing (cit. on pp. 75–78).
98. Siciliano, B. and Khatib, O. (2016). *Springer handbook of robotics*. Springer. Chap. 44, pp. 1012–1014 (cit. on pp. 3–7, 36).
99. Simon, D. (2006). *Optimal state estimation: Kalman, H infinity, and nonlinear approaches*. John Wiley & Sons (cit. on pp. 67, 78).
100. Stengel, R. F. (1994). *Optimal control and estimation*. Courier Corporation (cit. on pp. 67, 78).
101. Sudhakar, S., Karaman, S., and Sze, V. (2020). "Balancing Actuation and Computing Energy in Motion Planning". In: *2020 IEEE International Conference on Robotics and Automation (ICRA)*. IEEE, pp. 4259–4265 (cit. on p. 1).

102. Tang, L. and Shao, G. (2015). "Drone remote sensing for forestry research and practices". In: *Journal of Forestry Research* 26.4, pp. 791–797 (cit. on p. 4).
103. Uragun, B. (2011). "Energy efficiency for unmanned aerial vehicles". In: *2011 10th International Conference on Machine Learning and Applications and Workshops*. Vol. 2. IEEE, pp. 316–320 (cit. on p. 33).
104. Valavanis, K. P. and Vachtsevanos, G. J. (2015). *Handbook of unmanned aerial vehicles*. Vol. 1. Springer (cit. on p. 3).
105. Von Stryk, O. and Bulirsch, R. (1992). "Direct and indirect methods for trajectory optimization". In: *Annals of operations research* 37.1, pp. 357–373 (cit. on p. 75).
106. Voosen, P. (2019). *NASA to fly drone on Titan* (cit. on p. 5).
107. Wahab, M., Rios-Gutierrez, F., and El Shahat, A. (2015). *Energy modeling of differential drive robots*. IEEE (cit. on p. 34).
108. Wang, L. (2009). *Model predictive control system design and implementation using Matlab*. London: Springer Science & Business Media (cit. on p. 78).
109. Woo, D. H. and Lee, H.-H. S. (2008). "Extending Amdahl's law for energy-efficient computing in the many-core era". In: *Computer* 41.12, pp. 24–31 (cit. on p. 35).
110. Wu, G., Greathouse, J. L., Lyashevsky, A., Jayasena, N., and Chiou, D. (2015). "GPGPU performance and power estimation using machine learning". In: *2015 IEEE 21st International Symposium on High Performance Computer Architecture (HPCA)*. IEEE, pp. 564–576 (cit. on p. 32).
111. Zamanakos, G., Seewald, A., Midtiby, H. S., and Schultz, U. P. (2020). "Energy-Aware Design of Vision-Based Autonomous Tracking and Landing of a UAV". In: *2020 Fourth IEEE International Conference on Robotic Computing (IRC)*. IEEE, pp. 294–297 (cit. on p. 2).
112. Zhou, D. and Schwager, M. (2014). "Vector field following for quadrotors using differential flatness". In: *2014 IEEE International Conference on Robotics and Automation (ICRA)*. IEEE, pp. 6567–6572 (cit. on p. 71).

Index

- barometer, 3
- blimps, 6
- coax, 6
- computations, 16
- computations energy, 16
- computations parameters, 18
- control surface, 7
- convolutional neural network, 10
- CPU, 10
- data-driven control, 3
- difference of motion and computations energy, 16
- finite state machine, 20
- fixed-wings, 6
- flapping-wings, 5
- frames per second, 16
- global navigation satellite system, 3
- global positioning system, 4
- GPU, 1, 10
- gyroscope, 3
- heavier-than-air aerial robots, 5
- helicopters, 6
- heterogeneous computing hardware, 7
- Hewitt-Sperry automatic airplane, 3
- hexacopters, 6
- hovering, 6
- inertial measurement unit, 3
- lighter-than-air aerial robots, 6
- Lockheed D-21, 4
- meteorology, 4
- micro aerial vehicles, 7
- microcontroller, 7
- motion, 16
- motion energy, 16
- motor, 7
- multirotors, 6
- octocopters, 6
- Opterra fixed-wing aerial robot, 2
- output constraint, 81
- overall energy, 16
- path functions, 17
- path parameters, 18
- payload delivery, 4
- period, 21
- planning problem, 23
- precision agriculture, 2
- primitive paths, 21
- quadcopters, 6
- quadrotors, 6

- reconnaissance, surveillance, and target acquisition, 4
- remote sensing, 4
- remotely piloted vehicles, 3
- rotary-wings, 6
- Ryan Firebee, 4
- search and rescue, 4
- servo, 7
- stage, 19
- surveillance, 4
- tradeoffs, 10
- unmanned aerial systems, 3
- unmanned aerial vehicles, 3
- V-1 flying bomb, 4
- vertical take-off and landing, 7
- World War I, 3
- Wright brother, 3